Technical University of Denmark

Supramolecular Derivation of Graphene Nanomaterials for Chemical Sensors

Olsen, Gunnar; Chi, Qijin; Ulstrup, Jens

Publication date:
2016

Document Version
Publisher's PDF, also known as Version of record

Link back to DTU Orbit

Citation (APA):
Olsen, G., Chi, Q., & Ulstrup, J. (2016). Supramolecular Derivation of Graphene Nanomaterials for Chemical Sensors. DTU Chemistry.

DTU Library
Technical Information Center of Denmark

Supramolecular Derivation of Graphene Nanomaterials for Chemical Sensors

A dissertation by Gunnar Olsen

Submitted to

The Department of Chemistry

In partial fulfilment of the requirements

For the degree of

Doctor of Philosophy (Ph.D.)

In the subject of Chemistry
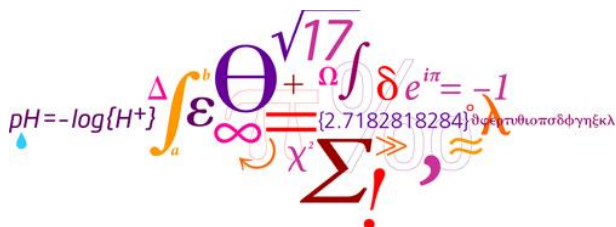
Kongens Lyngby April 2016

"The chemists are a strange class of mortals, impelled by an almost insane impulse to seek their pleasures amid smoke and vapour, soot and flame, poisons and poverty; yet among all these evils I seem to live so sweetly that may I die if I were to change places with the Persian king"

– Johann Joachim Becher 1667

Preface and Acknowledgements

April 2016, Kgs. Lyngby

Gunnar Olsen

Abstract

With properties such as high surface area, high conductivity, and low production cost with easy up-scaling, graphene-like materials provide a promising support for many applications, one of which is for chemical sensors. By functionalization with molecular receptors such as supramolecular moieties, which have long been used for chemical sensing, graphene-like, materials can be endowed with increasing selectivity to form better and cheaper sensing composite materials.

In this Ph.D. project, reduced graphene oxide (RGO) has been covalently functionalized with supramolecular moieties to create active sensing materials. Two different strategies have been applied to achieve specific functionalization: The first approach consisted of covalently attaching chemically resistant supramolecular moieties, in the present work crown-ethers to graphene oxide (GO); the functionalized GO was then reduced chemically. This resulted in monolayer RGO nanosheets functionalized with crown-ether to an extent of up to 30% of the theoretically available surface area (Figure 1). These materials were shown to selectively bind alkali metal ions, and potentiometric sensing based on the materials was achieved with a detection limit of 10^{-5} M.
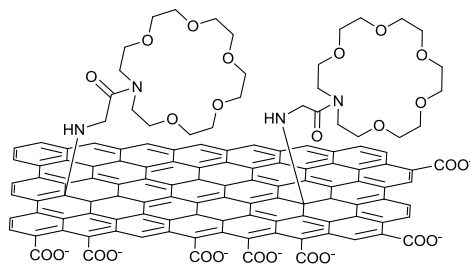
Figure 1: Schematic representation of the synthesized RGO nanosheet functionalized with crown-ether.

In the second approach Azido-RGO was prepared as a general platform for post reduction modification. GO was here functionalized with a short linker terminated in an alcohol. The intermediate material was then reduced effectively with NaBH$_4$, followed by chemical transformation of the alcohol into azide, thus providing a chemical handle for click chemistry in the form of CuAAC (Figure 2).

This platform material has then functionalized with ferrocene as a redox probe to accurately determine surface coverage which showed that the material one azido-functionality was attached per 16 RGO-sheet carbon atoms or slightly more than one azide per nm^2 of RGO-sheet.
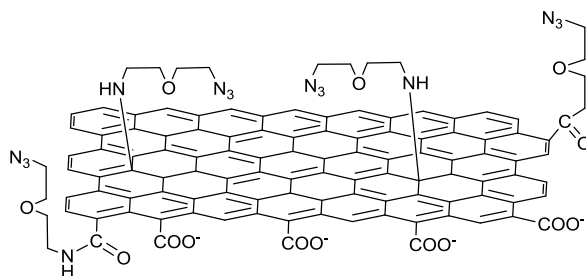
Figure 2: Schematic representation of the synthesized Azido-RGO, a RGO nanosheet functionalized with azides, which can be further functionalized with desirable groups or molecules after the reduction step by CuAAC.

This Azido-RGO was used in successful functionalization with the large supramolecular receptor molecules TTF-calix[4]pyrrole which function as a sensor for Cl$^-$ and potentially for TNB. The coverage achieved was one molecule per 50 – 60 carbon atoms in the RGO-sheet. In view of the size of this molecular moiety, the coverage is actually very high. The material was used for Cl$^-$ sensing showing sensitivity at very low concentration with linear response in the concentration range $10^{-8} - 10^{-5}$ M.

Résumé

Grafen-ligende materials egenskaber som stort overfladeareal, høj ledningsevne, lave produktionsomkostninger samt gode muligheder for opskalering, gør grafen-baserede materialer til lovende supportmateriale for en række anvendelser. En af disse for anvendelse i kemiske sensorer. Ved funktionalisering af grafen med molekylære receptorer som supramolekylære enheder, som længe har været anvendt som kemiske sensorer, kan disse egenskaber overføres til grafenmaterialet og resulterer i øget selektivitet medførende bedre og billigere sensormaterialer.

I dette Ph.d. projekt er RGO blevet kovalent funktionaliseret med supramolekylære enheder for at skabe aktive sensormaterialer. For at opnå denne funktionalisering er to forskellige strategier blevet anvendt: Den første strategi bestod i først at anvende kovalent kemi til fastgørelse af supramolekylære enheder som kroneether til GO, hvorefter det funktionaliserede GO reduceres kemisk. Dette resulterede i et atomart monolag af RGO funktionaliseret med kroneether op mod 30% af det teoretisk tilgængelige overfladeareal (Figur 3). Det blev vist, at disse materialer har egenskaber til selektivt at binde alkalimetalioner. Dermed kunne dette materiale anvendes at fremstille en potentiometrisk sensor med en detektionsgrænse på 10^{-5} M.
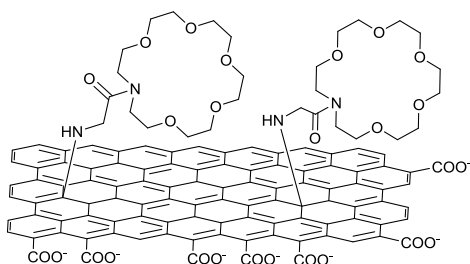
Figur 3: Skematisk illustration af det syntetiserede RGO funktionaliseret med kroneether.

Den anden strategi til funktionalisering af RGO med supramolekylærer enheder var at fremstille et nyt materiale, azido-RGO som platform. Hvorpå disse enheder kunne påsættes efter reduktion af GO til RGO. Dette er en stor fordel for enheder, som ikke er kemisk resistente over for reduktion. GO blev funktionaliseret med en kortmolekylær kæde med en alkoholgruppe yderst. Det funktionaliserede materiale blev derefter reduceret effektivt med NaBH$_4$ efterfulgt af kemisk substitution af alkoholen med azid. Denne azid kan anvendes som et kemisk "håndtag" ved brug af click-kemi i form af CuAAC. Dette platformmateriale blev studeret ved at funktionalisere det med, en redox probe ferrocen, som kan bruges til nøjagtigt at bestemme overfladedækning via elektrokemi. Dette viste, at materialet havde én

azidgruppe pr 16 kulstofatomer i RGO materialet hvilket svarer til lidt mere end én azidgruppe per nm^2 af RGO (Figur 4).
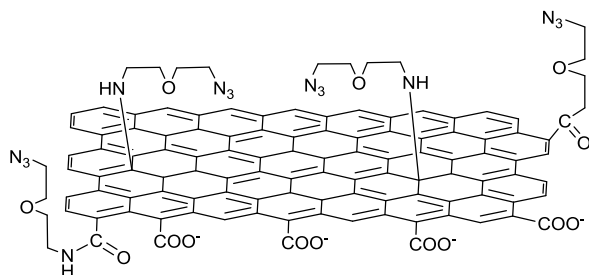
Figur 4: Skematisk illustration af det syntetiserede azido-RGO, et RGO "nanolag" funktionaliseret med azider, som kan funktionaliseres efter reduktionstrinet ved CuAAC.

Dette azido-RGO blev også brugt til at funktionalisere RGO med et stort supramolekylært receptormolekyle TTF-calix[4]pyrrol, der kan fungere som er en Cl$^-$ sensor. Det lykkes at funktionalisere RGO med én TTF-calix[4]pyrrol per 50 – 60 kulstofatomer i RGO materialet. Dette er meget høj dækning når størrelse af denne TTF-calix[4]pyrrol tages i betragtning. Det producerede materiale blev brugt til Cl$^-$ detektion og viste følsomhed ved meget lav koncentration af Cl$^-$ med lineært respons i koncentrationsområdet 10^{-8} – 10^{-5} M.

Thesis Structure

The thesis is structured in seven chapters. Chapter 1 provides a brief introduction to the core concepts that form the foundation of this work. Chapter 2 provides a more specific introduction to the key materials used in this thesis namely graphene related materials as well as a brief overview on how these materials in conjunction with supramolecular moieties have been used to construct chemical sensors. The following three chapters describe the work carried out in the Ph.D. project. They are structured in such a way that a short introduction to relevant previous work or important theory not covered in chapter 1 or 2 is first given, followed by synthesis, characterization and functional tests of the materials of presented.

Chapter 3 describes the work on covalent functionalization of reduced graphene oxide (RGO) with crown-ether moieties to produce sensing materials for alkali metals. Chapter 4 describes Azido-RGO as a platform material, onto which any chemical sensing components can in principle straight forwardly be attached. Chapter 5 describes, how a complex chemical sensor moiety TTF-calix[4]pyrrole can be attached to Azido RGO, in order to achieve a surface confined electrochemically active sensing system. Chapter 6 summarizes and concludes on the produced work. Chapter 7 provide the detailed experimental procedures used in the thesis work.

Table of Content

List of Abbreviations

ATR-FTIR – Attenuated total reflection Fourier transform infrared spectroscopy

BET – Brunauer–Emmett–Teller

CD – Carbon dots

CIAC – Changchun Institute of Applied Chemistry

CMG – Chemically modified graphene

CT – Charge Transfer

CuAAC – Copper(I)-catalyzed Azide-Alkyne Cycloaddition

CV – Cyclic voltammetry or cyclic voltammogram

CVD – Chemical vapour deposition

DCC – *N,N'*-Dicyclohexylcarbodiimide

DFT – Density functional theory

DGU – Density gradient ultra centrifugation

DMAP – 4-Dimethylaminopyridine

DMF – *N,N*-dimethylformamide

DMSO – Dimethyl sulfoxide

DPV – Differential pulse voltammetry

DTU – Technical University of Denmark

ECUST - East China University of Science and Technology

EDC – *N*-(3-Dimethylaminopropyl)-*N'*-ethylcarbodiimide

EtOAc – Ethyl acetate

FRET – Förster resonance energy transfer

GCE – Glassy carbon electrode

GO – Graphene Oxide

IR – Infrared spectroscopy

HOMO – Highest occupied molecular orbital

ISM – Ion selective membrane

IUPAC – International Union of Pure and Applied Chemistry

LUMO – lowest unoccupied molecular orbital

Me – Methyl

MWCO – Molecular weight cut-off

NMP – *N*-Methyl-2-pyrrolidone

NMR – Nuclear magnetic resonance

Pr – Propyl

RGO – Reduced graphene Oxide

RPM – Rounds per minute

RT – room temperature (in reaction only)

SCE – Saturated calomel electrode

SDU – University of Southern Denmark

SHU – Shanghai University

STM – Scanning tunnelling microscopy

TEM – Transmission electron microscopy

TBA – Tetra-n-butyl ammonium

TTF – Tetrathiafulvalene

TGA – thermal gravim analysis

THF – Tetrahydrofuran

TLC – Thin-layer chromatography

TNB – 1,3,5-trinitrobenzene

UV-vis – Ultraviolet-visible

XPS – X-ray photoelectron spectroscopy

XU – Xiamen University

XRD – X-ray Diffraction

Motivation

The detection and monitoring of chemical compounds is of tremendous importance in a number of important areas in our society[1]. Chemical species such as ions and small molecules have for example important roles in our body functions, and detection and monitoring of these compounds are therefore crucial for always accurate medical diagnostics[2,3]. Most important targets can be detected today, but there is intense interest in better, faster and cheaper systems[4,5]. Especially cheap disposable detection units for use in resource-limited environments and disaster zones are a pressing concern[6–8]. The growing environmental awareness also increases requirements of chemical sensors to monitor environmental systems such as water supplies, air quality, underground and so forth[9,10].

Graphene-like materials such as RGO and chemically modified graphene (CMG) show high promise for electrochemical sensing due to their high surface area, high conductivity and low production cost with easy up-scaling. They have, therefore been used extensively in sensor manufacturing[11–13]. However, these materials themselves have limited selectivity. Hybrid structures are therefore prepared mostly with enzymes in biosensor manufacturing, but the stability and high cost of enzymes can be obstacles limiting their usefulness. Supramolecular moieties have, however been used for decades as receptor units for chemical sensors, and serve as a strong alternative to enzymes for introducing increased levels of selectivity to graphene-like materials [14–18]. Despite comprehensive research in graphene materials for sensing applications, there is, however still ample opportunities within graphene materials functionalized by supramolecular moieties, so much the more as most current work in the field use physical adsorption rather than covalent attachment, which would be expected to add to more robust and reproductive sensing[19–25].

This project is focused on covalent functionalization of graphene-like materials with supramolecular moieties in the preparation of novel sensing materials. We used two strategies towards this goal. One was to functionalize graphene oxide (GO) efficiently with supramolecular moieties, and then reduce it to a RGO based CMG. The other approach was to synthesize a RGO material with a chemical handle, which can be used post in reduction to functionalize the RGO. This approach serves to spare the supramolecular moiety from potential unwanted chemical transformation during the reduction step.

Chapter 1   Introduction

This chapter provides a brief introduction to the concepts essential for the thesis, including chemical sensors, nanostructures, and supramolecular chemistry.

1.1   Chemical Sensors

Evolutionarily, one of the key factors for survival is the ability to use our human senses to observe and react to changes in the environment, from visual to auditory, but also chemical sensing. This is why we are capable of detecting more than 10 000 different odorants despite humans being primarily visual and underappreciate olfactory sensing[26]. Likewise, our society has a growing appreciation of the importance of chemical detection. From the general public to government and industry there is an ever-expanding urge to understand our chemical and biological environment[1].

Chemicals in general, from toxins to simple ions, have tremendous impact on our bodily functions, health and diseases. The detection or monitoring of specific compounds or ions in our body therefore offers crucial clues for medical diagnostics[2,3]. The increase in environmental awareness also implies a growing need for adequate detection of chemicals in our environment, such as water supply or air quality[9,10]. Chemical sensors for explosives,[27] and chemical warfare agents[28] are also increasingly important in controlling previous warzones, air security, and other security risk areas.

In general, a sensor is a device that can detect and convert an external stimulus into a readable output. For example, a motion sensor can detect motion and convert this stimulus into a signal such as an alarm or electrical recording. A chemical sensor is a sensor, which can recognize a specific chemical and give an analytically useful output signal allowing us to identify and possibly quantify this specific compound in a mixture of many compounds.

A chemical sensor is in itself not a sensing device or an analyser, but rather an essential component of such devices. In order to construct an operational device further components are required: signal processing unit (detector, amplifier and/or signal transformation), data

processing unit (reference sample or database), and monitor for readout. Further components can be added to improve the system; these include but are not limited to sampling unit (auto sampler), sample transport (stirring or flow device)[29].

Chemical sensors have two primary functional criteria: one is selectivity; being able to selectively recognize a specific compound out of a mixture, either by a receptor picking out specific property or compound or by a separator such as a membrane only allowing specify compounds through. The other criteria is transduction, having the ability to transduce a stimulus into a readable signal. A number of types of signals can be generated, depending on the transducers used. The signal can be optical such as colorimetric[30], fluorescent[31] and circular dichroism[32]; or electrochemical including potentiometric[33], amperometric[34] and conductometric[10]; or thermometric[35] etc.

Due to these two central components required, one rational design of a sensor is to have a recognition unit or binding site covalently linked to a probe also called the "receptor-spacer-reporter approach"[36] (Figure 5). This is regarded a recurring design for synthetic molecular sensors[37].
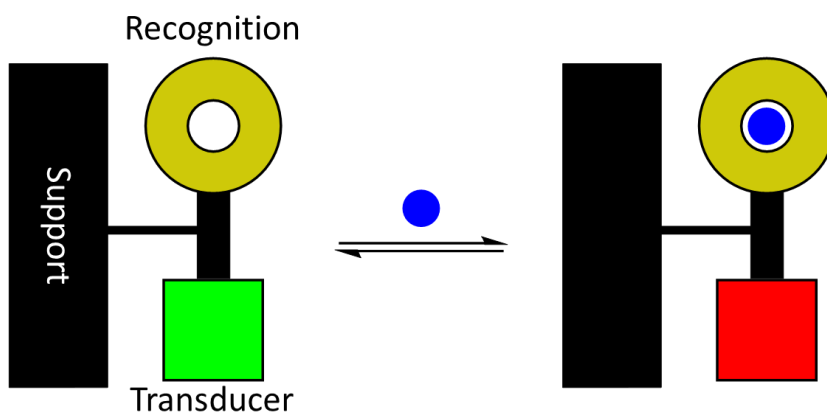
Figure 5: Schematic of supported "receptor-spacer-reporter" type sensor.

Support for a chemical sensor is also important. If the chemical sensors work as homogeneous sensors, the re-use could be very complicated if not impossible. However, if the sensor can be immobilized on a surface, it can then be cleaned and re-used. Supporting the sensor also opens the possibility of using it for continuous monitoring via heterogeneous flow devices[38]. A sensor for gaseous detection also requires a heterogeneous interface where the support material becomes important. It is important to make sure that the material does not interfere with the signalling type when using a support material, e.g. if a fluorescence probe is used, the support should not quench the fluorescence, or if an electronic signal is used the support needs to be electronically conductive to carry the signal through the material.

There are two main ways to achieve a high selectivity for chemical sensors. One is direct sensing and has its origin in "the lock and key principle" first postulated by Emil Fischer in 1894[39]. In "the lock and key principle" a recognition unit has a very high affinity towards one specific compound thereby generating a one-to-one relationship between stimuli and sensor output. Examples of such an approach are biological signalling receptors such as seven-transmembrane receptors[40], antibody recognition systems[41], synthetic sensors[36] or molecular imprinting[42]. The advantage of this approach is a one-to-one identification of a compound, resulting in very high selectivity for sensors, perfectly matched to the compound. The drawback is that some compounds are extremely similar and a perfect sensor can be hard if not impossible to achieve. Even in biology, systems that have evolved over millions of years can be tricked. The basis of most medicinal chemistry is to find alternative molecules to trigger certain receptors. Another potential drawback is the need of one unique sensor for each compound.

The other approach is to construct a sensory array, which has its origin in olfactory sensing. Where a series of sensors are arrayed, each sensing different properties, the collective signal fingerprint can then be analysed in order to identify the specific compounds. The benefit of array sensing is that the use of many sensors enables detecting an even larger library of compounds, by using the data from each receptor to piece together the overall detection of all the compounds. One drawback of such a system is its inherent complexity, as multiple receptors are needed that together create a complete array. Another drawback is that two or more compounds in a mixture of compounds can be interpreted as a single one and thereby give positive detection where it should give a negative result.

1.2   Nanotechnology and Nanochemistry

Richard Feynman first introduced the idea of engineering at the nanoscale that later inspired nanotechnology. December 29, 1959, he presented the now famous and popular words: *"there is plenty of room at the bottom"* at the annual meeting of the American Physical Society, at California Institute of Technology[43]. Back then the tools needed to manipulate materials at the nanoscale were not available, so his talk was purely speculative. The message of this talk was that the laws of physics do not prevent the manipulation of single molecules or atoms and the reason this was not achieved was lack of appropriate methods. We now know that he correctly predicted these would inevitably arrive. He also advocated for the potentials of nanoscale technology in storage of information and computer technology. Looking at the progress in these fields over the last few decades, his advocation was definitely warranted. However, even today we are still not at his imagined limits.

"Nano" comes from Greek word "*nanos*" meaning "dwarf". Now it is used as a prefix describing a billionth (10^{-9}) of a measuring unit. Nano in nanotechnology refers to the size

scale nature of the technology, further specified by the European Commission definition of nanomaterials in 2011[44]:

> *"A natural, incidental or manufactured material containing particles, in an unbound state or as an aggregate or as an agglomerate and where, for 50 % or more of the particles in the number size distribution, one or more external dimensions is in the size range 1 nm – 100 nm."*

What we readily observe is in the macroscopic scale (10^3 – 10^{-3} m). Zooming into the microscopic scale (10^{-3} – 10^{-6} m), biological cells and cellular organelles are visible by optical microscopes. Further beyond the microscopic scale is the nanoscale with single molecules and molecular clusters (Figure 6). To observe nanoscale objects, the crucial development of advanced microscopic techniques such as transmission electron microscopy (TEM) by Ernst Ruska in the 1930s[45] and scanning tunnelling Microscopy (STM) by Gerd Binning and Heinrich Rohrer in the 1980s[46] who later jointly got the Nobel prize in 1986[47]. Later the atomic force microscopy developed by G. Binning, C.F. Quate and Ch. Gruber in the 1980s joins the list of important microscopy techniques for the observation of objects at the nanoscale[48].

Beyond the sheer size difference between the macroscopic scale and the nanoscale some physical and chemical phenomena also change in this size range due to decreased effects of gravitation, coulombic forces dominating, increased importance of quantum mechanical effects, faster electron/ion transport, stronger effects of Brownian motion etc.[49,50]
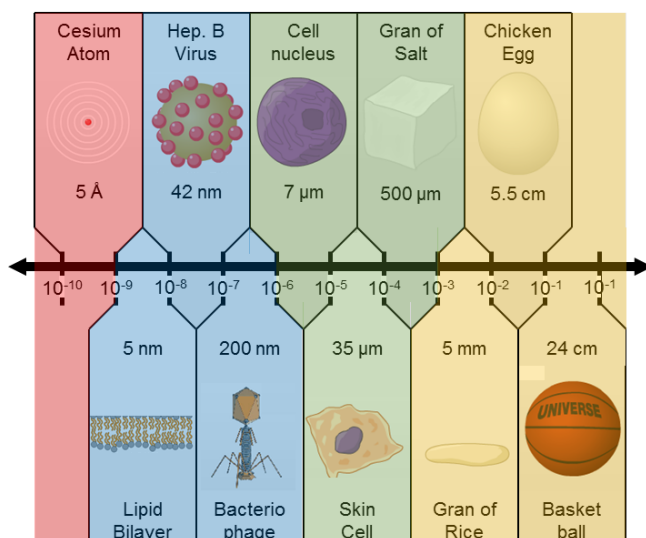
Figure 6: Depiction of the size regime from macroscopic (yellow) through microscopic (green) to the nanoscale (blue) and beyond, with examples of objects the size of which diminish roughly by a factor of ten. This figure is adapted from an interactive figure by Cary & Michael Huang[51].

Nanostructures exist in a multitude of shapes[52,53] from 0D structures such as roughly spherical nanoparticles[54], nanoflowers[55] etc., to 1D structures[56] such as nanotubes, rods or wires, to 2D structures[57] such as nanodiscs or nanosheets. Furthermore, nanostructures can be composed from a huge number of materials or combination of materials making the diversity of nanomaterials almost endless. Their properties often depend on all of these three key factors, i.e. size, shape and composition.

In principle, there are two main approaches to manufacture nanomaterials. One is the top-down approach of traditional workshop manufacturing in microfabrication methods, where tools are used to cut, mill, shape edging, and evaporating materials into desired shapes and functions[58].

The other approach is bottom-up, where nanomaterials are synthesized from smaller components. This can be thought of as the chemical approach of building up with atoms and molecules.[54–56] Advances in STM[59] or AFM[60] techniques have also made it possible to do as Feynman envisioned in engineering the motion of single atoms or molecules with the tip to generate nanostructures.

1.3   Supramolecular Chemistry

Jean-Marie Lehn first described the concept of supramolecular chemistry in 1978[61]:

> *"Just as there is a field of molecular chemistry based on the covalent bond, there is a field of supramolecular chemistry, the chemistry of molecular assemblies and the intermolecular bond."*

The Nobel prize in chemistry 1987[62] was awarded to Donald J. Cram, Jean-Marie Lehn and Charles J. Pedersen for their work on supramolecular chemistry, specifically supramolecular hosts: spherands, cryptands and crown ethers[63]. After the Nobel Prize award, Jean-Marie Lehn further detailed his description of supramolecular chemistry[64]:

> *Supramolecular chemistry may be defined as "chemistry beyond the molecule," bearing on the organized entities of higher complexity that result from the association of two or more chemical species held together by intermolecular forces. Its development requires the use of all resources of molecular chemistry combined with the designed manipulation of noncovalent interactions so as to form supramolecular entities, supermolecules possessing features as well defined as those of molecules themselves. One may say that supermolecules are to molecules and the intermolecular bond what molecules are to atoms and the covalent bond.*

In terms of the definition, it can be said that supramolecular chemistry adds an extra level of complexity to traditional synthetic chemistry where clusters of traditional molecules can be assembled into larger architectures. These advanced systems find many applications e.g. as

functional materials[65], sensors[36], self-assembly[66] and molecular machines[67]. Some of the major differences between traditional synthetic chemistry and supramolecular chemistry are summarized in Table 1[68].

Table 1: Summary of differences between covalent bonds and supramolecular interactions
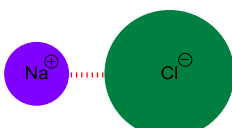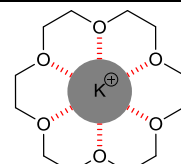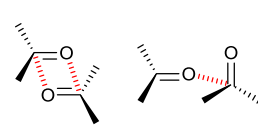
	Covalent Bond	Supramolecular interaction
Constituent bond type	Covalent	Ionic, hydrogen bond, π–π and hydrophobic interaction
Bond strengths	150 – 1075 [kJ mol^{-1}][69]	0 – 350 [kJ mol^{-1}][68]
Kinetic stability	Kinetically stable	Kinetically reversible
Contribution to ΔG	ΔH dominated	ΔH and ΔS Comparable
Solvent dependence	Secondary	Primary

1.3.1 Host-Guest Complexes

Host-guest complexation is one of the key subfields of supramolecular chemistry, which focus on designing large host complexes for recognition and binding of smaller guests such as cations[70,71], anions[72,73], or small neutral compounds[74,75]. The molecular host is designed so that direction specific interactions help to selectively bind the target compound and often have a size-limiting cavity or binding site.

1.3.2 Intermolecular Interactions

Table 2: Electrostatic interactions, and their strength and range/direction dependency.

Interactions	Ion – Ion	Ion – Dipole	Dipole – Dipole
Example	Na$^+$ Cl$^-$	K$^+$⊂18-crown[6]	Carbonyl bonding
Strength[68]	100 – 350 kJ mol^{-1}	50 – 200 kJ mol^{-1}	5 – 50 kJ mol^{-1}
Range dependency	R^{-1}	R^{-2}	R^{-3}
Directionality	No	Yes	Yes

There are several different types of intermolecular interactions: the most important ones are briefly described here. Most of these are electrostatic interactions governed by coulombic forces, the most common of which are listed in Table 2.

The hydrogen bond is an intermolecular interaction of high importance in chemistry, physical chemistry and biochemistry[76–79]. It is now more than 100 years[80] since the discovery of the hydrogen bond by T. S. Moore and T. F. Winmill[81]. Since then very much has been learned about the nature of the hydrogen bond and it has proven a quite complex interaction. As a result International Union of Pure and Applied Chemistry (IUPAC) has recently (2011) recommended a new definition of the hydrogen bond[82,83]:

> *The hydrogen bond is an attractive interaction between a hydrogen atom from a molecule or a molecular fragment X–H in which X is more electronegative than H, and an atom or a group of atoms in the same or a different molecule, in which there is evidence of bond formation.*

A hydrogen bond is primarily an electrostatic interaction of the dipole – dipole type, but many reports show it also involves partial charge-transfer (below) interaction leading to partial covalent bond and dispersion forces[76,77].

π–π interaction is electrostatic mutual polarization interaction between π systems typically aromatic rings. There are two types of attractive π–π interactions; face-to-edge and face-to-face (Figure 7). Face-to-face interaction is mostly between offset rings rather than directly superimposed rings. This is because π–π electron density interactions between electron poor and electron rich π-systems are enhanced[84] (blow).
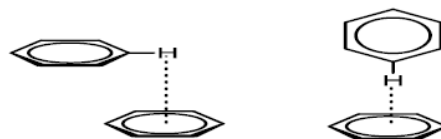
Figure 7: Interactions between aromatic π- systems A) Face-to-face; B) Face-to-edge.

Van der Waal's interactions can be divided into two different forces attractive dispersion (London) forces and exchange-repulsion. The dispersion arises from electrostatic interaction between temporary polarizations of the electron cloud, inducing a small dipole moment. The point interaction decreases with increasing distance as r^{-6}. Exchange-repulsion is the force that prevents atomic overlap and decreases with increasing distance as r^{-12}.[85]

Charge transfer (CT) interaction is an attractive interaction between an electron donor and an electron acceptor, where the energy gap between occupied molecular orbitals of the donor and unoccupied molecular orbitals of the acceptor is relatively small. In a CT complex the donor and acceptor orbitals mix into new complex orbitals. This is often but not necessarily always a (HOMO – LUMO) interaction[84]. The new complex orbitals have a lower lying occupied orbital with a higher electron density around the acceptor resulting in partial

electron transfer from donor to acceptor and a stabilizing energy. Charge transfer complexes are often highly coloured due to photo-induced charge transfer excitation between mixed orbitals and often lie in the visible area π-π interaction below to this category of supramolecular interactions[85–87].
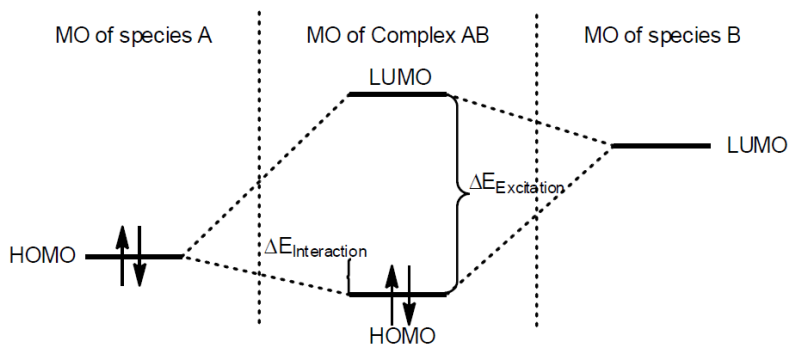
Figure 8: Illustration of an energy diagram of a HOMO – LUMO dominated CT-complex, showing the CT-stabilization energy $\Delta E_{Interaction}$ and the CT excitation band energy $\Delta E_{Excitation}$.

Solvation effects are governed by the interaction between the solvent with itself and with the solutes, and can have tremendous effect on the supramolecular complex stability as well as aggregation. If the interaction between solvent and solute is strong, e.g. a sodium ion in water, a solvation sphere will form. In order to make a complex where the sodium ion is included, these strong interactions must be broken, so the solvent effects work against the formation of the complex. If the interactions between solvent and solute are similar to those between solvent molecules themselves, this effect is less important[68]. In the other extreme, if the interaction between solute and solvent is weaker than the interaction among the solvent molecules e.g. hexane in water, there will be a different type of solvation sphere. This sphere consists of high-energy solvent molecules, which can be released if the solute can be encapsulated by a host molecule or by aggregation. Solvation thus contributes significantly to complex formation[68].

Chapter 2   Graphene-Like Materials

Throughout the work of this Ph.D.-study the materials used are two-dimensional carbon materials. This chapter focuses on introducing graphene and graphene-like materials, their properties, and advantages for applications as sensor materials. A modified version of the chapter has been provisionally accepted as a book chapter in "Nanomaterials and Nanotechnology" by "One Central Press" co-authored by Arnab Halder and Qijin Chi. The work done by Arnab Halder on biosensors is not included in this chapter[88].

Graphene is a single atomic layer of graphite (Figure 9). First discovered five centuries ago in Borrowdale[89], graphite is a black, soft and mechanically weak material. Initially, graphite was used for marking sheep, before it has found its practical application for military purpose as a heat resistant solid lubricant for canon ball molding[2]. Since then, graphite has been used for a variety of applications from pencils to nuclear reactors[90]. As a freestanding material graphene has been discussed theoretically for more than 60 years[91–93]. Yet it was widely believed to be too unstable to exist[94–96]. However, in 2004, Novoselov, Geim and co-workers[97–99] demonstrated that graphene can be obtained by mechanical exfoliation using a scotch tape on graphite, and these graphene sheets are stable enough for characterization. In 2010, Novoselov and Geim were awarded the Nobel Prize[100] in physics for their pioneering work and following studies of graphene and its unique properties.
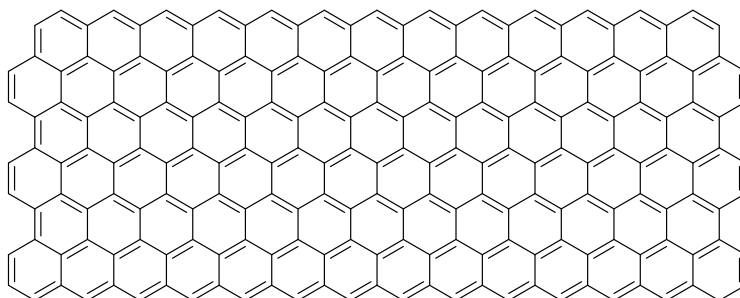
Figure 9: Hexagonal network of sp^2 carbon, the chemical structure of graphene.

After the discovery by Novoselov and Geim, a new area of research on graphene has quickly sparked, and received tremendous attention in the scientific community, and has grown rapidly ever since.

2.1   Properties of Pristine Graphene

The structure of graphene is an atomically flat hexagonal pattern of sp^2-hybridized carbon with a bond length of 1.42 Å. The theoretical specific surface area is tremendously large (2630 m^2/g) or 5.25Å^2 per carbon atom[101]. The conjugated π-system of delocalized electrons gives rise to its remarkable electron mobility and optical properties. The low opacity ($\approx$ 2.3 %) of graphene makes it optimal for devices where optical transparency is needed[102]. AFM via nano-indentation was used to study the mechanical properties of freestanding single-layer graphene membranes suspended over holes on a Si substrate[103]. These experiments showed graphene to be the strongest material ever discovered. However, thickness is a determining factor for mechanical strength. Graphene also has high thermal conductivity measured as 600 W m^{-1} K^{-1} on a SiO$_2$ support[104], and even as high as 5000 W m^{-1} K^{-1} for suspended graphene[105]. Its electronic properties are, however, most impressive, particularly high electron mobility. Novoselov *et al.*[97–99] reported the electronic mobility of SiO$_2$ supported graphene at room temperature to be $\approx$ 2000-15 000 cm^2 V^{-1}s^{-1}. Bolotin *et al.*[106] measured even higher electron mobility of suspended graphene extensively cleaned to remove impurities reaching 230 000 cm^2 V^{-1}s^{-1}, which shows that as for thermal conductivity, electronic mobility is also strongly affected by the support material. Graphene also exhibits a range of quantum effects, including ballistic transport of electrons on the sub-micrometer scale up to $\approx$ 0.3 μm at 300 K[96], quantum hall effect at room temperature[107,108], zero energy band gap, and electrons traveling across the conjugated π-system can be described as mass-less Dirac fermions[99]. All these unique properties are highly dependent on the quality, purity, and grain boundaries in graphene sheets.

2.2   Methods of Synthesis

The first graphene nanosheets were obtained by micro-mechanical exfoliation also called *"the scotch tape method"*. However, other synthesis methods are needed due to the scalability limitations of this micro-mechanical exfoliation approach. Some of these other methods are outlined below.

2.2.1   Bottom-Up Growth of Graphene

Chemical vapour deposition (CVD) and epitaxial growth on SiC can be used to grow graphene on a substrate from the bottom-up making high-quality large-area graphene sheets.

However, epitaxial growth is hardly suitable for large-scale production, due to the need for atomically flat SiC requiring cumbersome preparation. Transfer of graphene sheets from SiC is also complicated[109].

On the other hand, CVD growth has proven to produce very large single graphene sheets, among which the most notable report is of a 30-inch roll-to-roll graphene film by Lijima *et al.*[110] (Figure 10). Flexible Cu foil substrate was used to grow the graphene monolayer sheets, which were then stacked layer by layer to form four-layer films with 90% transparency and a surface resistance of 30 Ω sq^{-1}.
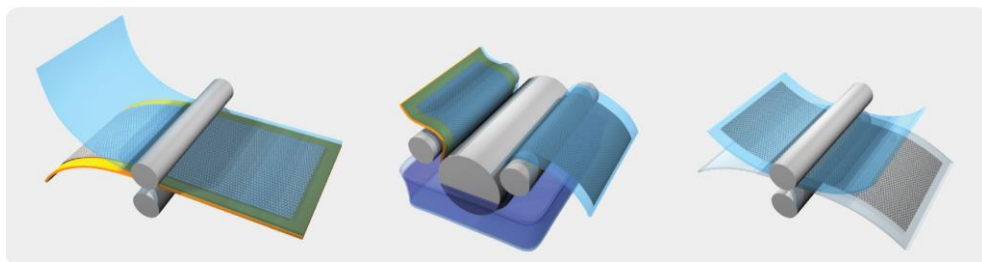
Figure 10. Schematic illustration of roll-based graphene grown on Cu foil reported by Lijima *et al.* (reproduced with permission from ref.[110] Copyright 2010 Macmillan Publishers Limited.)

In CVD, a gaseous carbon source usually consisting of methane and hydrogen gas is heated to high temperatures (800 – 1500 ºC) to break C–H bonds in order to form atomic carbon, which then forms graphene on the substrate surface. Catalytic metals are often needed[111] to reduce the required heat. The supports used are most often transition metals,[112] especially Cu[113] and Ni.[114]

The most concerning challenge in growing graphene is the presence of grain boundaries resulting in polycrystalline graphene sheets[115,116] as a result of multiple nucleation sites. These grain boundaries reduce the outstanding properties of graphene.[117,118] Another limitation is high energy requirements, resulting in a very costly industrial scale production.[112] Finally, it is challenging to safely lift the grown graphene from the substrate, a process that can easily damage the structure of graphene sheets.

2.2.2   Top-Down Exfoliation of Graphite to Graphene

Another approach to potential large-scale production of graphene is solvent exfoliation (Figure 11). The main challenge is to completely separate graphitic layers to monolayer graphene. Vigorous sonication for extended time can be used to break the weak interaction between graphene layers. The separation can be stabilized by minimizing the solid/liquid interfacial tension, thereby facilitating the separation and preventing from re-aggregation.[119] In order to minimize the interfacial tension, the surface energy of the solvent and graphene should be approximately at the same level. The surface energy of graphene is predicted to be

approximately the same as that for nanotubes and graphite (70 mJ m^{-2})[120] corresponding to a surface tension of ($\gamma \approx 40$ mJ m^{-2})[120]. The most effective solvents for dispersion of graphene include *N*-methyl-2-pyrrololidone (NMP) $\gamma = 40.25$ mJ m^{-2};[121] *N,N*-dimethylformamide (DMF) $\gamma = 39.07$ mJ m^{-2};[122] and dimethyl sulfoxide (DMSO) $\gamma = 41.76$ mJ m^{-2}.[122]
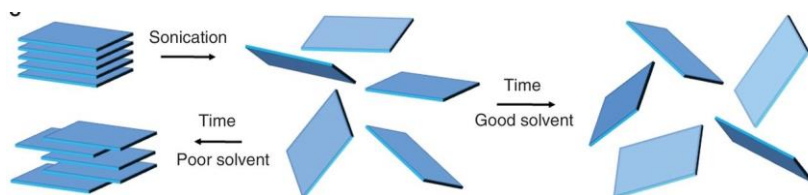
Figure 11. Schematic illustration of basic principles in liquid exfoliation.

Exfoliation in NMP by long-time sonication was reported to achieve high concentration of ≈ 1 mg mL^{-1}, where about 25% of the sheets are mono-layer and the majority < 5 layers [123]. The exfoliated graphene was reported to be up-concentrated to stable dispersions of 20 mg mL^{-1}.[124] The use of these solvents could be, however, problematic due to their toxicity[125,126] and high boiling points.

The high boiling point makes it difficult to completely remove residual solvent, which is why several attempts using less toxic and lower boiling solvents have been performed. Water is an ideal solvent from an environmental point of view. However, the problem with water is its high surface tension[127] $\gamma = 71.99$ mJ m^{-2} resulting in very poor interfacial interactions with the hydrophobic surface of graphene, making it almost impossible to exfoliate graphite into graphene in pure water. There are some reports with limited success using other polar organic solvents such as ethanol, acetone and acetonitrile[128].

Surfactants have been extensively studied[128] to facilitate exfoliation in water. Intercalating surfactants such as pyrene salts are of particular interest and have been used e.g. by Green and co-workers[129] to stabilize dispersion of graphene in water at 0.8–1.0 mg mL^{-1}. Polymers have also attracted attention to stabilize graphene in aqueous dispersion[128].

The main benefit of exfoliated graphene over grown graphene is a small number of crystal defects, as it originates from large crystalline graphite samples. Additionally, scaling up solvent exfoliation is less problematic. The disadvantage is due to long-term sonication giving relatively small ≈ 1 µm^2 produced graphene sheets[130,131]. Another problem is polydispersity. This problem was, however, largely solved by Green and Hersam[132]. They showed that density gradient ultra-centrifugation (DGU) can be employed to efficiently separate single-layer, double-layer, and multi-layered graphene.

Finally, residual solvent and other impurities can be problematic to be removed completely, therefore reducing the electrical properties of the product.

2.3 Graphene Oxide and Reduced Graphene Oxide

The particular method discussed here is wet-chemical exfoliation by sequential oxidation, exfoliation and reduction of graphite into a graphene-like material, i.e. RGO. This method is arguably the most effective approach for large-scale production, due to easy scale-up of the process. However, the reduction is not a complete recovery process, as the final product RGO contains significant amounts of structural defects.

Graphite oxide was first synthesized and studied by Brodie already in 1859[133]. Brodie's original interest was to determine the molecular formula of graphite, later he further studied the properties of graphite oxide. Brodie used $KClO_4$ in fuming nitric acid for the oxidation of graphite. Brodie carried out the oxidation over four individual reactions, achieving graphite oxide with a C:O ratio of $\approx$ 2:1 and observed that the graphite oxide was dispersable in water. However, he did not know that this was because graphite oxide readily exfoliates in water (Figure 12). Thus, he could not realize that he was working with what was properly the first ever two-dimensional material of atomic height suspended in water. Later the method of making graphite oxide was improved first by Staudenmaier in 1898[134] and then further by Hummers and Offeman in 1958[135]. "The Hummer's method" often slightly modified is today the most common method for preparation of graphite oxide. Here, $KMnO_4$ oxidizes graphite in sulfuric acid in a single step. All these methods can achieve approximately the same ratio of carbon to oxygen (C:O $\approx$ 2:1).
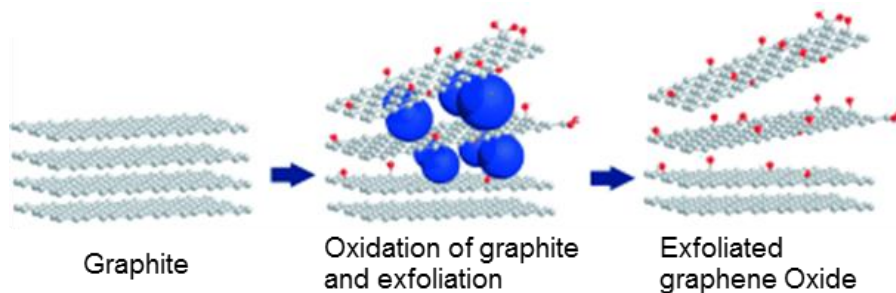
Figure 12. Schematic representation of oxidation and exfoliation of graphite into GO (reproduced with permission from ref.[136] Copyright Wiley-VCH Verlag GmbH & Co. KGaA, Weinheim)

The structure of graphite changes significantly during oxidation of the sp^2 carbon network, by transforming into mostly sp^3 covered with oxygen functionalities. This completely interrupts electron transport in the material, making graphite oxide or GO be an insulator in solid state. However, new interesting properties arise from this transformation. The chemical reactivity of GO is high, making it easy to be modified chemically (section 2.4.2 page 20). Graphite oxide is readily exfoliated in slightly acidic, in neutral and in alkaline aqueous solutions at high concentration (Figure 12). This is attributed to a strong interaction between

the oxygen functionalities and water, allowing water to intercalate,[137,138] with subsequent separation of the sheets in solution. Separation is further helped by electrostatic repulsion, due to a net negative charge of GO mainly arising from carboxylic acid edge groups.[139]

The exfoliation still needs to be assisted by either sonication or intensive stirring. Sonication is a more effective method but it can cause fracturing of GO sheets.[130,131] Graphite oxide can also be exfoliated in other polar solvents, such as ethylene glycol, DMF, NMP and tetrahydrofuran (THF).[140] High-speed centrifugation can separate exfoliated GO layers from stacked graphite oxide.

GO is not a defined material like molecules but rather a mixture of materials with different sheet size, oxidation level, and specific functional groups on basal plane and edges. This depends on a number of parameters some of which cannot be fully controlled, resulting in batch-to-batch variations. Detailed studies of GO are therefore problematic due to variation in conditions such as heat, oxidant, acid, graphite source and so forth.[141]

Dimiev et al.[142] discovered that post-reaction work-up also has significant impact on the GO product, showing that the normal water work-up effectively changes the reactive properties of GO. They performed experiments using organic solvent for the post reaction work-up. The resulting solid product was not a grey but a yellow, and in some cases white graphite oxide. They hypothesized that epoxides or covalent sulfur species dominate the sp^3 hybridized basal plane after oxidation of most of the basal planes. These can be hydrolysed to some extent under aqueous work-up and thus partially restore sp^2 hybridization resulting in an increased absorption of light.

2.3.1 Structure of Graphene Oxide

The chemical structure of graphite oxide has been debated and studied extensively in the scientific community for several decades. Its exceeding complexity stemming from non-stoichiometry, amorphicity and sample-to-sample variations makes precise characterization very difficult.

Several models of graphite oxide have been proposed throughout the years e.g. by Hofmann[143], Scholz-Boehm[144], and Nakajima-Matsuo[145]. All of these had regular lattices and compositions. Now it is, however, established that the structure of GO is truly amorphous. The currently most accepted model was proposed by Lerf and Klinowski[146], based on solid-state NMR spectroscopy of graphite oxide (Figure 13).
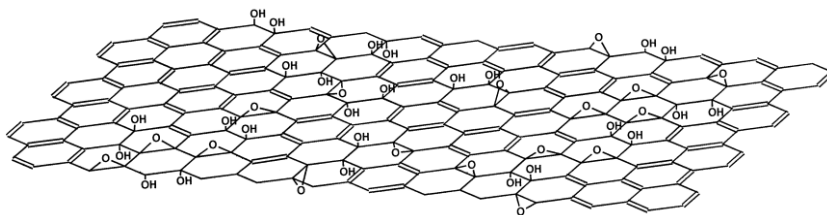
Figure 13. Structural model of graphite oxide proposed by Lerf and Klinowski[147] **(reproduced with permission from ref.**[147] **Copyright 1998 Elsevier Science B.V)**

The NMR studies show functionalities of tertiary alcohols (δ = 60 ppm), epoxides (δ = 70 ppm) and alkenes or aromatic functionalities (δ = 130 ppm) confirming previous models based on reactivity studies. However, the study does not elucidate the distribution of these groups nor fully explain whether the alkenes are separated or clustered in conjugated or aromatic assemblies[148].

Based on further synthesis studies by Lerf *et al.*[146] showed that isolated double bonds would not resist the strongly oxidative media thus concluding that aromatics or part of conjugated systems must be the sources of the δ = 130 ppm peaks.

2.3.2 Reduction of Graphene Oxide

Easy availability of 2D-structure coupled with the loss of electronic conductivity upon oxidation of graphite makes the reduction of GO into graphene a key interest in graphene research. Unfortunately, full reduction seems impossible. The electronic and material properties of RGO therefore do not match the unique properties reported for pristine graphene. However, electronic properties can be partially restored by reduction into RGO[149].

Despite less impressive properties, the low production cost of RGO makes it a good candidate for many of applications proposed for graphene[150]. Furthermore, the step through GO makes it possible to functionalize RGO much more easily than graphene (2.4 page 16). GO can thus be reduced by a long list of different methods[150].

The most common method of reduction is reduction by hydrazine monohydrate first reported by Ruoff and co-workers[151]. Being stable in water hydrazine has an advantage over most other strong reducing agents. Reduction by hydrazine effectively removes most of the oxygenated functional groups and largely restores the sp^2 hybridization, although some structural defects and residual functional groups are still present in the RGO. The sheet conductivity is restored to 780 kΩ sq^{-1}.[152] Hydrazine reduced RGO has an oxygen content around C:O = 10:1.[151] The main carbon species left as determined by either NMR spectroscopy or XPS is C=C, while some COO$^-$ groups are retained at the edges.

The primary disadvantage of hydrazine is unintentional introduction of nitrogen functionalities such as amines. These commonly seen nitrogen functionalities can amount to C:N = 16:1.[151]

Sodium borohydride ($NaBH_4$) can be used for more efficient reduction of GO, though $NaBH_4$ being unstable in aqueous solution. Due to the kinetically slow decomposition, it can still be used for aqueous reduction of GO. Reduction of GO by $NaBH_4$ reduces the sheet resistance to 59 kΩ sq^{-1} significantly lower than hydrazine-reduced RGO sheets[152].

Other environmentally safe methods of reduction using mild reducing agents such as ascorbic acid have also been reported[153,154]. These methods are less effective than hydrazine and $NaBH_4$ but can be useful in specific cases. *In situ* generated H_2 from metals in acid has also been reported to reduce GO[155,156]. Interestingly, strong alkaline solution without reducing agent also results in certain reduction[157]. High-temperature thermal reduction ($\approx$ 1000 °C)[158] is another highly used method of reducing GO, sometimes in combination with H_2 atmosphere. Under these conditions, oxygen is released from the graphene sheets in the form of CO or CO_2 leaving behind structural defects[159]. In spite of existing defects, the bulk conductivity can be enhanced to 1000 – 2300 S m^{-1}.[160]

2.4 Functionalization of Graphene Materials

In the field of sensors based on graphene materials, it is important to introduce chemical functionalization, to generate selective binding to the sheet surface. This can be done either through non-covalent attachment[161] or by covalent functionalization of edges or basal plane sites. The latter is the focus of this work. Functionalization is, notably much feasible on GO (section 2.4.2 page 20) or RGO (section 2.4.3page 22) than on pristine graphene (Figure 14).
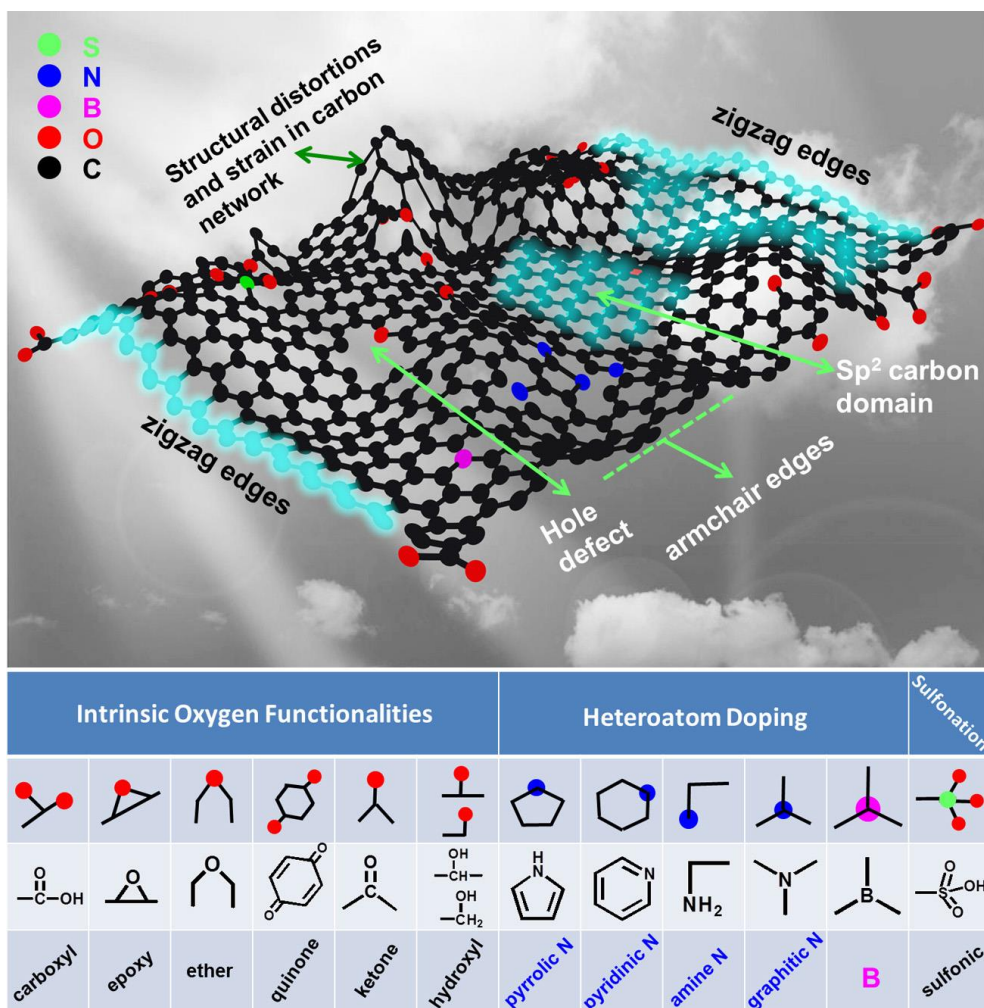
Figure 14. General schematic model illustrating possible active sites for functionalization in graphene, oxidized graphene and doped graphene. (Reproduced from ref[162] with permission, Copyright 2014 Elsevier B.V.)

2.4.1 Functionalization of Pristine Graphene

Edge functionalization is feasible because carbons with unpaired electrons and edge defects increase the reactivity of the otherwise inert graphene[163–165]. This can be used to improve solubility and change assembly behavior[166]. Edge functionalization leaves the sp^2 network intact and therefore, does not radically change electronic properties such as electron mobility. However, as functionalization is limited to edges functionalization and can only reach a limited extent.[163]

Basal plane functionalization on the other hand, is difficult due to high-energy bonds C–C that need to be broken, and the structural change from planar sp^2 to tetrahedral sp^3. Such reactions require highly reactive intermediates[167]. These kinds of functionalization also change the π-conjugation and therefore directly affect the electronic properties of graphene. Functionalization is thus a trade-off between new functionalities and the existing properties.

Free-radical reactions are one of the effective ways to functionalize the basal plane. Diazonium salts are usually used to generate carbon radicals, which react with the chemically inert graphene[168,169] (Figure 15A). Inspired by functionalization of related carbon materials such as C_{60} and nanotubes, cycloaddition reactions have developed into a widely used method for graphene modification. [1+2] cycloaddition reaction of a highly reactive carbene[170,171] or nitrene[172,173] to a graphene double-bond forming a 3-membered ring is an example (Figure 15B&C). In a similar fashion, *in situ* generation of ylides can undergo [2+3] dipolar cycloaddition forming a more stable 5-membered ring perpendicular to the basal plane[174–176] (Figure 16A). Finally, a Diels-Alder cycloaddition can be used to form a 6-membered ring where graphene can act as either the diene or the dienophile[177,178] (Figure 16B).

Despite the availability of multiple reaction pathways for functionalization of graphene, all of them require highly reactive intermediates, which can become problematic if the desired functional groups are also reactive.
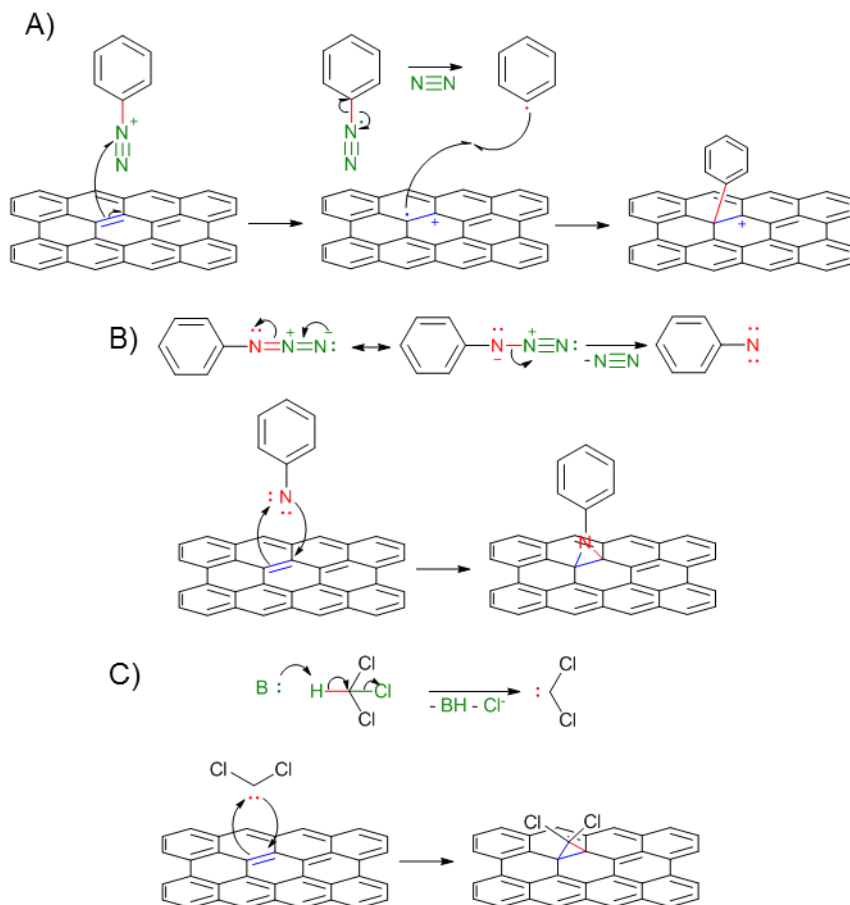
Figure 15: Schematic mechanisms of the reactions described in the text: A) phenyl functionality added to pristine graphene through radical addition, initiated by Diazonium salt by production of free N_2. B) Phenyl functionality added to pristine graphene by *in situ* formation of nitrene from azide, which reacts with graphene in a [1+2] cycloaddition. C) Base induced formation of carbine, to react in a [1+2] cycloaddition with graphene in order to attach a dichloromethylene functionality.
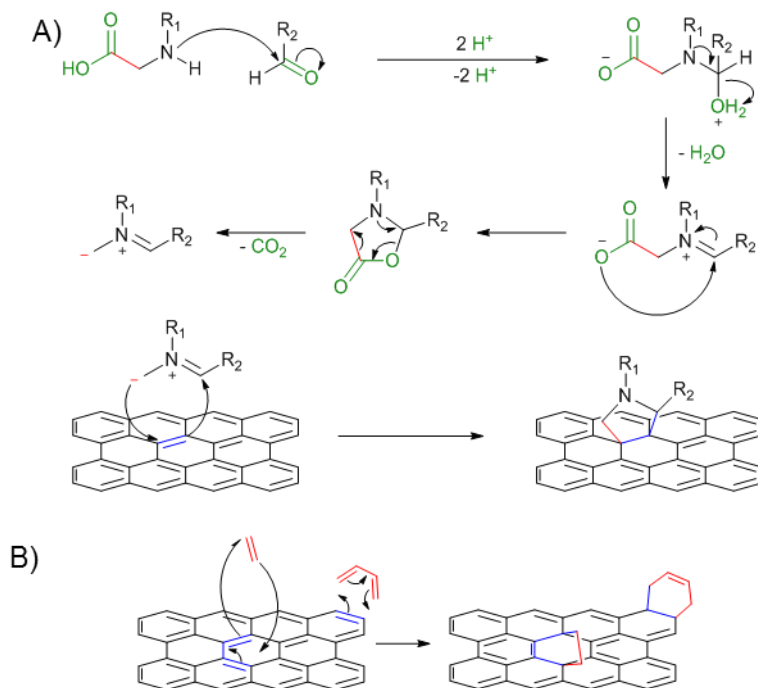
Figure 16: Schematic mechanisms of the reactions described in the text A) *in situ* **formation of ylide by reaction of aldehyde and *N*-substituted glycine under elimination of H₂O and CO₂. The ylide can react in a [3+2] cycloaddition with graphene. B) Diels Alder reaction between graphene and either a diene or a dienophile.**

2.4.2 Functionalization of Graphene Oxide

In contrast to pristine graphene, functionalization of GO is surprisingly approachable. The many available functional groups on the GO surface can serve as chemical handles to introduce new functionality. Reactions with both nucleophiles and electrophiles are possible to attach functionality. Nucleophiles are for functionalization onto basal plane by reaction with epoxides or onto the edges by reaction with carboxylic acids after appropriate activation, electrophiles for basal plane hydroxyls or for edge carboxylic acid. The challenge in functionalization of GO lies more in selectively controlling the functionalization, as there are several different types of functional groups in GO that can be used at GO functionalization sites.

GO edges are covered with carboxylic acids. These can be used for edge functionalization with nucleophiles through activated coupling reactions with reagents such as SOCl₂[179], 1-Ethyl-3-(3-dimethylaminopropyl)carbodiimide (EDC)[180], and *N,N'*-Dicyclohexyl-

carbodiimide (DCC)[181] (Figure 17). EDC coupling with amines is the most commonly used method.

The main complication of edge functionalization is restricting it to the edges, as "unwanted" functionalization of basal plane sites through nucleophilic ring opening of epoxides (below) is also possible.
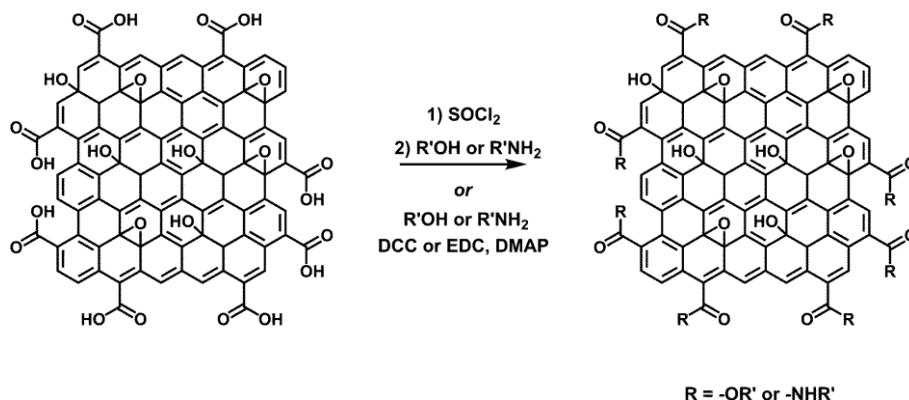
Figure 17: Schematic illustration of edge functionalization of carboxylic acid by activation followed by coupling with amine. (Reproduced from ref[182] with permission Copyright The Royal Society of Chemistry.)

Nucleophilic ring opening of epoxides can be used to effectively functionalize the basal plane of GO. Here the nucleophile attacks the α-carbon of the epoxide, opening the epoxide group into a hydroxyl at the β-carbon (Figure 18A)[183,184]. Use of isocyanates is an electrophilic approach to basal plane as well as edge functionalization (Figure 18B), as strong electrophilic isocyanates can react with either edge carboxylic acids to create carbamate esters or basal plane hydroxyl forming amides[185].
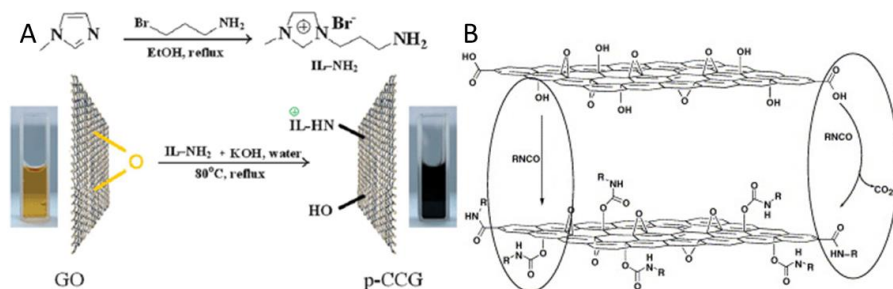
Figure 18. Illustration of basal plane functionalization A) by nucleophilic ring opening of epoxides and B) using isocyanate functionalization. (Reproduced A) from ref.[183] with permission Copyright The Royal Society of Chemistry 2009, and B) ref.[185] with permission Copyright Elsevier Ltd. 2006)

2.4.3   Functionalization of Reduced Graphene Oxide

The reduction of GO removes a large fraction of the reactive groups. However, as previously mentioned, complete reduction is not achieved. RGO can therefore be functionalized by much the same methods as GO, though much less effectively[186]. Chemical modification is therefore usually done before reduction of GO.

Post-reduction modification can also be done using the methods described for graphene modification, as the π-system is largely restored (section 2.4.1 page 17). As expected, the reaction is more effective on RGO than on pristine graphene due to the higher concentration of defects. Examples of using free radical chemistry through diazonium salt[187] or carbene chemistry[188] to functionalize RGO post-reduction have been reported.

2.5   Characterization of Graphene-Like Materials

As noted (section 2.3.1 page 14), full structural characterization of GO and of RGO or CMG is highly challenging if not impossible. However, some important features can be characterized in considerable detail, and such characterization is of paramount importance in the evaluation of these materials. The characterization can be divided into topological and chemical structure characterization.

2.5.1   Topological Characterization

Properties of graphene-like materials depend strongly on their sheet thickness and their surface area, which are the key parameters for their applications. Topological investigation of graphene materials, including particularly the thickness of sheets to determine if they are mono-layered or multi-layered, can be done using a range of different structural techniques: Raman spectroscopy, Brunauer–Emmett–Teller (BET) surface area determination, AFM and TEM.

Raman spectroscopy can be used to evaluate indirectly the thickness of graphene sheets by assessing the ratio between the D band (associated with disorder) and the G band (associated with the stacking). A high D/G ratio indicates low degree of stacking[141].

Microscopic imaging techniques are essential tools to provide information of shape, size and thickness in the characterization of all nano-materials, including graphene. Due to the very small thickness of graphene, only AFM[189] and TEM[190] provide appropriate high resolution. In this thesis, AFM has been the main method of choice.

Atomic Force Microscopy

AFM is a scanning probe technique where a tiny sharp probe (end radius of curvature < 10 nm) raster scan the surface in order to "feel" the surface and generate a topography map.
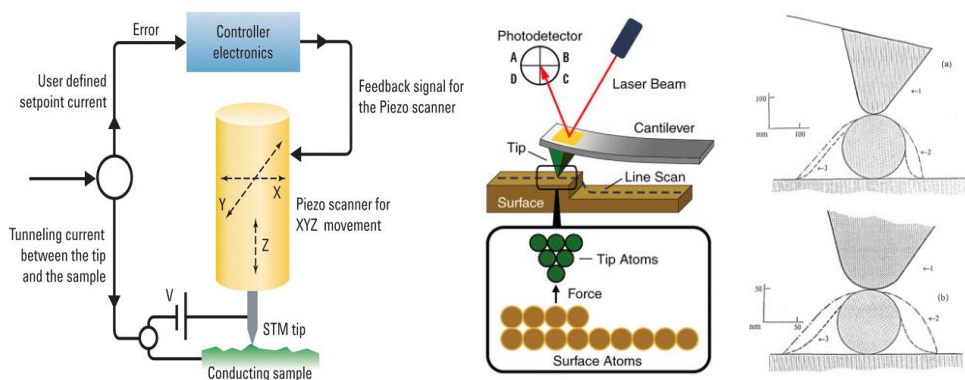
Figure 19: A) schematic of principal components of an SPM setup and how output signal is maintained through a calibrated feedback controller. B) Illustration of how the laser beam is reflected by the cantilever in AFM and photodetector. C) Illustration of convolution of a spherical object scanned by a tip. The dashed line represents the recorded data. (A and B Reproduced from Agilent SPM 5500 user manual and C from ref.[191])

AFM relies upon the precision of a piezo electric controller to control the XYZ-position of the probing tip at the end of a cantilever mounted on the piezo.

In the contact mode, a laser beam is deflected off the bent cantilever. When a change in force is exerted on the probe, the cantilever bending changes because of change in topography and thereby the laser deflection. In the tapping mode, the cantilever is set to vibrate either through acoustic vibration or using a magnet. The amplitude of the vibration is reduced when the tip approaches the sample surface. A calibrated controller unit in a feedback loop controls the piezo Z-position as the XY position is scanned. Changes in output signal of either deflection in contact mode or amplitude in tapping mode vs set-point value, are translated into an electric signal to the piezo to change the Z-position in order to maintain contact deflection or amplitude (Figure 19A and B). AFM is an exceedingly sensitive technique with regard to Z-height able to detect sub nano-meter changes. However, the X and Y precision is distorted due to convolution of the surface and the tip (Figure 19C).

A strong advantage of AFM is that it can be used to investigate any solid material surface such as conductive, semi-conductive, non-conductive, magnetic, hard or soft materials, in a variety of environments such as specific atmospheres or liquids. Another key advantage is the possibility of combining AFM with other techniques such as electrochemical control, conductivity studies, infrared spectroscopy (IR) and others. All AFM measurements for this thesis were recorded using an Agilent SPM 5500 system in the contact mode together with Bruker DNP-S10 contact mode tips.

2.5.2   Chemical Structure Determination

Due to the complex nature of GO, RGO and CMG, structural investigations require a combination of multiple techniques to verify chemical modifications. The best methods are XPS, NMR spectroscopy, elemental analysis, and infrared (IR) and Raman spectroscopies. To some extent information from thermogravimetric analysis (TGA), X-ray diffraction (XRD) and ultraviolet-visible (UV-vis) spectroscopy can also be used, but only for specific systems.[192,193]

Probably the most powerful technique for structural determination in carbohydrate chemistry is liquid phase NMR spectroscopy. Unfortunately, due to slow rotation of the large graphene sheets, anisotropic coupling arises complicating the spectra. Instead, solid-state magic angle ^{13}C-NMR spectroscopy can be used. However, XPS is more often used in this field, which also provides chemical shifts of binding energy based on local chemical environment, as well as elemental composition based on elemental survey.[137,138,146,148,192] Further information on chemical functionality can be found through vibrational spectroscopy - either IR or Raman spectroscopy - based on their fundamental vibrations[192,193]. The primary techniques used in this thesis for structural determination is, first XPS acquired on DTU Danchip ThermoScientific K-alpha XPS instrument with K-Alpha X-ray source with photon energy of 1486.7 eV. This is secondly, complimented by IR spectroscopy in the form of Attenuated Total Reflection Fourier transform infrared spectroscopy (ATR-FTIR) acquired on Bruker ALPHA FTIR Spectrometer using ATR sampling module.

X-Ray Photoelectron Spectroscopy

XPS is a surface technique, and due to the flatness of graphene, XPS provides valuable information. In XPS a solid sample under high vacuum (10^{-10} bar) is irradiated with soft mono-chromatic X-rays in order to kick out electrons. The number of electrons and their energy generates the spectrum. These energies can be correlated to orbital energies and even the local chemical environment.

The carbon 1s (C1s) peak can be de-convoluted into the characteristic peaks at 284.4 eV (C–C sp^2), 285.2 eV (C–C sp^3), 286.4 eV (C–O), 287.7 eV (C=O) and 289.1 eV (COO$^-$)[192], respectively (Figure 20A&B). The deconvolution yields direct information on the reduction extent, in terms of not only reduced oxygen content, but also reformed sp^2 hybridization. The nitrogen 1s (N1s) peak can be deconvoluted to offer additional information on the chemical state, which in many cases is important to evaluate functionalization (Figure 20C&D).
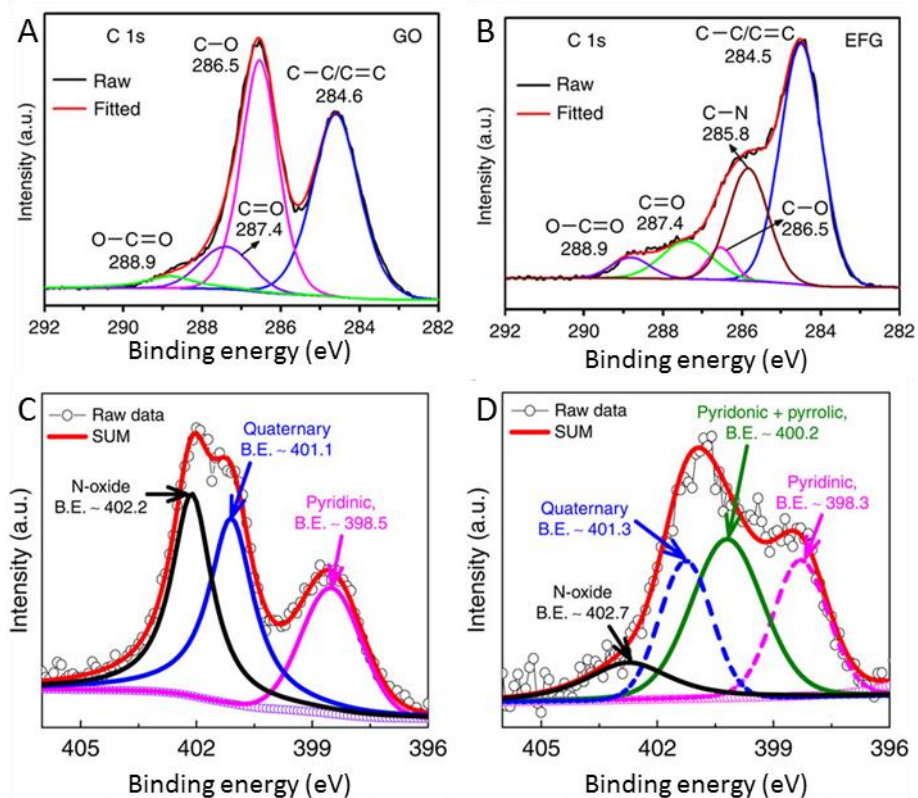
Figure 20. XPS characterization of carbon materials C1*s* XPS spectra of A) GO, (B) functionalized RGO. Deconvoluted N1*s* spectra for carbon nanofibers. C) before and D) after electrochemical treatment (A & B Reproduced from ref.[194] and C and D from ref.[195] with permission. Copyright Macmillan Publishers Limited. 2014 and 2013)

2.6   Graphene Sensors based on Supramolecular Functionalization

Electrochemical sensors based on RGO and CMG show great promise, due to good conductivity and high surface area, as well as electro-catalytic properties caused by residual functionalities or specifically attached functionalities. As with other electrochemical sensors, selectivity is achieved by the separation of voltammetric redox peaks. However, interference is a problem, but CMG with supramolecular functionalities can here provide an extra level of selectivity through host-guest recognition (section 1.3.1 page 6).

2.6.1   Ion-Selective Functionalized Graphene

Supramolecular ion receptor molecules have been used for ion selective sensing for decades. Their multiple directional interaction and size specific sites facilitate highly selective binding of specific ions. These receptors include crown-ethers[14] and Schiff base complexes[15].

Even though graphene-like materials have been used extensively to produce chemical and biological sensors, there are only few examples of utilizing the properties of both graphene and supramolecular moieties, and even fewer reports on covalent modification to introduce these moieties. Supramolecular ionophores are widely used in preparation of ion-selective membranes which are used in graphene based potentiometric sensors, but not directly on the graphene[196–200]. One example of direct use of a supramolecular receptor on graphene to produce a sensing material is the work of Y. Xu *et al.*[201] who synthesized an optical sensing material for Cd^{2+} by non-covalently attaching a porphyrin derivative through electrostatic and π-π interaction to a RGO nanosheet. The sensing material is able to selectively detect Cd^{2+} at 10^{-6} M concentration (Figure 21).
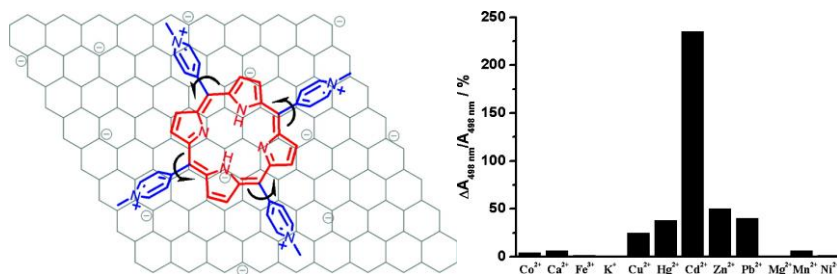
Figure 21: A) Illustration of optical sensing material with non-covalent modification of RGO with porphyrin derivative. B) substrate profile of absorption changes at 498 nm toward addition of 1.0 µM of different metal ions. (Reproduced from ref.[201] with permission. Copyright American Chemical Society 2009)

2.6.2   Cavitand Functionalized Graphene for Neutral Analytes

Supramolecular cavitands have been used for molecular recognition of neutral guests inside their binding pockets, often controlled primarily by hydrophobic forces, but also assisted by supramolecular interaction[16–18]. Cyclodextrins, calixarenes, pillararenes and cucurbiturils are most common. Cavitand modification of graphene for the purpose of making sensors has in fact been quite extensively reported. Most of these modified sensors utilize a non-covalent approach. Especially cyclodextrins are used, but calixarenes have also been reported. Selective sensors for biologically important analytes such as Pesticides[19,20], medicinal compounds[21–24] and carcinogens[25] based on cavitand functionalization of graphene-like materials have been reported.

Cyclodextrin functionalized graphene electrodes can for example be used in combination with differential pulse voltammetry (DPV) thus providing a two-dimensional sensing as shown by Chen and co-worker[202] (Figure 22). First, only molecules able to bind in the cyclodextrin hydrophobic site can approach the electrode. Second, the redox potential further separates the approaching molecules. This illustrates the essence of how cavitand functionalized graphene electrochemical sensors work. The sensor reported by Chen and co-worker[202] shows high selectivity for multiple compounds due to the two-dimensionality of this system with a detection limit for rhodamine B of 6.5 nmol L^{-1} and for 1-animopyrene 3.6 nmol L^{-1}.
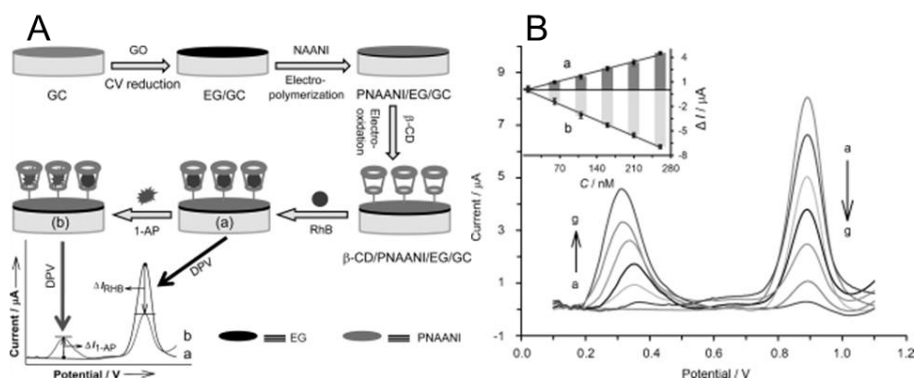
Figure 22. A) Illustration of dual-signalling electrochemical sensor based on the competitive host–guest interaction between cyclodextrin and substrates. B) DPV responses of the RhB bound to functionalized electrode. (Reproduced from ref.[202] with permission. Copyright Wiley-VCH Verlag GmbH & Co. KGaA, Weinheim 2013)

As shown by Yang *et al.*[203] cyclodextrin covalently attached to RGO can also be used to create such a dual selectivity system. Gold nanoparticles were further incorporated into their nanohybrid structure, where DPV was used to selectively detect p-nitrophenol and hydroquinone. The power of this method of combining selective binding and electrochemical selectivity was shown by Erhan Zor *et al.*[204] when they used a cyclodextrin modified RGO to separate the redox peaks of enantiomers of cystine in DPV, due to their different interaction with the cyclodextrin (Figure 23).
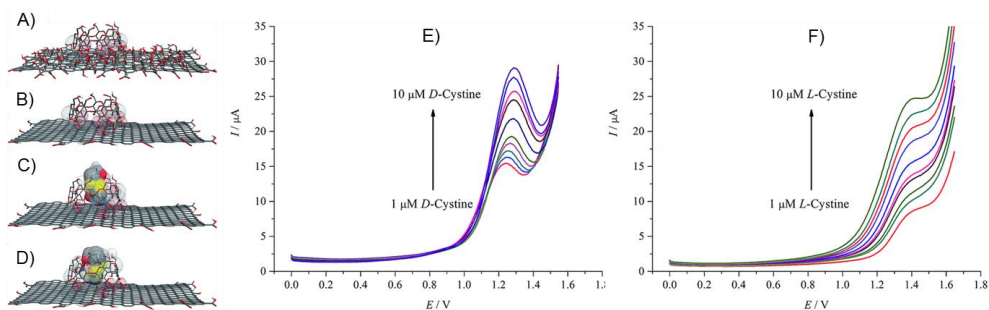
Figure 23. A-D) Computational model structures of β-CD in complexes with GO (A+B), RGO/β-CD complex (C) with D-cystine and (D) with L-cystine, showing the different binding in the cyclodextrin resulting in the difference in the DPV. E & F) Differential pulse voltammograms at increasing concentration of D-cystine (E) and L-cystine (F) in concentration range 1–10 µM. (Reproduced from ref.[204] with permission. Copyright the Royal Society of Chemistry 2015)

Mao *et al.*[205] similarly achieved enantiomeric selectivity by using a non-covalently immobilized calix[4]arene recognition unit on graphene. This system allowed enantiomeric selective sensing of amino substituted propanol at nmol L⁻¹ concentrations using electrochemical impedance spectroscopy (Figure 24).
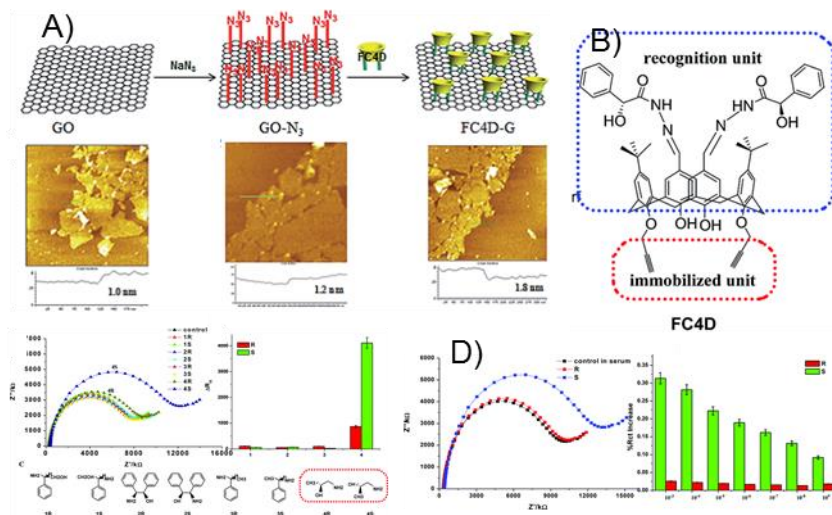
Figure 24. A) Schematic of the synthesis procedure for calix[4]arene derivative on graphene. B) molecular structure of the calix[4]arene recognition unit. C) Impedance response of four pairs of amino propanol analogues. D) sensing for the selective amino propanol analogue in serum with impedance spectra showing clear enantiomeric selectivity. (Reproduced from ref.[205] with permission Copyright The Royal Society of Chemistry 2015)

2.6.3   Fluorescence Sensing by Guest Exchange

Still another method of using supramolecular moieties in combination with graphene for sensing is to exploit the long-range ($\approx$ 30 nm) fluorescence quenching properties of graphene, and of RGO and CMG[206,207]. Sensors can thus be made through competitive guest exchange of a fluorophore and analyte by having a fluorescence probe interacting weakly with the supramolecular host. When the system is exposed to a stronger binding analyte guest exchange, as a result of competitive binding, the fluorophore is released and the fluorescents signal is turned on.

An example of such systems, used for *in vivo* observation of the biologically important metabolite L-carnitine, was reported by Li and co-workers[208] (Figure 21). This system is based on immobilized p-sulfonated calix[6]arene on CMG, loaded with the fluorescent dye safranine T bound through electrostatic interaction with p-sulfonated calix[6]arene. The fluorescence dye in the calix[6]arene will be quenched by the proximity to the graphene sheet. Competitive binding of L-carnitine liberates the fluorescence dye, resulting in turn-on of the fluorescent signal with a detection limit of 1.54 µmol L^{-1}. Furthermore, they showed selectively over structuslly similar molecules glutamate and O-acetyl-L-carnitine.
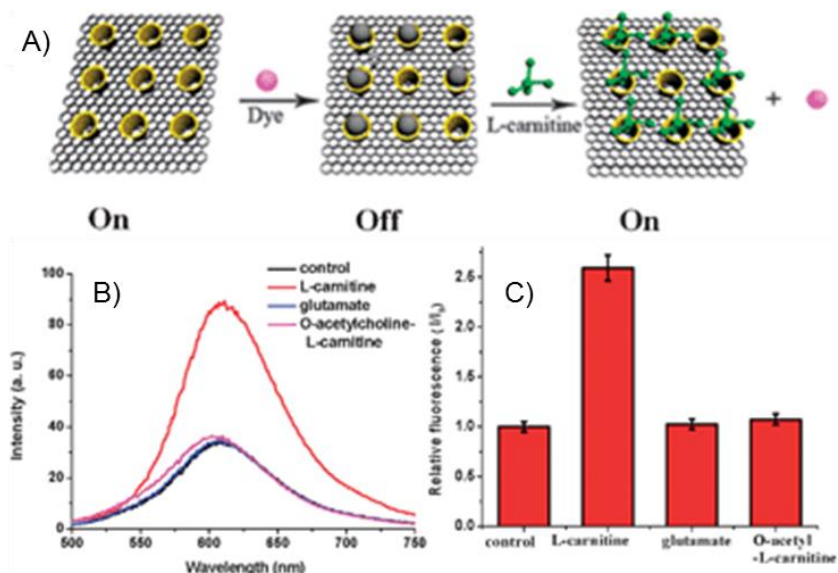
Figure 25. A) Schematic demonstration of the fluorescence "off–on" mechanism for detecting L-carnitine. B) Fluorescence spectra of CMG–hybrid (C) Relative fluorescence intensity (Reproduced from ref.[208] with permission. Copyright The Royal Society of Chemistry 2012)

2.7   Concluding Remarks and Outlook

The combination of electronic properties and high surface area of graphene makes it ideal as a transducer for sensors. RGO and CMG further benefit from significantly lower production cost and the possibility of up scaling compared to pristine graphene. Furthermore, unique possibilities of increasing selectivity of these systems arise from the residual functional groups and especially from introduced functionalization.

Especially the use of supramolecular moieties can introduce crucial selectivity to sensor systems, by selectively limiting access to the electrode surface or enforce binding of specific molecules, or even through competitive binding to release probe molecules on detection of target analytes. However, despite many impressive examples demonstrated in this area the full potential has not been explored. The use of more specific receptor systems and of covalent attachment could provide other exciting new sensors.

Chapter 3   Crown-Ether   Functionalized Reduced Graphene Oxide

This chapter describes the work conducted on RGO functionalized covalently with crown-ether. An introduction to ionic receptors, crown-ethers and their binding mode is first described. We then discuss how crown-ether functionalized RGO can be used for sensors and compare with previous work on graphene crown-ether composites, before going into design, synthesis and testing of RGO functionalized with 18-crown[6]ether. Part of this work has been published in ACS Applied Materials and Interfaces[209]. It is finally illustrated, how this work can be used with other crown-ethers particularly 12-crown[4]ether and 15-crown[5]ether.

3.1   Alkali Ion Sensing

Ions are one of the most important targets for selective solute quantification in solution. Some essential ions play a crucial role in the function of biological systems, while others, mainly heavy metals cause damage to the same biological systems. Detection of ions in solutions is therefore crucial for environmental monitoring, food-quality control, and clinical diagnostics[210,211]. Some of the most critical ions in clinical diagnostics include protons, sodium, potassium and calcium ions[4,5]. Environmental monitoring, especially of mercury, lead, arsenic, antimony and cadmium are core target ions, due to their toxic effects on humans and on biological systems in general[212,213]. Clinical measurement for diagnostics of those ions are performed in high-end laboratory setting. However, the need for more cost-efficient detection methods used in response to e.g. natural disasters, as well as in remote and resource-limited environments, are ever present[6–8].

High selectivity towards a single target ion is of paramount importance for sensors of physiological samples as practical samples, that contain many different types of ions. Furthermore, the more challenge comes that in many cases the target ion is the ion present in
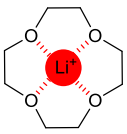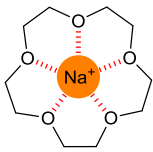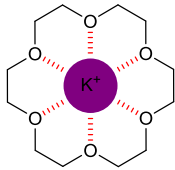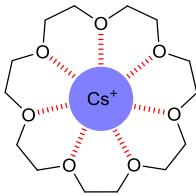
the lowest concentration. For instance, the potassium to sodium ratio in blood is approximately 1:30[214].

One of the key uses of supramolecular host systems is for chemical sensing, where directional interaction combined with size of the binding site are used to give high selectivity. For cations the most used systems are crown-ethers[14], calixarenes and Schiff base complexes[15]. These have been used extensively for sensors of different types to selectively bind and detect cations[215–217].

Crown-ethers are one of the oldest families of supramolecular hosts. The first crown-ethers were studied by Charles Pedersen in 1967[218,219]. Crown-ethers are highly selective for alkali ions, and the selectivity depending on the size of the crown-ether ring, different alkali ions are bound selectively. When binding alkali ions, the crown-ether oxygens form ion-dipole interaction with the positively charged ion resulting in large binding constants of the complexes (Table 3).

Table 3: Illustration of different size crown-ethers binding different alkali metals. Cavity diameter (Ø), and selective ion diameter are given. The binding constants, log K were measured in methanol at 20 °C for each of the crown-ethers[220].

	12-Crown[4]ether	15-crown[5]ether	18-crown[6]ether	21-crown[7]ether
Cavity Ø[220]	1.2 – 1.5 Å	1.7 – 2.2 Å	2.6 – 3.2 Å	3.4 – 4.3 Å
Ion Ø[220]	Li^+ = 1.20 Å	Na^+ = 1.90 Å	K^+ = 2.66 Å	Cs^+ = 3.34 Å
Log K	Li^+ = 1.7	Na^+ = 3.24	K^+ = 6.08	Cs^+ = 5.02

Combining the conductive properties of graphene-like materials with enzymes has proven another highly successful way to generate selective biosensors[221]. Likewise, using supramolecular hosts such as crown-ethers should also provide possible highly selective sensing materials. Despite all the reports on graphene materials in the field of sensors over the last decade, there are, however, surprisingly few reports where supramolecular hosts have been used.

The majority of these reports focus on cyclodextrins (section 2.6.2 page 26). Many possibilities are open within this field. However, ionophores are extensively used for graphene based potentiometric sensors but using these in ion-selective membranes not as part of the graphene materials[196–200].

3.2   RGO-Crown[6] for Potassium Ion Sensing

This system is to bind potassium ions selectively to the surface of RGO using a modified 18-crown[6]ether covalently attached to the basal plane of RGO via a short linker, with the aim of developing potassium ion selective sensing material.

3.2.1   Related RGO – Crown-Ether Systems

Apparently the only example of using crown-ethers functionalized graphene to produce selective sensing material for potassium ion was reported by X. Qu and co-workers[222]. In this report 18-crown[6]ether and RGO mixing to form a hybrid structure held together by hydrophobic interaction between RGO and a methylenes in 18-crown[6]ether was described. An aminated fluorescent carbon dot (CD) probe was anchored to the crown-ether. The proximity of CDs to the graphene structure results in quenching of the fluorescence. Upon exposure to K$^+$, CDs are released due to competitive replacement of crown-ether guest resulting in turn-on of CD fluorescence signal (Figure 26). This system has a detection range of 0.05 – 10.0 mM. Two other related examples where smaller crown-ethers have been covalently attached to graphene-like materials are also reported. R. Ballesteros-Garrido *et.al.*[223] reported the use of covalently attached 9-aza-crown[3]ether to graphene effectively binding alkali-metal ions (Li$^+$, Na$^+$ and K$^+$) in order to increase the lifetime of charge separated photo-induced excited electronic states of graphene by ionic stabilization. M Banerjee *et al.*[224] later used 1-aza-15crown[5]ether to improve the binding of Li$^+$ to graphene with application for solid electrolytes in lithium ion batteries.
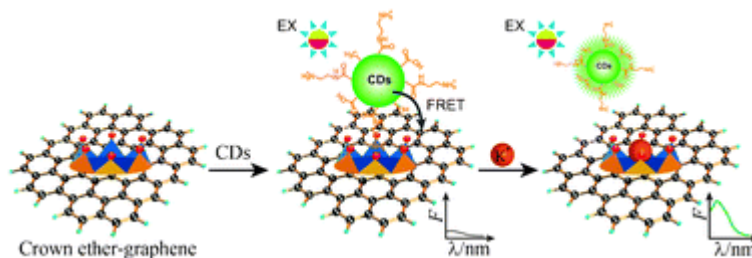
Figure 26: Schematic illustration of the Förster resonance energy transfer (FRET) model based on CDs–graphene and the mechanism of K$^+$ determination. (Reproduced with permission from ref.[222]. Copyright 2012 the Royal Society of Chemstry)

3.2.2   System Design

A recent theoretical density functional theory (DFT) study by K. Cho and co-workers[225] showed that 12-crown[4]ether suitable to form crown-ether–Li$^+$ complex can adsorb onto the basal plane of graphene surfaces through weak interaction (Figure 27B). In the system we present here, we follow the strategy of covalently attaching 18-crown[6]ether to achieve

similar adsorption, by inserting a short flexible linker between the crown-ether and the graphene sheet to minimize potential strain in the system (Figure 27A).
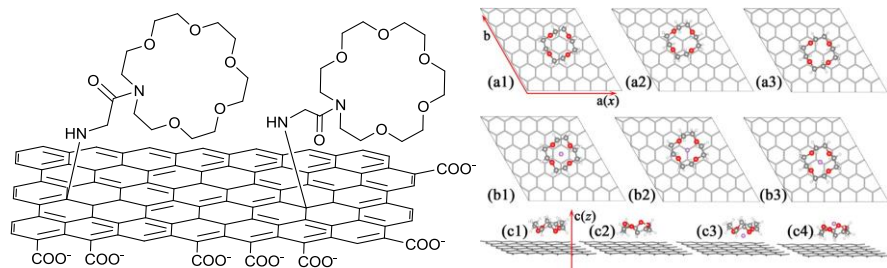
Figure 27: A) Illustration of system design (Reproduced with rights from ref.[209]. Copyright 2015 American Chemical Sociaty). B) Different configurations for crown-ether on single-layer graphene and of CE(O)/graphene, CE(H)/graphene, CE/Li(or Li+)/graphene, and Li(or Li+)/CE/graphene. (Reproduced with permission from ref.[225]. Copyright 2015 American Chemical Sociaty)

Basal plane functionalization on GO and to some degree on RGO can be achieved, by either nucleophilic addition through nucleophilic ring opening of basal plane epoxide functional groups, or electrophilic addition though isocyanides (section 2.4.2 page 20). As isocyanides are unstable towards H_2O and the graphite oxidation is done in H_2O, we chose the nucleophilic approach. The linker must have a terminal amine group for reaction with epoxides in GO/RGO.

In order to covalently attach 18-crown[6]ether, the crown-ether has to be modified with an anchoring group. This is normally done by replacing one oxygen atom with a nitrogen atom[226]. As oxygens are directly involved in binding of the potassium ion, this substitution weakens the binding, since nitrogen is a weaker Lewis base than oxygen, reducing the ion-dipole interaction[226]. Furthermore, amines are also Brønsted bases introducing a pH dependence. Instead of an amine link, we used an amide. This further reduces the sixth ion-dipole interaction, as the nitrogen lone pair is now partially involved in the amide bond. Thus, the problematic pH dependence in the binding mode is removed. Being a short flexible linker, with both terminal amine and terminal carboxylic acid for attachment to GO/RGO and crown-ether, respectively, glycine as the linker perfectly fits these requirements, (Scheme 1).
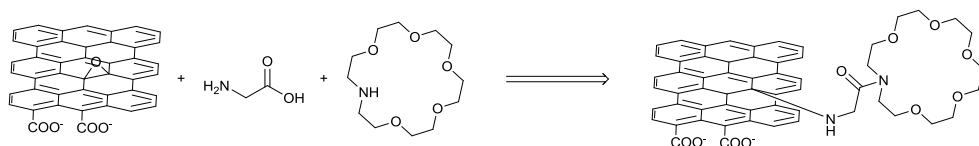
Scheme 1: Schematic illustration of retrosynthetic deconstruction of graphene functionalized with 18-crown[6]ether.

3.2.3 Synthesis

The modified crown-ether with attached linker was synthesized, starting from commercially available 1-aza-18-crown[6]ether and *N*-(tert-Butoxycarbonyl)glycine. These compounds were coupled together using a triphosgene activated protein coupling procedure modified from[227] (experimental in 7.1.2 page 106). This was followed by deprotection of the boc-group using trifluoroacetic acid[228] (experimental in 0 page 106). The crown-ether with the linker was then ready for functionalization of the GO/RGO (Scheme 2).
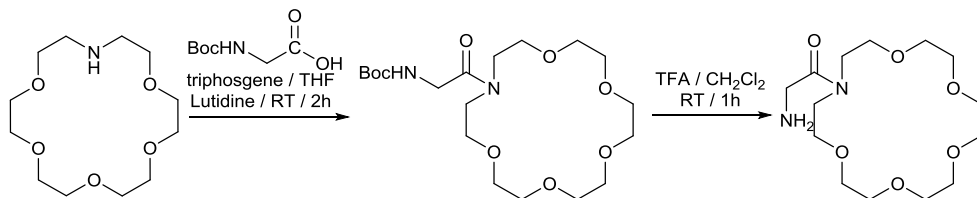
Scheme 2: Schematic of the synthesis route to linker modified crown-ether.

GO was synthesized by a modified Hummers' method[135,229] (experimental section 7.1.1 page 104). GO was oxidized in two steps; first with $K_2S_2O_8$ and P_2O_5 and then by $KMnO_4$. The prepared GO was then treated with an acidic aqueous workup, and neutralized by extensive washing and centrifugation, before final size separation with centrifugation. The result is fully dispersed monolayer GO sheets with approximate XY dimensions of 1–8 µm.
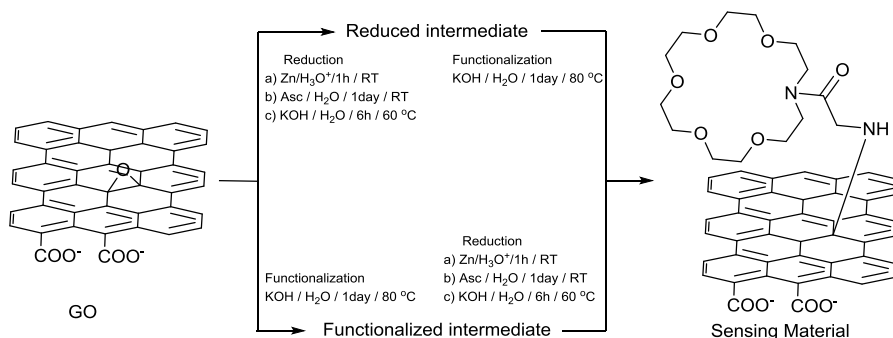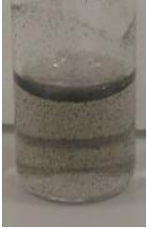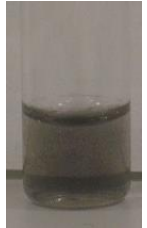
Scheme 3: Synthesis routes from GO to sensing material by reduction and functionalization, in either order.

Due to the risk of amide substitution, hydrazine was not considered viable for reduction of functionalized GO. Instead, three different milder GO reduction methods were used: Zn/H_3O^+ (experimental in 7.1.6 page 109)[155]; ascorbic acid[153] (experimental in section 7.1.7 page 109) and strong alkali solution[157] (experimental in section 7.1.5 page 109). It was attempted to functionalize and reduce GO in either order, for the reduction each of these three methods was used for separate batches (Scheme 3); to produce crown-ether functionalized RGO. In the case of Zn/H_3O^+ reduction, rapid aggregation occurred making functionalization after

reduction futile. Reduced RGO reference samples were taken from the reduced first approach before further functionalization. All the GO functionalization experiments were performed with a 1 mg/mL GO concentration. All the materials were subsequently purified by dialysis $(28 \times 1 \text{ L})$ over 7 days.

Table 4: Synthesized materials and accompanying abbreviation; where FRGO means reduced then functionalized i.e. functionalized Reduced Graphene Oxide; RFGO means functionalized first then reduced e.i. Reduced Functionalized Graphene Oxide. The prefix letter specifies the reduction method used: A- for ascorbic acid, Zn- for Zn/H$_3$O$^+$ and B- for Alkaline reduction.

	Ascorbic acid Reduction	Zn/H3O$^+$ Reduction	Alkaline Reduction	No Reduction
Functionalization First				
Abbreviation	A-RFGO	Zn-RFGO	B-RFGO RGO-crown[6]	FGO
Reduction First		NA		NA
Abbreviation	A-FRGO		B-FRGO	
No Functionalization				
Abbreviation	A-RGO	Zn-RGO	B-RGO	GO

After the synthesis of the functional material reduced by either Zn/H$_3$O$^+$ or ascorbic acid visual aggregation was noted to have occurred, whereas the materials prepared by the alkaline solution reduction remained stable in solution (over one and a half years) (Table 4).

3.2.4 Preliminary Potentiometric Functional Tests

The equilibrium electrochemical potential of an electrochemical system originates from the *potential determining equilibria* in which components of the solution interact with the material of the electrode at the electrode/solution interfaces.

If we consider the potential determining equilibria for the designed system, which is a concentration gradient between the bulk solution and the electrode created by the increased affinity of the crown-ether, the potential ϕ can then be described by the Nernst equation (Equation 1) in the form:

Equation 1
$$\phi = \phi_{ref} + \frac{RT}{zF} \ln\left(\frac{aK^+_{electrode}}{aK^+_{bulk}}\right)$$

Where ϕ is the potential, ϕ_{ref} the potential in the absence of the probe ion, z number of electrons, F the Faraday constant, R the gas constant, and T the temperature.

It is important to consider activity instead of apparent concentration, as ionic solutions are non-ideal. The Debye-Hückel limiting law (Equation 2) is used to determine the activity coefficient (γ) in this thesis.

Equation 2
$$\log(\gamma) = -Az^2\sqrt{I}$$

Where A is a temperature and solvent dependent prefactor; for water at room temperature $A \approx 0.5$. I is the ionic strength given by (Equation 3):

Equation 3
$$I = \frac{1}{2}\sum_i c_i z_i$$

Where c_i is the concentration of each different ion, and z_i is their respective charge.

The main problem in potentiometric sensing, is that contributions from the entire solution species could contribute to the signal, making it inherently non-selective. The most common way to solve this problem is by using an ion selective membrane (ISM), through which only a specific ion can travel, thus making it possible to consider only contribution of the specific ions to the potential.

In our system, the electrode surface is regarded as selective for a specific ion, but that does not eliminate contributions from other ions. To ensure selectivity we will therefore use a high concentration of "background" electrolyte. As the contribution of all potential determining equilibria is additive the contribution from the electrolyte will dominate fixing the potential as long as electrolyte concentration is significantly higher than the other ion concentrations. Even though there is a large excess of Na^+ in the bulk solution K^+ will, however, be able to compete with Na^+ at the electrode interface thus given a substantial contribution to the potential, because of the electrode surface having a high affinity for K^+.

The functional materials were first tested a screen-like way, to assess which of the materials performed best for further analysis. The materials (10 µL of 1 mg/mL) were drop cast onto

polished 7 mm^2 glassy-carbon electrodes (GCE) and allowed to air dry overnight creating the functionalized electrodes. These were used for potentiometric titration of KNO$_3$ in the range 10^{-6} – 0.1 M in the presence of 0.1 M NaNO$_3$, testing if the electrode could bind potassium in the presence of excess NaNO$_3$ and produce a reproducible potentiometric response.
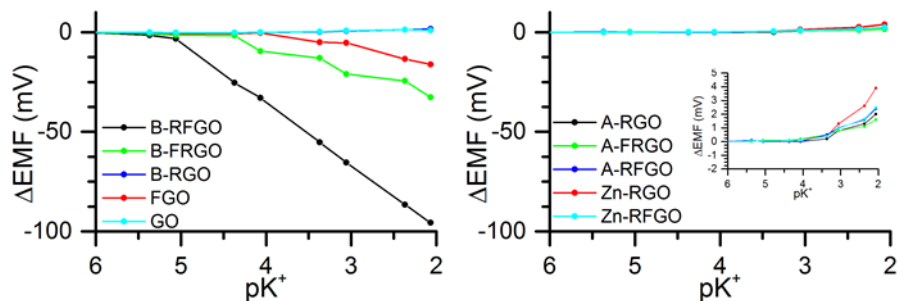
Figure 28: Preliminary potentiometric test of the 10 synthesised materials, by titration of KNO$_3$ in NaNO$_3$ 100 mM electrolyte.

As seen from the potentiometric titrations (Figure 28), the alkaline-reduced and then functionalized RGO and the functionalized GO show some response, whereas the material first functionalized and then alkaline-reduced RGO shows significantly higher response. All others show little to no response.

Based on the results of these preliminary potentiometric tests only B-RFGO henceforth abbreviated RGO-crown[6] was chosen for further functional test and full characterization. It was decided, however, to record XPS on B-FRGO and FGO as well, in order to possibly determine the reason behind the difference in functioning.

The ascorbic acid and Zn/H$_3$O$^+$ reduced materials were from now on omitted completely due to their highly aggregated state and no significant response to K$^+$.

3.2.5   Characterization

AFM Imaging

AFM imaging was used to determine whether RGO-crown[6] remained dispersed as monolayers or aggregation had occurred during functionalization or reduction of the material (Figure 29).

The RGO-crown[6] nanosheets were found to have lateral XY dimensions of 1 – 4 µm which is a slight reduction in sizes compared to the GO used (1 – 8 µm). The height was measured from about 1.2 – 1.3 nm and up to about 2.0 nm which again is higher than the GO (0.8 nm). This increase is presumably due to basal plane functionalization, although aggregation into double-layer graphene cannot be ruled out completely.
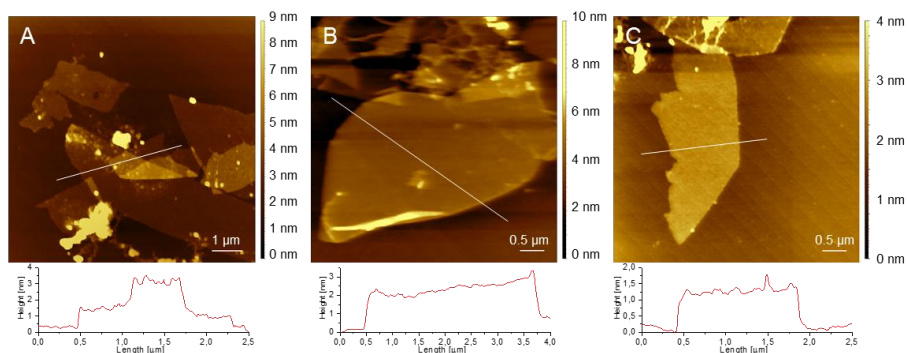
Figure 29: AFM images of RGO-crown[6] drop cast on mica showing single-layer sheets of 1 – 4 µm XY-size range. Topography of three separate images with height profiles A) 5×5 µm^2 B) 5×5 µm^2 C) 5×5 µm^2.

The reference B-RGO was also characterized by AFM. The lateral X-Y dimensions of 1 – 5 µm of these nanosheets (Figure 30) were similar to those of RGO-crown[6] leading to the assumption that fracturing of GO sheets occurred during the reduction in hot alkaline solution. The height of the B-RGO nanosheets are between 1.2 – 2.0 nm despite RGO normally being slightly thinner than GO. The increased height indicates re-stacking of the exfoliated GO into few-layer RGO.
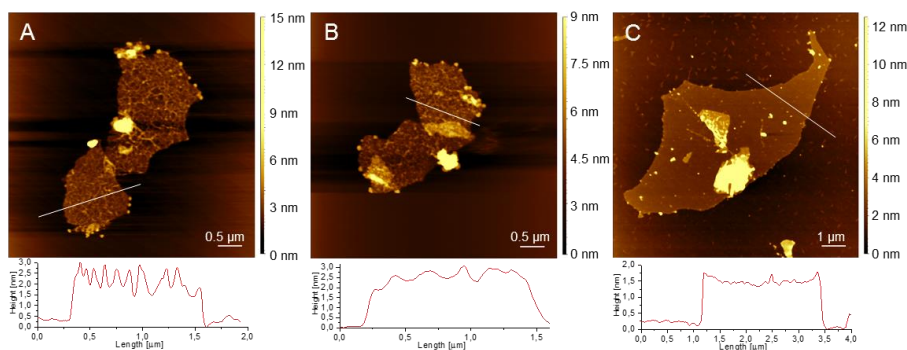
Figure 30: AFM images of B-RGO drop cast on mica showing single-layer sheet of XY-size range of 1 – 4 µm. Topography of three separate images with height profiles A) 5×5 µm^2 B) 5×5 µm^2 C) 10×10 µm^2.

IR Spectroscopy

Vibrational spectroscopy in the form of attenuated total reflection Fourier transform infrared spectroscopy (ATR-FTIR) was used to characterize RGO-crown[6] (Figure 31A) in comparison to B-RGO (Figure 31B). In attempts to verify that the crown-ether was attached to the RGO, the problem is that the characteristic fundamental vibration in the crown-ether overlaps with the fundamental vibration from residual functionalities in RGO in the

39

$1500 - 750 \text{ cm}^{-1}$ region. B-RGO and RGO-crown[6] both have a broad O–H stretching band at $3600 - 2600 \text{ cm}^{-1}$ which can be assigned to either edge COOH or as residual H_2O. Both exhibit peaks slightly lower than 3000 cm^{-1} consistent with sp^3 C–H stretch. In the case of B-RGO this is surprising, and hampers verification of functionalization, as the appearance of bands here would be consistent with ether functionalities. Again both materials have C=O stretch bands $\approx$ 1715 cm^{-1} as well as a range of peaks in the $1500 - 750 \text{ cm}^{-1}$ region which can be assigned to –CH_2– bending ($\approx 1465 \text{ cm}^{-1}$); C–O stretch ($\approx 1300$ & $\approx 1100 \text{ cm}^{-1}$); sp^2 C–H out of plane bending ($1000 - 700 \text{ cm}^{-1}$); and possibly oxirane rings ($\approx$ 800 cm^{-1}). When comparing the peak intensity of the $1500 - 750 \text{ cm}^{-1}$ region to the rest of the peaks, a definite increase is seen for RGO-crown[6] compared to reference BRGO.
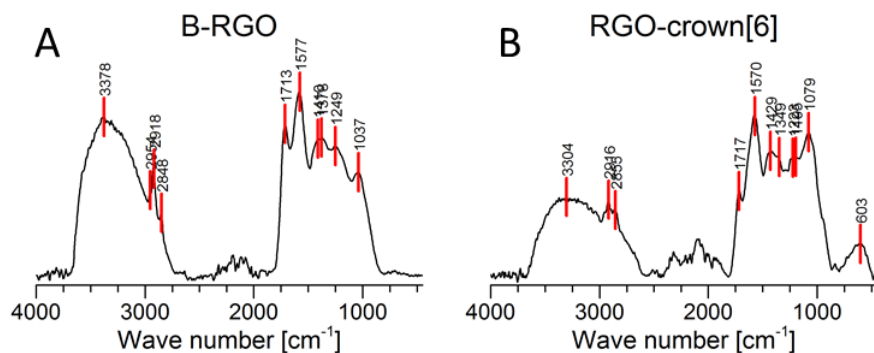
Figure 31: ATR-FTIR spectra of A) RGO-crown[6] and B) B-RGO.

A difference spectrum between B-RGO and RGO-crown[6] in the $1500 - 750 \text{ cm}^{-1}$ region could be recorded and compared to the spectrum of 1-aza-18-crown[6]ether (Figure 32). The major peak C–O–C stretch of the crown-ether at 1100 cm^{-1} clearly emerges, as well as to a lesser extent, several smaller peaks at 1500 cm^{-1}, 1300 cm^{-1}, 1250 cm^{-1}, 900 cm^{-1}, 800 cm^{-1}. The latter can be assigned to a combination –CH_2– bending, C–O stretch, sp^2 C–H out of plane bending, and possibly oxirane rings.
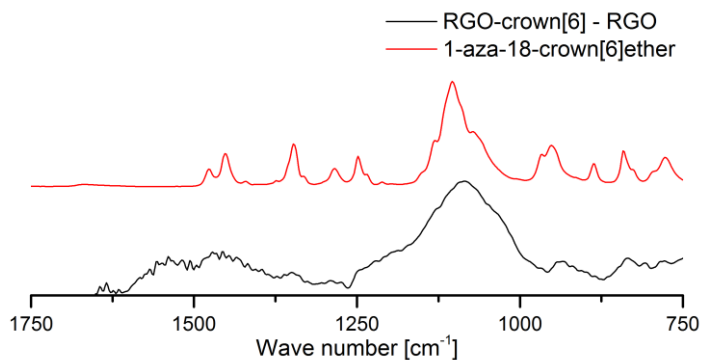
Figure 32: ATR-FTIR spectrum of 1-aza-18-crown[6]ether in red and difference spectrum between RGO-crown[6] and B-RGO in black, zoomed in the 1500 – 750 cm^{-1} region.

XPS Characterization

XPS-survey (Figure 33) was used to determine how much crown[6]ether was attached to RGO through changes in atomic composition (Figure 33 & Table 5). Under the assumption that the change in nitrogen content between B-RGO and RGO-crown[6] (2.5 %) is a result of attachment of the crown-ether moiety ($C_{14}O_7N_2$), the amount of crown-ether is equal to half this change (1.25 %). Similarly the crown-ether content of the B-FRGO is found to be significantly lower (0.6%), which explains the lower activity of B-FRGO determined by the preliminary potentiometric tests (section 3.2.4 page 37).

Table 5: Elemental composition as determined by XPS, as well as calculated contribution from crown-ether moiety and RGO sheet.

Sample	Raw data			Crown-ether ($C_{14}O_7N_2$)			Sheet Contribution		
	%C	%O	%N	%C	%O	%N	%C	%O	C:O
GO	68.8	30.2	1.0	-	-	-	68.8	30.2	2.3
B-RGO	75.8	23.8	0.9	-	-	-	75.8	23.8	3.1
RGO-crown[6]	75.1	21.5	3.4	17.5	8.75	2.5	57.6	12.75	4.5
B-FRGO	72.4	24.5	2.1	8.4	4.2	1.2	64.0	20.3	3.1
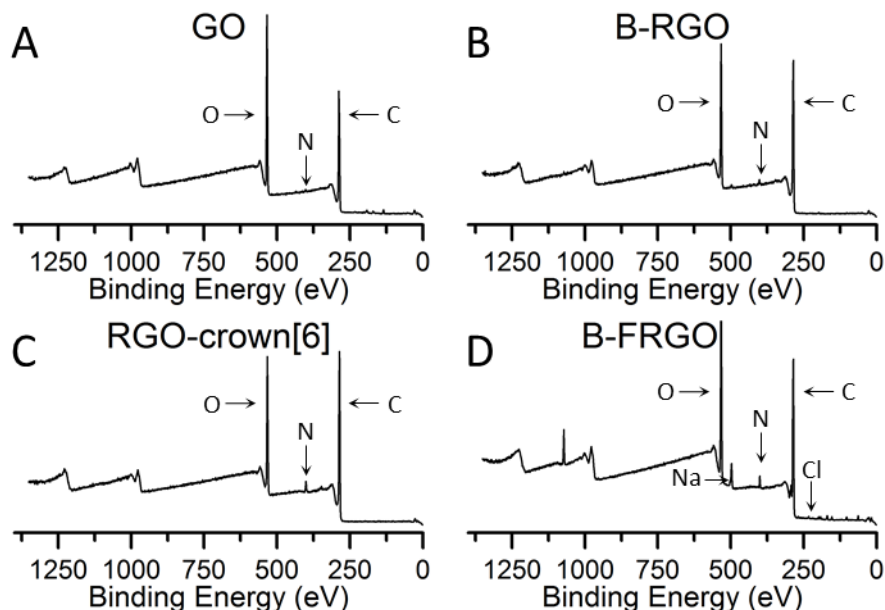
Figure 33: XPS – Survey of A) GO; B) B-RGO; C) RGO-crown[6] D) B-FRGO. C1s N1s and O1s peaks are indicated. In D) B-FRGO contains a NaCl impurity.

The carbon and oxygen from the RGO-sheet can be determined when the crown-ether content in the material is known, by subtracting the contribution from crown-ether from the total. It was found that there are 46 carbon atoms per 1 crown-ether moiety in RGO-crown[6] after separating the contribution from nanosheet and crown-ether functionality. Under the assumption that crown-ether is lying as "doughnuts" on the RGO nanosheet as predicted in the theoretical study by K. Cho and co-workers[225], the theoretical coverage can be estimated by comparing the surface area of graphene carbons and surface area of the crown-ether.

The surface area of a single graphene carbon has been calculated by A. Peigney and associates[101] to be 5.246 Å^2. Using the average distance between diagonal hydrogens in the 18-crown[6]ether crystal structure[230] as the diameter (10.2 Å) and assuming perfect circular shape, the surface area of the crown-ether is then 81.7 Å^2 making the surface coverage $\approx 34\%$. The less efficient B-FRGO contains one crown-ether per 107 carbon given a theoretical coverage of $\approx 15\%$.

The C:O ratio relevant to the reduction can then be calculated. Only a very mild reduction by the alkaline solution is observed, increasing the C:O ratio from 2.3 in GO to just 3.1 in the reference RGO as well as in B-FRGO which was reduced before functionalization. Surprisingly the RGO-crown[6] material seems to be reduced more intensively, giving a C:O ratio of 4.5. Furthermore, looking at the C1s spectra (Figure 34), GO contains a majority of oxygen bound carbon (C–O), whereas all reduced materials show a decrease of the C–O peak,

and an increase of the C–C peak. The latter is also slightly shifted towards lower binding energy, consistent with a partial change from sp^3 (284.8 eV) to sp^2 (280 eV) carbon.
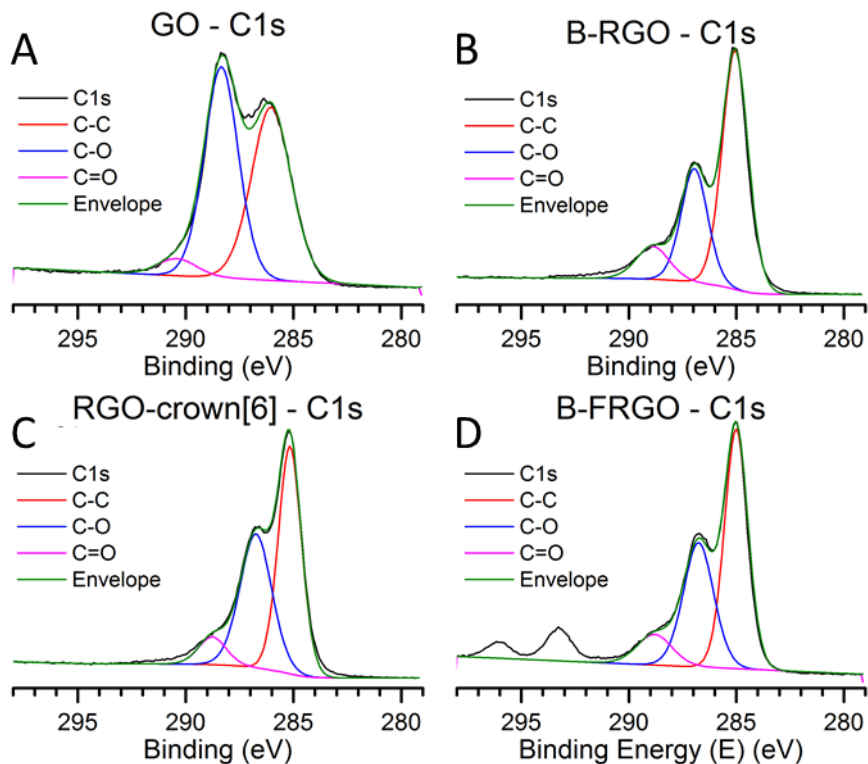
Figure 34: XPS C1s spectra of the materials A) GO; B) B-RGO; C) RGO-crown[6]; D) B-FRGO. Raw data (black); deconvoluted into C–C (red), C–O (blue) and C=O (purple) peaks. Enveloped sum of deconvoluted peaks (green) shows the fit to data.

3.2.6   Functionalized Glassy Carbon Electrodes

The RGO-crown[6] material was used to functionalize GCE, by drop casting of 15 µL of 1mg/mL aqueous dispersion onto polished 7 mm^2 GCE surface. After drying overnight, these were used as electrodes for sensitivity and selectivity studies. In these studies 100 mM NaNO$_3$ was used as a masking salt to stabilize the electromotive force and to remove contributions from salts with non-specific binding.

The sensitivity studies were performed on RGO-crown[6] functionalized GCE, as well as three reference electrode systems: clean GCE, reference RGO functionalized GCE and GO functionalized GCE. Potentiometric titration was performed in the range 10^{-7} to 10^{-1} M KNO$_3$. All three reference materials show little or no response below 25 mM where the concentration approaches the NaNO$_3$ concentration (Figure 35A). The RGO-crown[6], however, starts showing a response at 10^{-5} M and shows a linear potential increase of −37 mV

per decade up to 10^{-1} M. This negative potential change can be explained as the concentration at the electrode is high due to binding to the crown-ether even at low concentration, upon addition of additional K^+, the ratio between electrode and bulk concentration of K^+ is reduced, reducing the potential, the reason for non-Nernstian response is most likely from the masking $NaNO_3$ salt.
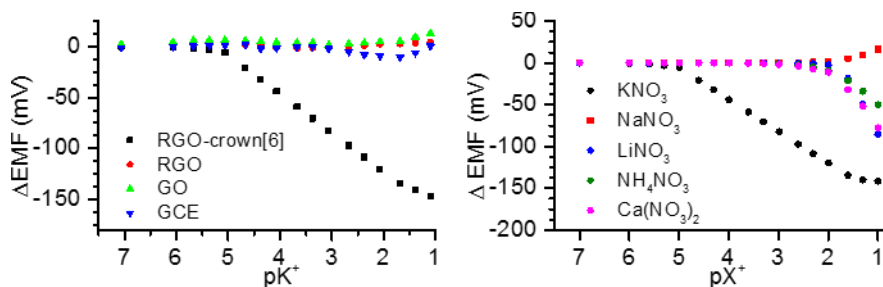
Figure 35: (A) Sensitivity tests: potentiometric KNO_3 titration, of GCE doped with RGO-crown[6] and of the reference materials GO, RGO, and pure GCE. (B) Selectivity tests: Potentiometric titration, of GCE doped with RGO-crown[6] with different salts (KNO_3, $NaNO_3$, $LiNO_3$, and $Ca(NO_3)_2$). All tested solutions contained 100 mM $NaNO_3$.

To determine the selectivity of the system, titration experiments of RGO-crown[6] functionalized GCE in electrolyte solution with masking salt $NaNO_3$, with a range of different nitrate-salts: Li^+, Na^+, NH_4^+ and Ca^{2+} were carried out (Figure 35B). None of these show any response within the linear range of the sensing signals. Response to all of the ions appears but only at concentrations approaching the $NaNO_3$ concentration.

3.2.7   Disposable Functionalized Screen-Printed Electrodes

In order to test this sensing material as simple and cost effective sensors of K^+, the sensing material RGO-crown[6] was used to modify DropSense 150 screen-printed electrodes by drop casting 15 µL of 1 mg/mL aqueous dispersion and drying overnight (Figure 36). The DropSense 150 electrodes consist of 4 mm diameter carbon working, Pt counter and Ag reference electrodes.

Figure 36: photography of modified DropSense 150 screen-printed electrodes.

When testing samples the potential of a zero-point reference in the form of 50 µL 0.1 M $NaNO_3$ was first measured. To 1 mL of real sample was then added 8.5 mg $NaNO_3$ masking salt equivalent to 100 mM. From this sample, 50 µL was then probed and correlated to the

calibration curve from GCE measurements. In total, 24 samples were prepared to evaluate these disposable sensors across the detection range; eight only containing KNO_3, eight "polluted" with $\approx$ 5 mM $Ca(NO_3)_2$ and eight "polluted" with $\approx$ 10 mM NH_4NO_3. All these 24 tested samples give responses fitting the GCE calibration very well. (Figure 37)
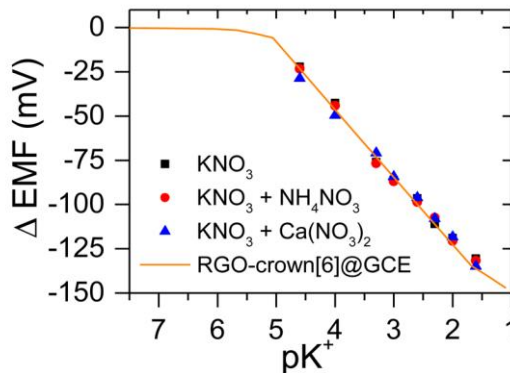
Figure 37: Potentiometric responses of the samples with varying KNO_3 concentrations in either pure solution or in the presence of NH_4NO_3 or $Ca(NO_3)_2$ all with added $NaNO_3$ equivalent to 100 mM, comparison to the GCE calibration curve also shown (solid line). Open circuit potential (OCP) was calibrated against 100 mM $NaNO_3$ solution.

3.2.8   Resistance based Sensing

The use of the sensing material RGO-crown[6] for a resistance type sensing device was explored during my external research stay at CIAC in Changchun, China. The idea behind this is that the film resistance of the RGO-crown[6] film would be reduced when exposed to K^+, because K^+ would be attached to the film surface due to specific binding. There are two electric pathways between the two electrodes in this system (Figure 38), either through electrolyte or through the thin film. The electrolyte pathway makes it problematic to use high concentration of masking salt, as this would reduce the electrolyte resistance and lower the sensitivity of the system. An ion-selective membrane (ISM) should therefore, be used in the final device. However, for initial investigation an ISM would introduce an extra element of selectivity and make it difficult to evaluate the selectivity provided by the material itself.
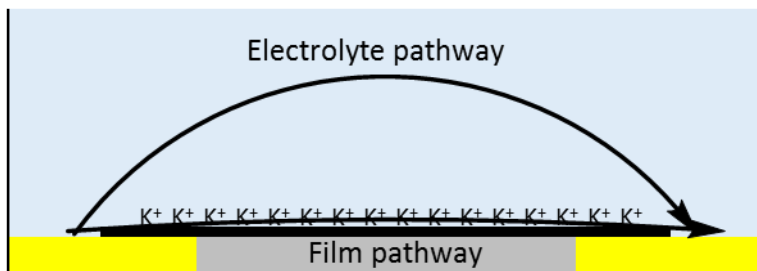
Figure 38: Illustration of principal electrical pathways in the source-drain system, for probing the sensitivity of the RGO-crown[6] to K⁺.

In order to test this principle, a simple source-drain like device was manufactured by sputtering gold onto a glass plate, with an intermediate layer of chromium acting as glue between glass and gold, creating two gold electrodes separated by 2 mm. These electrodes were then connected by a drop cast film of the sensing material RGO-crown[6] or reference material (experimental section 7.2.3 page 114; Figure 39A). A water reservoir with a Ag/AgCl reference electrode was placed on top of the RGO-crown[6] film and the two gold electrodes (Figure 39B&C) for electrochemical tests.
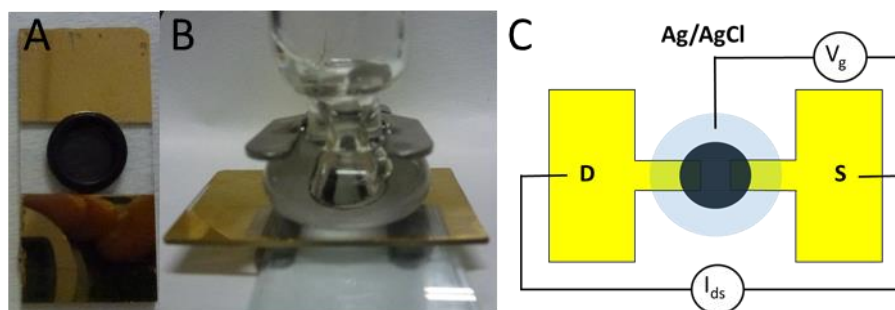
Figure 39: A) Photography of manufactured source-drain like device with drop cast RGO-crown[6] film (black spot). B) Photography of electrochemical setup with water reservoir. C) Schematic illustration of electrochemical setup, two gold electrodes connected by drop cast RGO film.

The sensitivity and selectivity of these simple source-drain sensors were evaluated by current vs. activity titration at a potential of 0.5 V vs the Ag/AgCl reference electrode, in 0.1 mM NaCl electrolyte solution. These measurements show that the B-RGO reference system exhibit no response at NaCl or KCl concentration lower than 10^{-4} M but high response from 10^{-3} M and up presumably due to lowered electrolyte resistance. RGO-crown[6] gives a similar response to NaCl, but a different response for KCl with a detection limit of 10^{-6} giving a linear response of 11.8 mV per decade of KCl concentration in the range of $10^{-6} - 10^{-3}$ M (Figure 40). These results show that this form of detection provides an increase in sensitivity

but at the cost of selectivity as the interference starts at 10^{-4} M concentrations. In conclusion, the RGO-crown[6] materials are able to detect K^+ in the range 10^{-6} M – 10^{-4} M by reducing the sheet resistance of the RGO film, but when the electrolyte concentration increase above 10^{-4} M the lowered electrolyte resistance opens an alternative ionic pathway through the aqueous solution that makes detection impossible.

Linear Fit of RGO-crown[6] (KCl)	
Slope	11.8 ± 2 mV / decade a_{KCl}
Fit range	$6 - 3$
Pearson's r^2	0.986
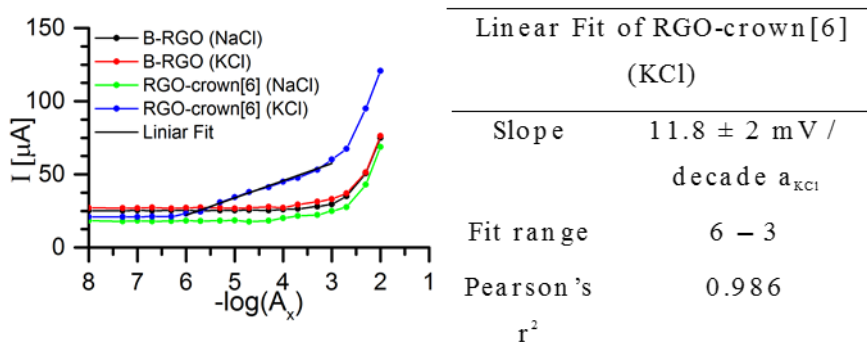
Figure 40: Current vs concentration titration with KCl and NaCl; for RGO-crown[6], and B-RGO, which is used as reference system.

3.3 Expanding the Series

RGO-crown[6] showed positive results in terms of selectively binding to K^+ even in the presence of large excess of Na^+, resulting in clear potentiometric responses. The series of materials was therefore expanded to include RGO modified with 12-crown[4]ether for Li^+ detection and 15-crown[5]ether for Na^+ detection, abbreviated RGO-crown[4] and RGO-crown[5] respectively. These two extra materials were synthesized based on the synthesis procedure used for RGO-crown[6] (section 3.2.3 page 35 & Scheme 4) for experimental procedure (section 7.1.2 page 106 to section 7.1.5 page 109).
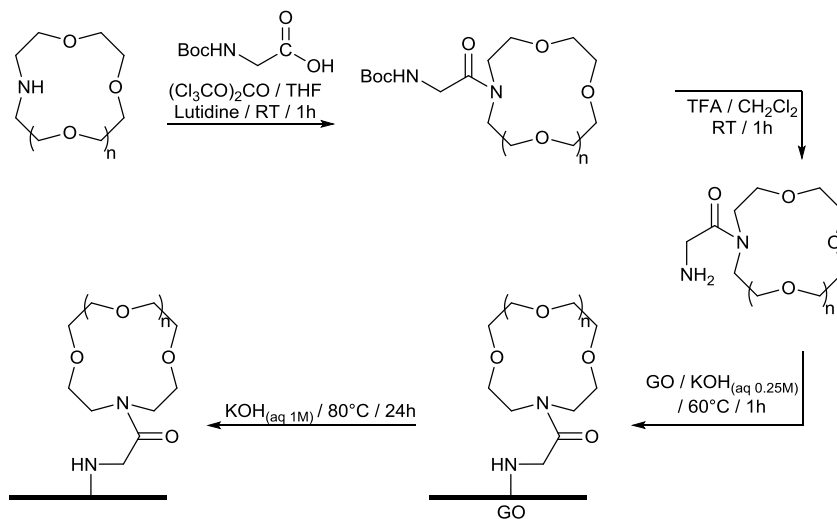
Scheme 4: Synthesis route to sensing material RGO-crown[4] and RGO-crown[5] where n = 1, 2 respectively.

3.3.1 Characterization

AFM Imaging

Nanosheet topography of RGO-crown[4] (Figure 41) and RGO-crown[5] (Figure 42) was characterized by AFM. Lateral XY dimensions are very similar to those of RGO-crown[6] yet slightly smaller 0.5-4 µm. The height of RGO-crown[4] was measured to be 1.0 – 1.2 nm very similar to RGO-crown[6] and consistent with monolayer dimension with increased height due to functionalization.

RGO-crown[5] height measurements show sheet heights between 0.9 – 1.7 nm. The images show higher tendency than RGO-crown[6] of clustered sheets indicative of minor aggregation to few-layered sheets as well as mono-layer sheets.
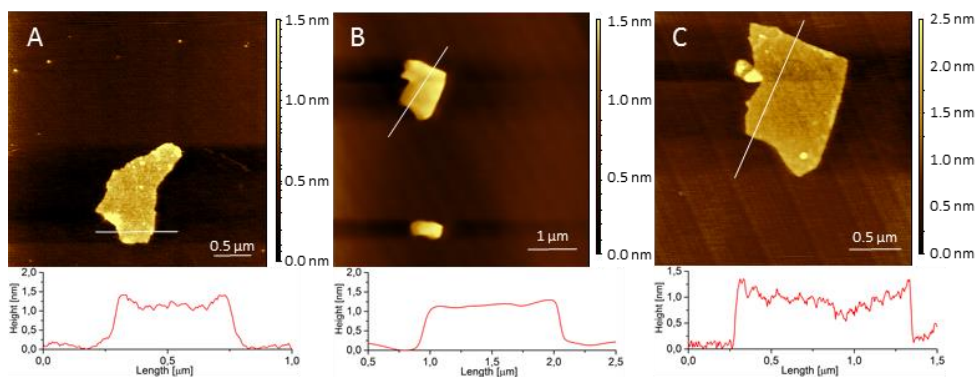
Figure 41: AFM images of RGO-crown[4] drop cast on mica showing a single-layer sheet of 0.5 – 4 μm XY-size range. Topography of three separate images with height profiles A) 3.5×3.5 μm². B) 5×5 μm². C) 3×3 μm².
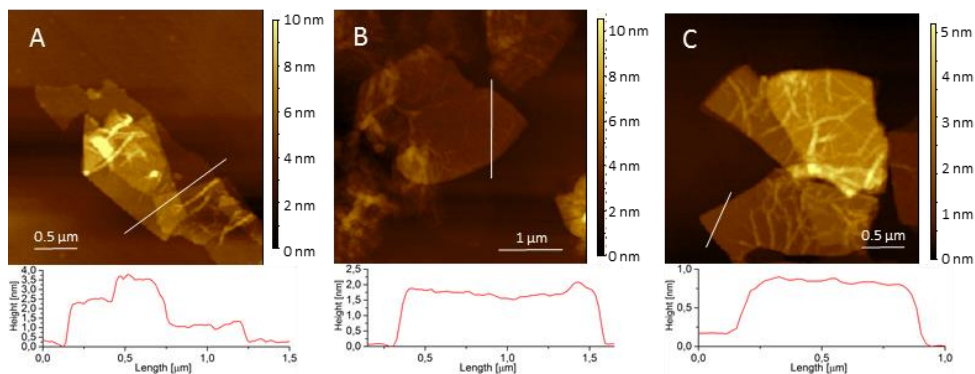
Figure 42: AFM images of RGO-crown[5] drop cast on mica showing single-layer sheet of 0.5-4 μm XY-size range. Topography of three separate images with height profiles A) 3×3 μm². B) 4×4 μm². C) 3×3 μm².

IR Spectroscopy

ATR-FTIR of RGO-crown[4] (Figure 43A) and RGO-crown[5] (Figure 43B) show the same fundamental vibrations as RGO-crown[6]; broad O–H stretch 3600 – 2600 cm^{-1}, aliphatic C–H stretch ($\approx$ 2900 cm^{-1}), carbonyl stretch 1720 cm^{-1} and several peaks in the 750 – 1500 cm^{-1} range, which can be assigned to –CH_2– bending ($\approx$ 1465 cm^{-1}); C–O stretch ($\approx$ 1300 & $\approx$ 1100 cm^{-1}); sp^2 C–H out of plane bending (1000 – 700 cm^{-1}), and possibly oxirane rings ($\approx$ 800 cm^{-1}). Compared to B-RGO the primary difference is an increase of the fundamental vibration at $\approx$ 1050 cm^{-1} assigned to C–O–C ether stretch from the attached crown-ether.
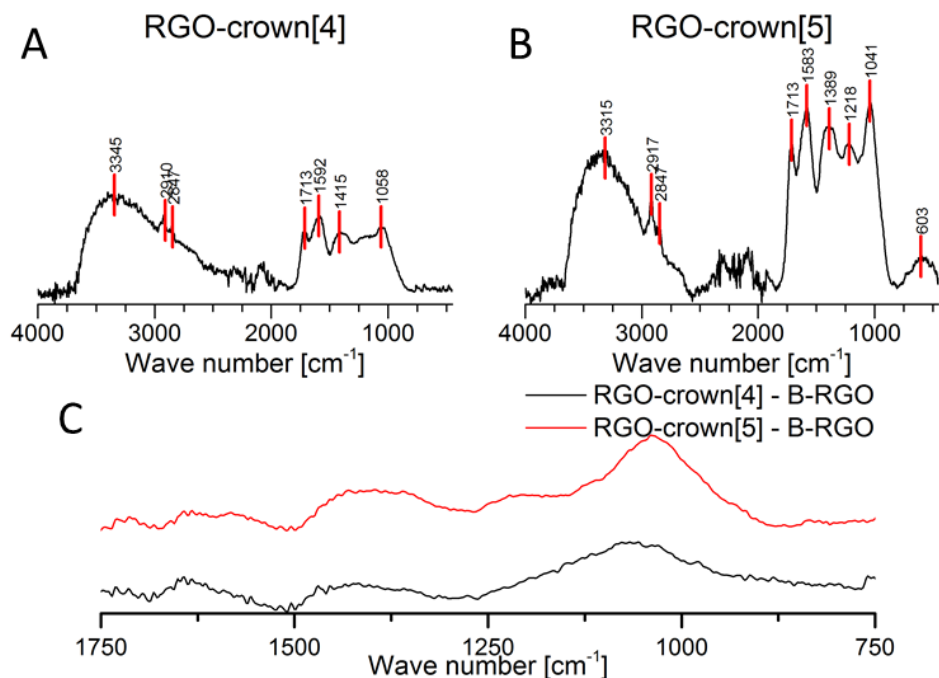
Figure 43: ATR-FTIR spectra of A) RGO-crown[4] and B) RGO-crown[4] C) difference spectrum between RGO-crown[6] and B-RGO, zoomed in on the 1500 – 750 cm^{-1} region.

XPS Characterization

Based on XPS-survey (Figure 44 and Table 6), the amount of crown-ether attached was evaluated, using the same method as described for RGO-crown[6] (section 3.2.5 page 42). In the material RGO-crown[4] one 12-crown[4]ether moiety ($C_{10}O_5N_2$) is attached per $\approx$ 52 graphene carbon were determined from XPS survey. From the X-ray structure[231] of 12-crown[4]ether an outer diameter of 7.68 Å can be found resulting in an area of 46.3 Å^2. The theoretical surface coverage can be determined from this data as $\approx$ 17 %. In the material RGO-crown[5] one 13-crown[5]ether moiety ($C_{12}O_6N_2$) attachment per $\approx$ 48 graphene carbon were determined from XPS survey. From X-ray structure[232] of 15-crown[5]ether an outer diameter of 8.77 Å can be found resulting in an area of 60.4 Å^2. The theoretical surface coverage can be determined from this data as $\approx$ 24 %.
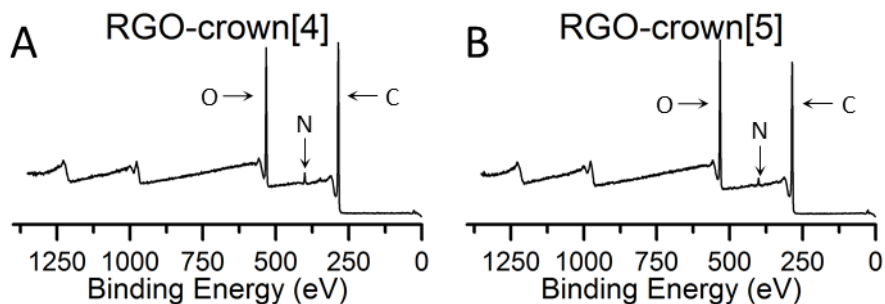
Figure 44: XPS – Survey of A) RGO-crown[4] and B) RGO-crown[5].

Table 6: Elemental composition as determined by XPS, as well as calculated contribution from crown-ether moiety and RGO sheet.

Sample	Raw data			Crown-ether			Sheet Contribution		
	%C	%O	%N	%C	%O	%N	%C	%O	C:O
GO	68.8	30.2	1.0	-	-	-	68.8	30.2	2.3
B-RGO	75.8	23.8	0.9	-	-	-	75.8	23.8	3.1
RGO-crown[4]	74.9	21.7	3.3	12	6	2.4	62.9	15.7	4.0
RGO-crown[5]	75.1	21.5	3.4	15	7.5	2.5	60.1	14.0	4.3

The alkaline reduction increases the sheet C:O ratio to 4.0 and 4.3 for RGO-crown[4] and RGO-crown[5], respectively consistent with the mild reduction observed for RGO-crown[6] and the B-RGO samples. C1s spectra (Figure 45) also indicate mild reduction in the form of reduced C–O peak intensity and shift of C–C peak maxima towards lower energy.
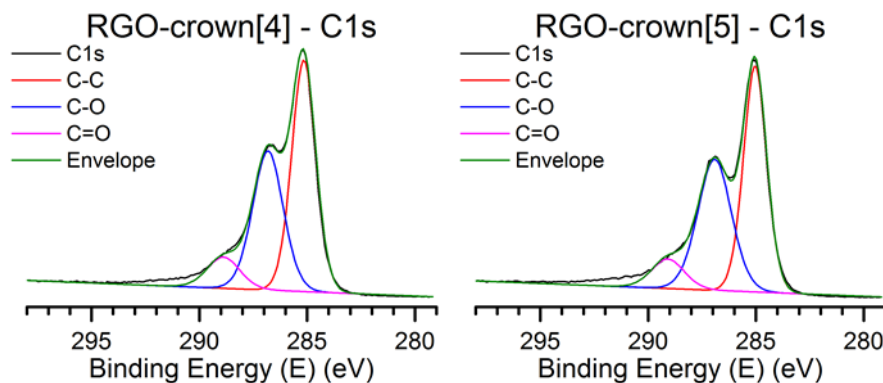
Figure 45: XPS C1s spectra of the A) RGO-crown[4] and B) RGO-crown[5]. Raw data (black); deconvoluted into C–C (red), C–O (blue) and C=O (purple) peaks; enveloped sum of deconvoluted peaks (green) showing fit to data.

Both RGO-crown[4] and RGO-crown[5] are thus determined to be functionalized successfully with their individual crown-ether based on IR spectroscopy. Using the XPS data it is found that the coverage per graphene carbon is similar for all the crown-ether modified materials, which the respective surface coverage reduced as the size of crown-ether is reduced: 52 C / crown-ether for RGO-crown[4] surface coverage ≈ 17 %; 48 C / crown-ether for RGO-crown[5] surface coverage ≈ 24 %; 46 C / crown-ether for RGO-crown[6] surface coverage ≈ 34 %.

3.3.2 Functional Test on Glassy Carbon Electrode

Functional electrodes were prepared using RGO-crown[4] and RGO-crown[5], by drop casting 15 µL of 1 mg/mL aqueous dispersion of these materials onto polished 7 mm^2 GCE and drying these overnight. Sensitivity and selectivity were then evaluated by potentiometric titration with nitrate salts in the concentration range of 10^{-7} to 10^{-1} M in electrolyte solution with 0.1 M masking salt for Li$^+$ sensing with RGO-crown[4], NaNO$_3$ was used as masking salt, while NH$_4$NO$_3$ was used as masking salt in the case of Na$^+$ sensing with RGO-crown[5].
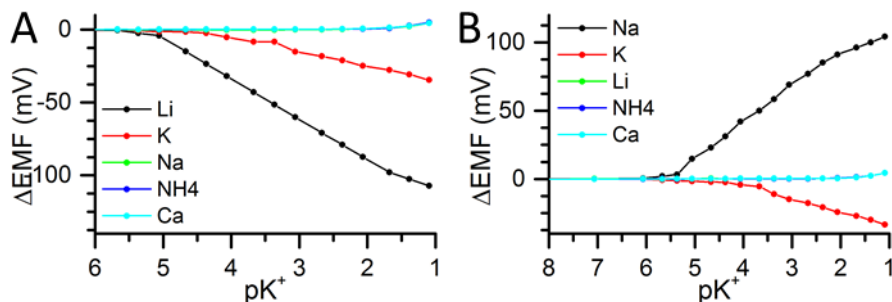
Figure 46: Sensitivity and selectivity tests by potentiometric titration of functionalized GCE. A) RGO-crown[4] and B) RGO-crown[5] with different salts (KNO₃, NaNO₃, LiNO₃, and Ca(NO₃)₂), in electrolyte of NaNO₃ and NH₄NO₃ for RGO-crown[4] and RGO-crown[5] respectively.

The RGO-crown[4] functionalized electrode shows response to Li^+ at a detection limit of 10^{-5} M with linear response up to 10^{-2} M with a potential increase of -22 mV per decade. The material show selectivity towards Li^+ over Ca^{2+}, Na^+, NH_4^+. However, interference from K^+ with -9 mV per decade potentiometric response above 10^{-4} M is seen. The RGO-crown[5] functionalized electrode show opposite potential response to Na^+ of 24 mV per decade in the concentration range 10^{-5} M – 10^{-2} M. The reason for the change in sign of potentiometric response in not known, but assumed to be a result of change of masking salt. RGO-crown[5] shows selectivity towards Na^+ over Ca^{2+}, Li^+, NH_4^+, but also interference response from K^+ above 10^{-4} M with potential increase of -8 mV per decade.

3.4   Conclusion & Perspective

The functionalization of RGO nanosheets with simple crown-ethers gave long-term stable functional materials and a surprisingly similar functionalization ratio. The materials produced selectively can bind target cations: 18-crown[6]ether moiety selectively binds K^+, with no interference from any of the tested ions. 15-crown[5]ether moiety binds Na^+ and 12-crown[4]ether binds Li^+, but here both show some interference from K^+.

The functionalized materials can be used to make membrane-free ion-selective electrodes based on potentiometric sensing, using high electrolyte concentration to mask signals from non-specific surface interactions with the electrode. The detection limit of these electrodes are 10^{-5} M, and they provide good selectivity over a range of ions up to 25 mM concentration. Furthermore, it was shown that disposable sensors could be prepared from these materials by drop casting onto screen-printed electrodes, illustrated with RGO-crown[6]. The disposable sensors provide near identical sensitivity and selectivity to the GCE based systems. Finally, it is shown that the source-drain based devices could enhance the detection limit to 10^{-6} M at

the cost of lowered selectivity, but with interference signals at 10^{-4} M concentrations of any salt. The interference is a result of a change in conductive pathway. When resistance of the electrolyte is sufficiently low the aqueous solution has lower resistance than the RGO film and conductivity in the former prevails. It would be interesting to investigate if the combined used of ion-selective membrane and these functional materials, would increase the sensitivity and/or selectivity of the individual parts, with both a membrane barrier and surface specific interactions.

Chapter 4   Azido-RGO: A   Possible
Universal Functionalization Platform

This chapter describes the design, synthesis and characterization of azide functionalized RGO (azido-RGO). Azido-RGO offers a general platform for further functionalization with complex molecular structures that would otherwise prove difficult due to harsh reduction condition used, during efficient GO reduction. As the first test, the Azido-RGO was functionalized with ferrocene that functions as a redox probe for electrochemical determination of coverage.

4.1   Introduction

Modification of GO by EDC coupling, or with a similar method, followed by its reduction to RGO is very often used as the synthesis strategy to functionalize graphene-like materials for many applications[141]. However, in the many cases where advanced chemical structures, such as receptors, are used as functionalities, this post modification reduction could be problematic, e.g. Schiff bases, which are a very used group of molecules for selective cation sensing[233], are for example susceptible to reduction too.

To tackle the problem of post-modification reduction, we have attempted to prepare a platform material that utilizes the efficiency of functionalization from GO, yet can be reduced before the desired final functionality is attached. Several different coupling reactions could be suitable for this purpose. Copper(I)-catalyzed azide-alkyne cycloaddition (CuAAC), however, has several benefits[234] such as: high yield, run at room temperature, compatible with water as solvent[235], and being catalyzed by Cu(I) without the need of additional ligands[235]. Furthermore, both parts of the coupling, i.e. azide and terminal alkyne, can easily be introduced to complex functional molecules such as recognition units, by simple efficient synthetic chemistry.

4.1.1   Copper(I)-Catalyzed Azide-Alkyne Cycloaddition

CuAAC is an adaption of 1,3-dipolar Huisgen cycloaddition[236] catalyzed by Cu(I) simultaneously discovered by both K.B. Sharpless *et al.*[237] and M. Meldel *et al.*[238] in 2002. In CuAAC, an azide and a terminal alkyne react to form a triazole-ring (Scheme 5). The improvement of this reaction by using Cu(I) as a catalyst makes it possible to run the reaction at room temperature and to introduce regio-selectivity in the triazole only forming 1,4-substituted triazole, rather than a mixture of 1,4 and 1,5 substitutions.
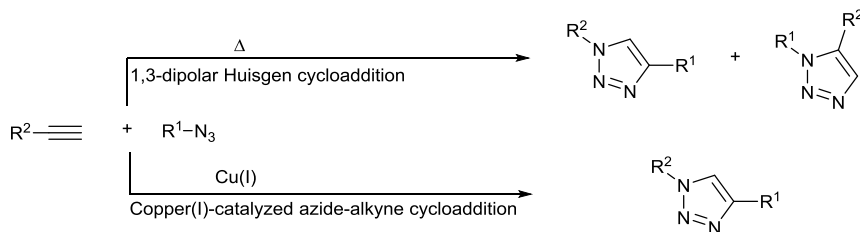
Scheme 5: 1,3-cycloaddtion of azide and alkyne. Top) un-catalysed Huisgen cycloaddion[236]. Bottom) CuAAC

The CuAAC reaction is connected to the concept of click chemistry possibly more than any other reactions, even called the "cream of the crop" of click reaction by Sharpless[239]. Click chemistry introduced by K.B. Sharpless *et al.*in 2001[239], aims to employ a few stable reaction pathways to create a wide selection of compounds with different properties, as a biomimetic approach to peptides. In essence, a click reaction should be simple, effective, with high yield, using benign solvent and reagents, and requires only simple purification. CuACC has been utilized in modification of a multitude of compounds e.g. peptides, DNA, nucleotides, carbohydrates, bioactive inhibitors, natural products, pharmaceuticals, macrocycles, calixarenes, rotaxanes, catanes, dendrimers and polymers, displaying how useful it is for coupling complex molecular structures without causing unwanted side reactions[234].

4.1.2   Reaction Mechanism

The mechanism of CuAAC has been proposed by Himo *et al.*[235] and Rodionov *et al.*[240] as a stepwise, rather than a concerted reaction (Scheme 6), which is believed to take place in the un-catalysted Huisgen reaction. Complexation of Cu(I) with the alkyne initiates the reaction, which increases the nucleophilicity and facilitates deprotonation of the terminal alkyne. The azide is then bonded to the complex via complexation of *N*-1 to the second Cu(I) organizing complex which imposes 1,4-regioselectivity. The complexation of the azide to Cu(I) activates the *N*-3 to make a nucleophilic attack on the *C*-4 carbon, forming a cyclic intermediate. The ring formation is completed by ring contraction and after protonation the Cu(I) catalyst can dissociate.
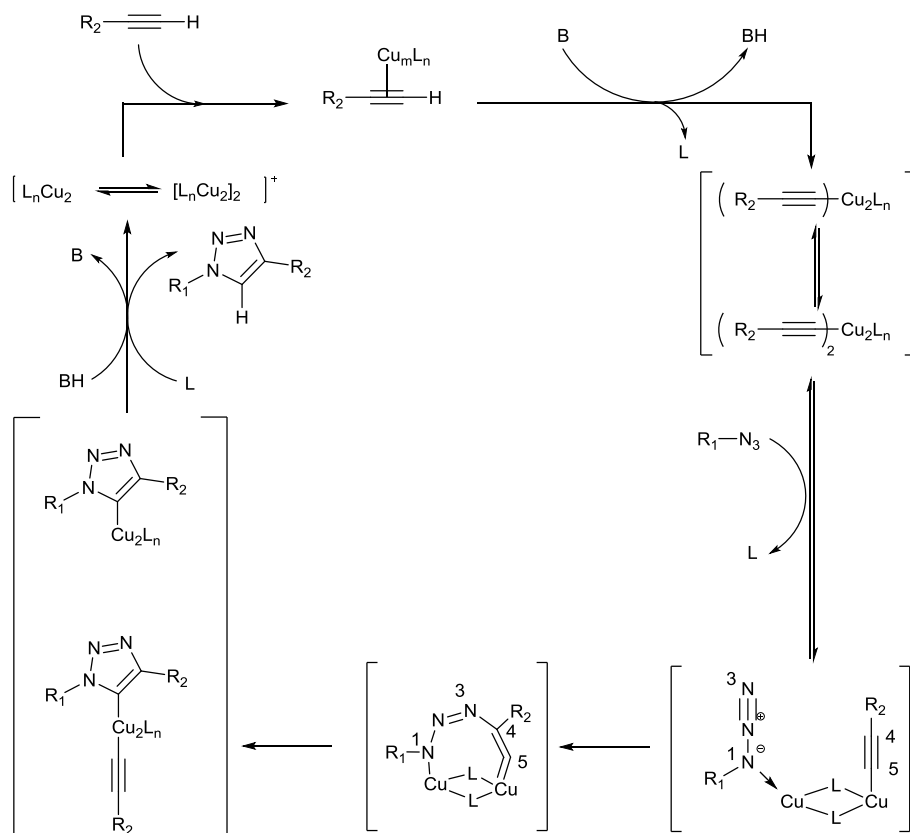
Scheme 6: Mechanism Proposed by Himo *et al.*[235] and Rodionov *et al.*[240]

4.1.3   Graphene-Like Materials for CuAAC

Not surprisingly many examples of utilizing the CuAAC reaction for modification of graphene-like materials are available. In most of these cases, GO Nanosheets are directly modified with either azides[205,241,242] or terminal alkynes[243–245] followed by CuAAC.

This type of functionalization has been used to introduce DNA[242], supramolecular recognition units[205], and polymers[243–245] onto GO nanosheets. CuAAC has also been used in combination of non-covalent attachment through aromatic anchoring units in the form of pyrene[246,247] or dopamine[248]. The method has even been used for functionalization of CVD[249] graphene by using diazonium salt to attach alkyne and further functionalization through CuAAC.

4.2 Synthesis

4.2.1 Design Consideration
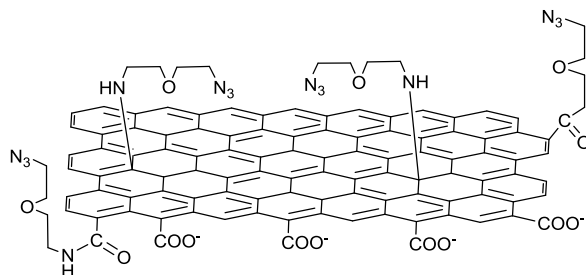
Figure 47: Schematic illustration of the proposed RGO-platform for functionalization using CuAAC coupling reaction.

Before synthesis of this RGO-platform (Figure 47), there are several important considerations to be evaluated for the design of the RGO-platform for CuAAC functionalization:

1. Effectively reduced GO to regenerate favourable graphene-like properties by efficient reduction method.
2. Introduced either azide or alkyne to provide an anchor for functionalization through CuAAC.
3. Utilize high chemical reactivity of GO to provide high coverage by functionalization before reduction.

$NaBH_4$ reduction is reported to be one of the most efficient reduction methods to regenerate electronic conductivity. This is therefore the reduction method that will be utilized here[152], when deciding whether to introduce terminal alkyne or azide functionality. First we consider if either survives the reduction. Azide is reduced to amine[250] and alkyne[251] can be reduced to alkane though slowly if not catalysed, making post reduction synthesis necessary, especially if another stronger reduction method should prove necessary.

The RGO-platform is intended for complex molecular functionalization. The synthetically more flexible terminal alkyne is therefore reserved for this complex molecular functionalization. The alkyne is thought to be more flexible than the azide because of the potential use of silane-protection for alkyne. Both azide[252,253] and terminal alkyne[254] can be introduced through organic synthesis. Azide functionalization should therefore be introduced to the platform. The post reduction introduction of azide could be done through a nucleophilic substitution with a good leaving group[253]. However, despite the fact that $NaBH_4$ generally exhibits poor reactivity towards halides, due to ineffective S_N2 reactions[255], it was decided

that this choice posed an unnecessary risk, and instead the azide was introduced through activation of primary alcohol through Mitsunobu reaction[252].

The need for anhydrous conditions in the Mitsunobu reaction opens for the possibility of using isocyanate functionalization of GO[185]. However, the success of functionalizing GO with nucleophilic ring opening of epoxide from a previous project warrants testing to further improve functionalization EDC coupling can be done simultaneously.

Two possible routes to azido-RGO were therefore used (Scheme 7 & Scheme 8). "*2-(2-aminoethoxy)ethan-1-ol*" was chosen for the following reasons: It is terminated by the amine and alcohol groups needed, secondly it is a short flexible linker which can increase interaction with water, helping to disperse the RGO-sheets in water, and finally it is commercially available.

After the work of A. Dimev *et al.*[142] came to my attention I wanted to test if I could achieve even higher functionalization coverage by utilizing a non-aqueous work-up after GO synthesis as the reported high reactivity due to a presumed higher concentration of basal plane epoxides, for the work-up of this GO. Ethyl acetate (EtOAc) was used (experimental section 7.1.1 page 104). Hereafter, GO is referred to as either anhydrous GO if it is GO where EtOAc was used during synthetic work-up, or aqueous GO when H_2O used in the workup.

4.2.2   Synthesis Procedure

The two synthesis pathways to azido-RGO discussed above either through nucleophilic approach, i.e. combined EDC coupling and nucleophilic ring opening of epoxides (Scheme 7), or through electrophilic approach, i.e. isocyanate functionalization (Scheme 8).

Before synthesis, GO obtained from both aqueous and anhydrous workup was extensively dried. This was done by first centrifugation to remove most solvent followed by vacuum drying, and secondly by five times repeated dispersion and centrifugation with anhydrous THF to further remove residual water.
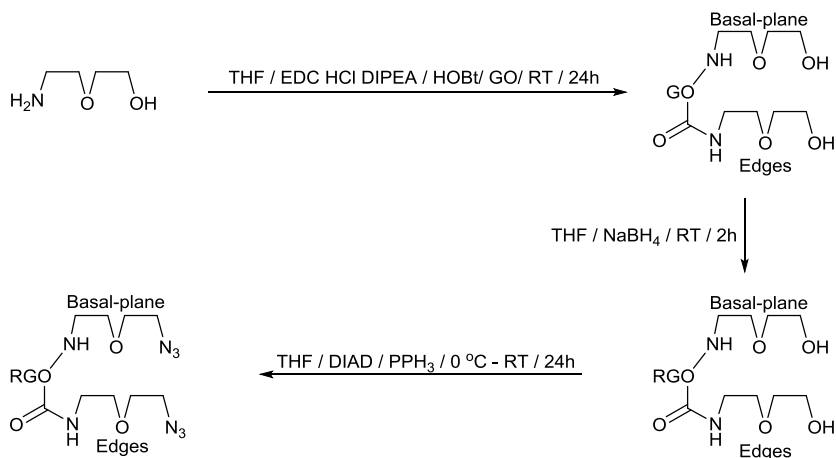
Scheme 7: Overview of the nucleophilic approach to synthesis of azido-RGO.

For the nucleophilic approach, the glycol linker was directly attached to GO through the amine by combining EDC coupling[256] and nucleophilic ring opening of epoxides[183] (experimental section 7.1.9 page 110), and followed by reduction with $NaBH_4$[152] (experimental section 7.1.11 page 111), before the final Mitsunobu reaction[257] (experimental section 7.1.13 page 112). The reactions were performed in anhydrous THF with centrifugation to remove excess reagents and single wash with anhydrous THF between each step. After synthesis, the final product was centrifuged, washed once with anhydrous THF and five times with H_2O, and further purified by dialysis.
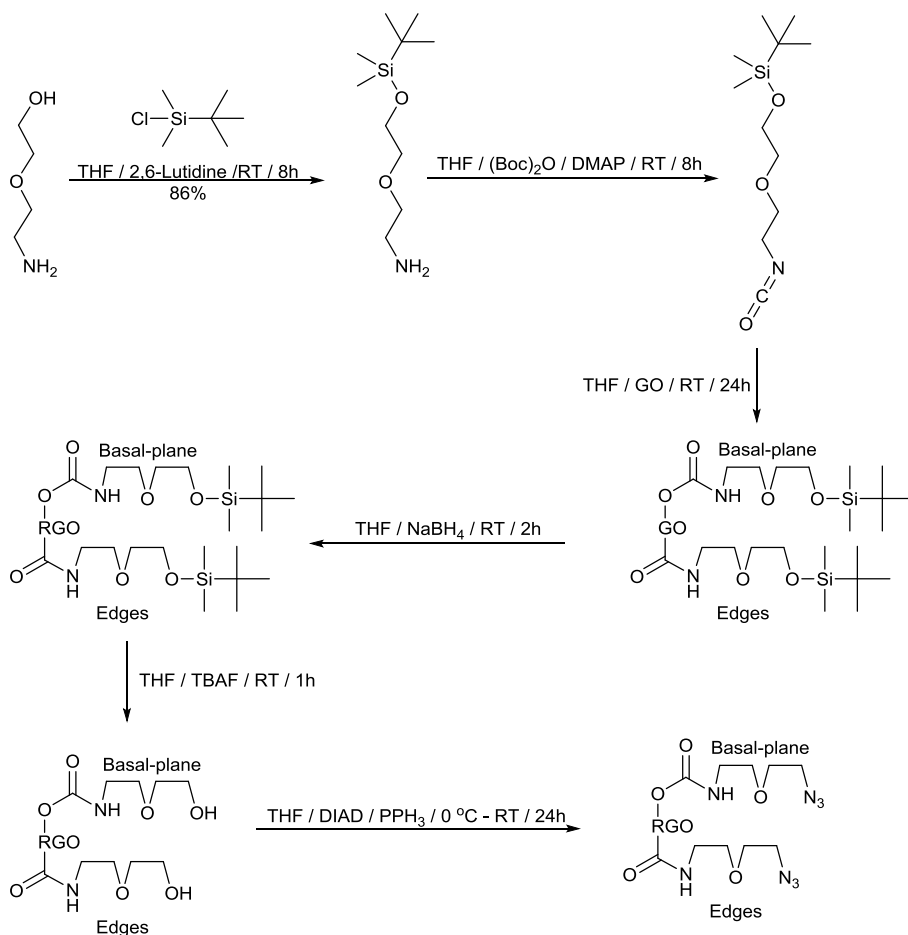
Scheme 8: Overview of the electrophilic approach to synthesis of azido-RGO.

For the electrophilic approach, the alcohol of the glycol linker was first protected with a silyl protection group[258] (experimental section 7.1.8 page 110). Then the amine was transformed to an isocyanate catalyzed by 4-dimethylaminopyridine (DMAP)[259]. The isocyanate was used directly for functionalization of the GO[185] (experimental section 7.1.10 page 111). The functionalized GO was then reduced by NaBH$_4$[152] (experimental section 7.1.11 page 111), and the silyl protection group removed using TBAF[260] (experimental section 7.1.12 page 112), before the final Mitsunobu reaction[257] (experimental section 7.1.13 page 112). The reactions were performed in anhydrous THF with centrifugation to remove excess reagents and washed once with anhydrous THF between each step. After synthesis, the final product was centrifuged, washed once with anhydrous THF and five times with H$_2$O, and further purified by dialysis.

4.3 Characterization

4.3.1 IR Spectroscopy

For the nucleophilic synthesis path before the Mitsunobu reaction, the ATR-FTIR shows an increase in the intensity of C–H stretch at 2950 cm^{-1} and C–O 900 cm^{-1} (Figure 48 & Figure 49 blue). After azide introduction in the post reduction the Mitsunobu reaction, the characteristic fundamental vibration from azide stretch at $\approx$ 2100 cm^{-1} is found in the IR spectrum (Figure 48 & Figure 49 Green) indicating a successful transformation. When comparing the relative peak intensity of the azido vibration with other peaks, a clear distinction between anhydrous and aqueous GO materials is observed where the intensity in the material prepared from anhydrous GO shows significantly more intense azido peak.
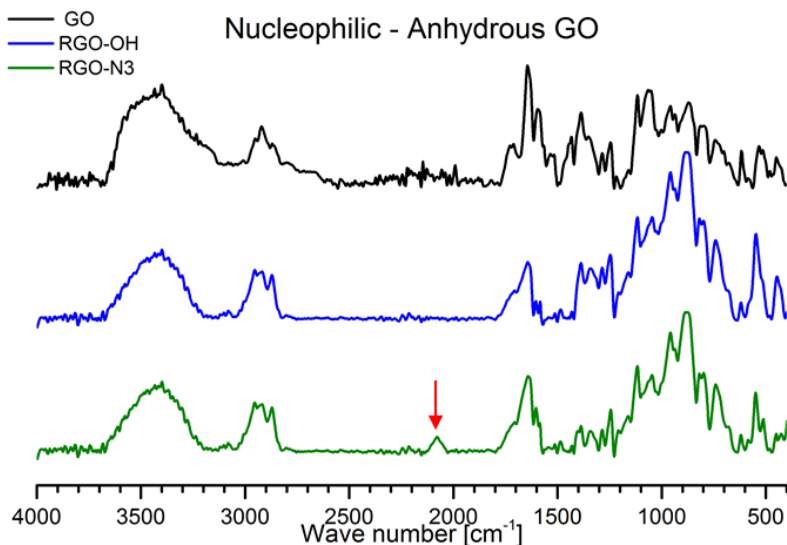
Figure 48: ATR-FTIR spectra of GO starting material (black) and the synthetically prepared, from anhydrous GO using nucleophilic strategy, material before the Mitsunobu reaction (blue) and after the Mitsunobu reaction (green).
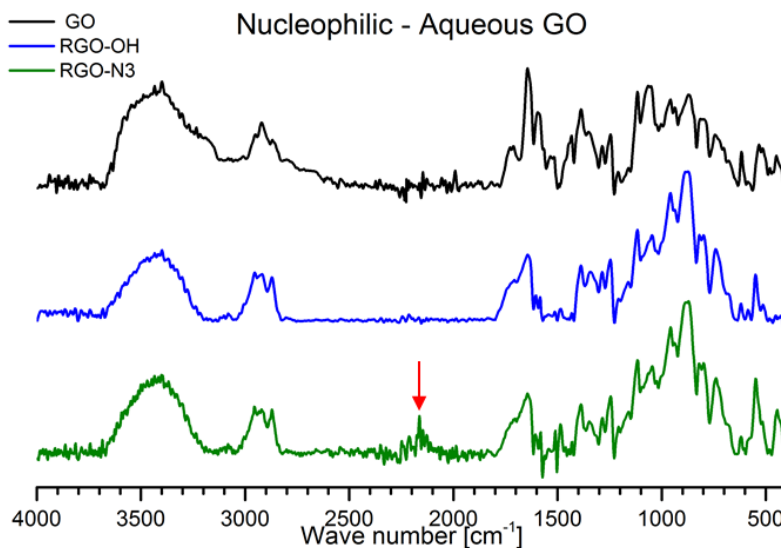
Figure 49: ATR-FTIR spectra of GO starting material (black) and the synthetically prepared, from aqueous GO using nucleophilic strategy, material before the Mitsunobu reaction (blue) and after the Mitsunobu reaction (green).

The longer electrophilic synthesis path starts by the introduction of silyl protected glycol. The introduction of this functionalization is clearly seen in the IR spectrum (Figure 50 & Figure 51 red) by a significant increase of intensity at $2850 - 2950$ cm^{-1} corresponding to sp^3 C–H stretch from the many methyl-groups on the silyl protection. Only a small difference is observed between the two GO starting materials. When the silyl protection group is removed with TBAF and the GO reduced by NaBH$_4$ (Figure 50 & Figure 51 Blue), the C–H stretching peak is reduced and the most prominent vibration is the C–O stretch at 1000 cm^{-1} from ether and alcohol. When the alcohol on the RGO is substituted with azide by the post-reduction Mitsunobu reaction the fundamental vibration for azide stretch at ≈ 2100 cm^{-1} is observed (Figure 50 & Figure 51 green). As for the nucleophilic synthesis path, an indication of better functionalization is achieved after the final step for the anhydrous GO compared to aqueous GO is shown by the peak intensity of the azide peak at 2100 cm^{-1}.
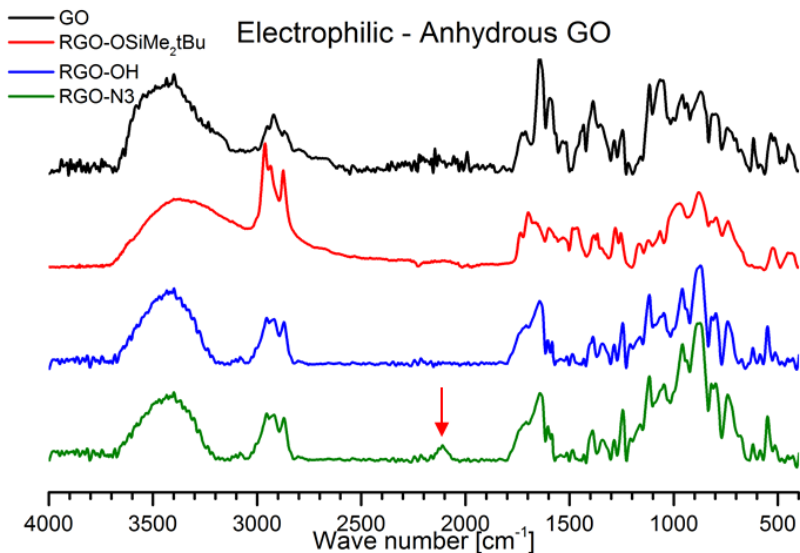
Figure 50: ATR-FTIR spectra of GO starting material (black) and the synthetically prepared, from anhydrous GO using electrophilic strategy, material before the Mitsunobu reaction (blue) and after the Mitsunobu reaction (green).
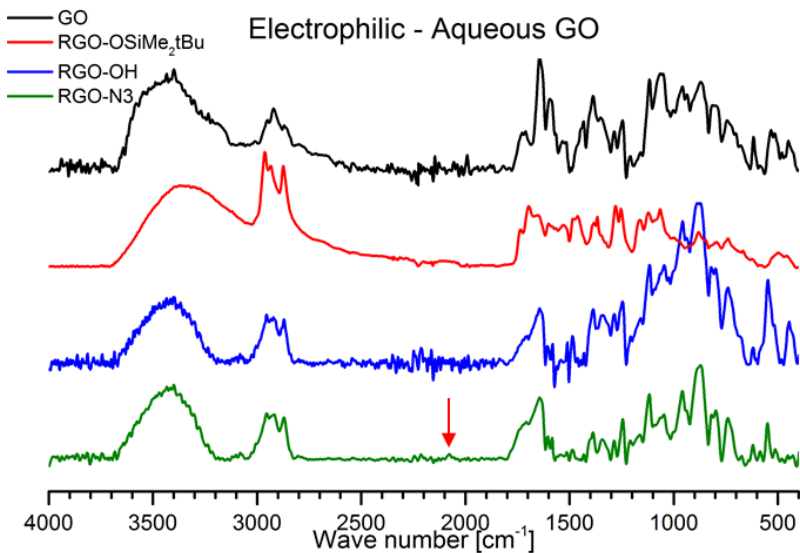
Figure 51: ATR-FTIR spectra of GO starting material (black) and the synthetically prepared, from aqueous GO using electrophilic strategy, material before the Mitsunobu reaction (blue) and after the Mitsunobu reaction (green).

4.3.2   XPS Characterization

The four variants of the synthesized azido-RGO were further studied by XPS. The survey spectra of the elemental composition show that all the materials were functionalized with nitrogen containing functionalities (Figure 52 & Table 7).
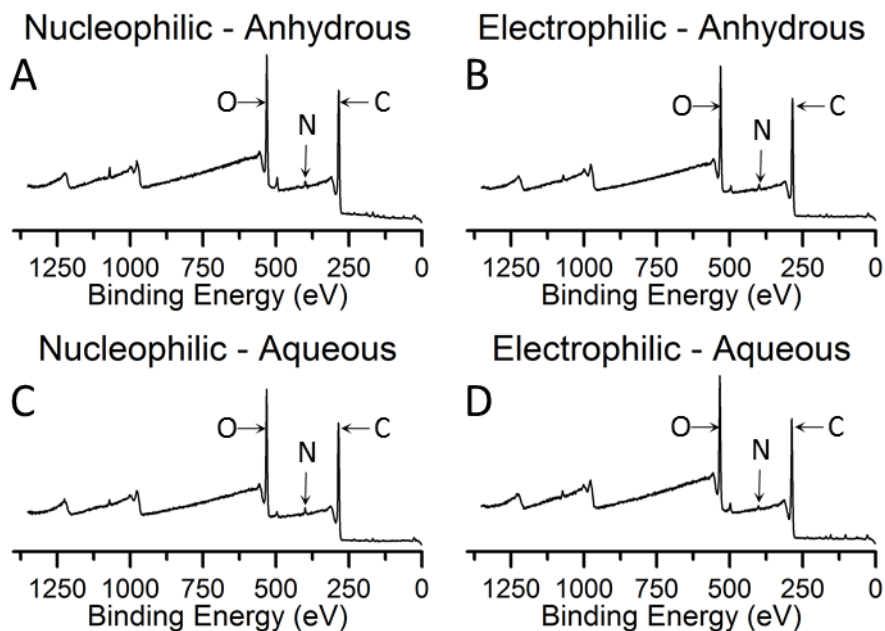
Figure 52: XPS-survey spectra of the four synthesized azido-RGO materials A) nucleophilic approach using anhydrous GO as starting material. B) Electrophilic approach using anhydrous GO as starting material; C) nucleophilic approach using aqueous GO as starting material; D) electrophilic approach using aqueous GO as starting material. All show C, O and N as well as some Na impurity. In D) the silicon from sample plate is also observed.

Table 7: Elemental composition of the azido-RGO materials as derived from XPS-survey.

	% C	% O	% N	Other elements	C : O
GO - Anhydrous	66.85	32.02	0.13		2.1
GO - Aqueous	66.54	32.30	0.16		2.1
Nucleophilic – Anhydrous	81.24	15.57	3.19	Na	5.2
Electrophilic – Anhydrous	80.94	16.53	2.53	Na	4.9
Nucleophilic – Aqueous	78.22	19.16	2.62	Na	4.1
Electrophilic – Aqueous	79.18	19.32	1.5	Na, Si	4.1

From the nitrogen content alone the nucleophilic approach (3.1 9% and 2.62 %) seems preferable to isocyanate approach (2.53 % and 1.5 %). Furthermore, the anhydrous GO shows

higher N content (3.19 % and 2.53 %) than the aqueous GO (2.62 and 1.50 %). As we have chemically different nitrogen species in the forms of amine, amide and azide as confirmed by IR spectroscopy, we could obtain further information from the N1s spectrum (Figure 53).

The binding energy of amine and amide are almost the same ($\approx$ 400.5). The three nitrogens in the azide give rise to two different binding energies ($\approx$ 399 and $\approx$ 402 with a 2:1 intensity ratio)[261]. By normalizing the area of the amine/amide peak of the deconvoluted spectrum we can estimate a conversion yield for the Mitsunobu reaction under the assumption that all amines and amides in the material are introduced as a part of the glycol linker.
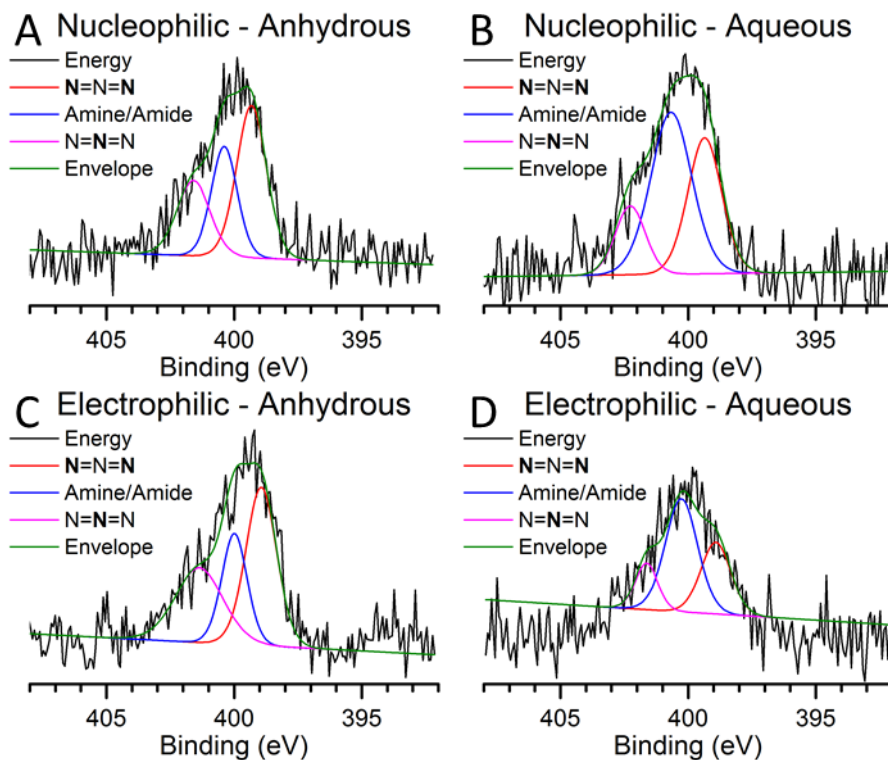
Figure 53: XPS-N1s spectra of the four synthesized azido-RGO materials. Raw data (black) deconvoluted amine/amide (blue); deconvoluted azide (red and purple); envelope of the deconvoluted spectrum (green). A) Nucleophilic approach from anhydrous GO starting material. B) Electrophilic approach from anhydrous GO starting material. C) Nucleophilic approach from aqueous GO starting material. D) Electrophilic approach from aqueous GO starting material.

Table 8: the ratio of Amine/Amide to azide estimated from deconvoluted XPS-N1s spectra, and calculated conversion yield.

	N=**N**=N ≈399 eV	Amine ≈400.5 eV	**N**=N=**N** ≈402 eV	Conversion yield
Nucleophilic – Anhydrous	0.87	1	1.59	83 %
Electrophilic – Anhydrous	0.67	1	1.43	70 %
Nucleophilic – Aqueous	0.31	1	0.69	33 %
Electrophilic – Aqueous	0.29	1	0.59	29 %

The low nitrogen content in the sample and reduced the signal to noise ratio make deconvolution of the spectra difficult. By fixing an approximate 2:1 intensity ratio of the two azide peaks it is, however, possible to deconvolute the data (Figure 53). An interesting difference between the starting materials is revealed. The azido-RGO synthesized from anhydrous GO shows a high azide conversion yield of 83 % and 70% for nucleophilic and electrophilic approaches, respectively. However, the azide conversion yield for azido-RGO synthesized from aqueous GO is only 33 % and 29 % for nucleophilic and electrophilic approaches, respectively (Table 8).

As all reaction conditions throughout the synthesis are kept the same, the significantly lower conversion yield must be a result of difference in the starting materials themselves, either in the chemical nature of the GO material as suggested by Dimiev *et al.*[142] or another possible reason could be that some strongly bound water is not removed by even the extensive drying process. Water could reduce the effectiveness of the Mitsunobu reaction by reaction with the triphenylphosphine. Residual water could also help explain the lower nitrogen content through isocyanate attachment compared to the nucleophilic method.

The reduction of the graphene sheet, can also be evaluated from the XPS survey spectra (Table 7). The C:O ratio of the graphene-like material has been increased, from approximately 2:1 in the GO starting material to 5:1 after reduction for the anhydrous GO and slightly lower 4:1 for aqueous GO. This is a significant reduction of the oxygen content, but still leaves considerable oxygen containing functional groups. Some of these residual oxygens can be accounted for by edge carboxylic acid groups possible functionalized into amides. Another small fraction is a result of introduction of oxygens from the glycol linker. However, with the limited functionalization apparent from the nitrogen introduction this only amounts to a small part. A significant amount of this oxygen must therefore originate from non-reduced basal plane oxygen functionalities.

From the XPS C1s spectra (Figure 54) of all four materials, the intensity of the C–C and C–O/C–N peaks are almost 1:1, which further supports that significant basal plane oxygen functionalities, must still be present in the material.
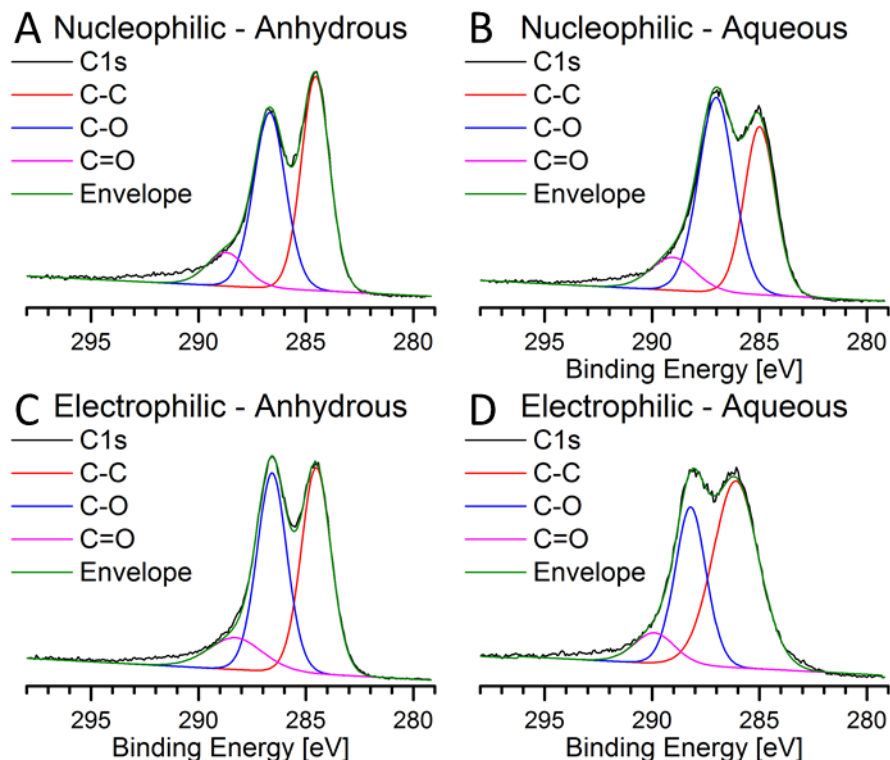
Figure 54: XPS-N1s spectra of the four synthesized azido-RGO materials raw data (black) deconvoluted C–C (red), C–O (blue) C=O (purple) and envelope of the deconvoluted spectrum (green). A) Nucleophilic approach from anhydrous GO starting material. B) Nucleophilic approach from aqueous GO starting material. C) Electrophilic approach from anhydrous GO starting material. D) Electrophilic approach from aqueous GO starting material.

	C–C ≈284.8 eV	C–O ≈286 eV	C=O ≈288.5 eV
Nucleophilic – Anhydrous	46.95	43.19	9.86
Electrophilic – Anhydrous	47.17	45.75	7.08
Nucleophilic – Aqueous	38.27	51.02	10.71
Electrophilic – Aqueous	58.14	33.72	8.14

Table 9: Data from the deconvoluted XPS-C1s spectra relative C–C, C–O, C=O content.

4.3.3   AFM Imaging

AFM was used to verify that the graphene-like materials remain exfoliated in the dispersion after the synthesis and do not aggregate into multi-layered structures.
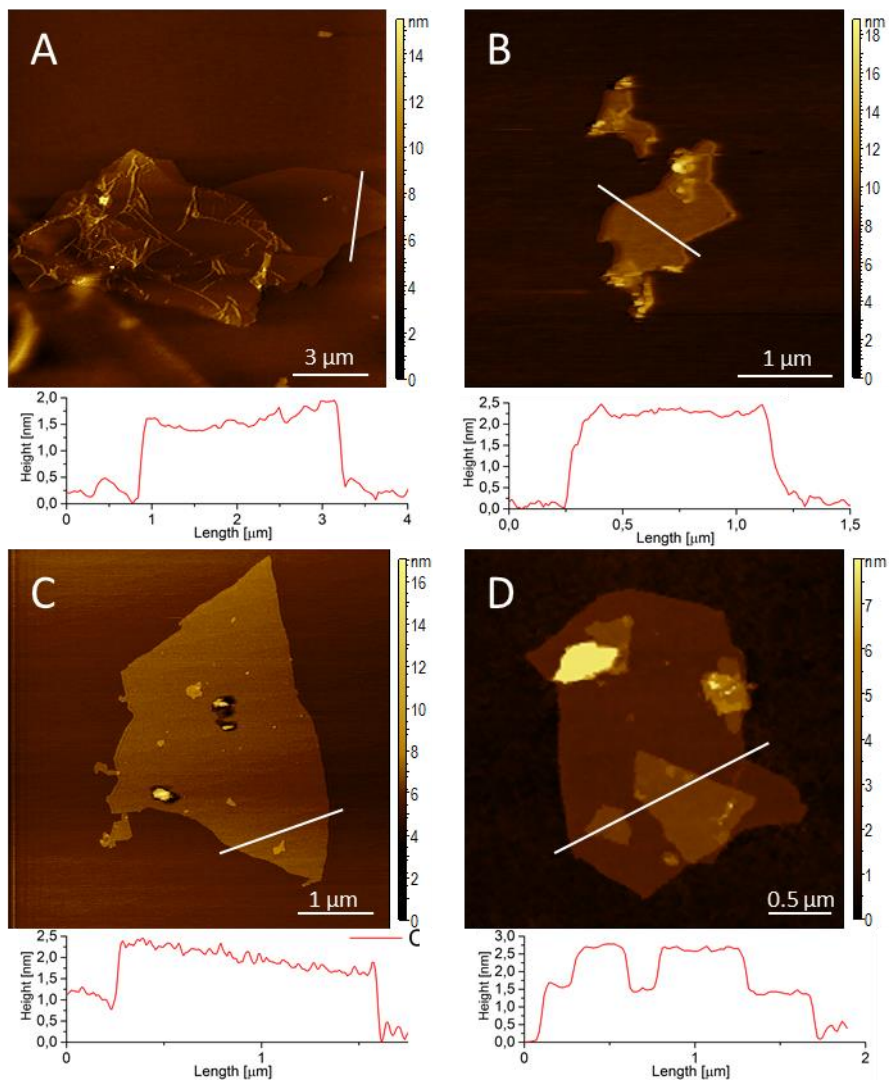
Figure 55: AFM Topography images with height profiles of Azido-RGO drop cast on mica showing single-layer sheets of 0.25 – 4 µm XY-size range. A) Nucleophilic approach from anhydrous GO starting material. B) Electrophilic approach from anhydrous GO starting material. C) Nucleophilic approach from aqueous GO starting material. D) Electrophilic approach from aqueous GO starting material.

We can see from the AFM images that all four materials remain exfoliated and mono-layered graphene-like sheets are the primary substituent of the synthesized materials. After synthesis the lateral sheet size is significantly reduced from (1 – 8 µm) to (0.25 – 4 µm) most of them about one µm. The height of the sheets are approximately 1.5 nm. This is significantly higher than that normally observed for pure RGO but can be explained by the glycol functionalities on both sides of the graphene basal plane.

4.4 Functionalization with Ferrocene

To determine accurately to what extent this azido-RGO can be functionalized by CuAAC, it was further functionalized with a redox probe i.e. ferrocene (Figure 56). The effective loading can then be obtained from the charge needed for oxidation or reduction of the attached redox probe using cyclic voltammetry (CV).
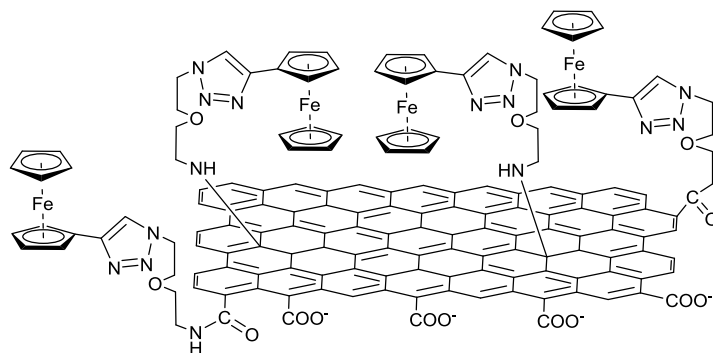
Figure 56: Schematic illustration of ferrocene functionalized RGO.

4.4.1 Attachment of Ferrocene
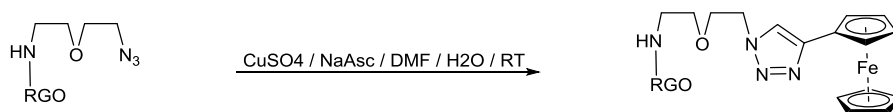
Scheme 9: reaction condition for the CuAAC coupling of ethynlferrocene and Azido-RGO.

The CuAAC coupling reaction between ethynylferrocene (redox probe) and the four different azido-RGO materials were performed in a mixture of DMF (as Ethynylferrocene is poorly soluble in water) and water (1:1) over 2 hours. $CuSO_4$ reduced *in situ* by ascorbic acid was used as Cu(I) source, with no stabilizing ligands used. The ferrocene functionalized graphene-like material was purified by repeated washing with DMF and then water before being dialyzed (Scheme 9) (experimental section 7.1.14 page 113).
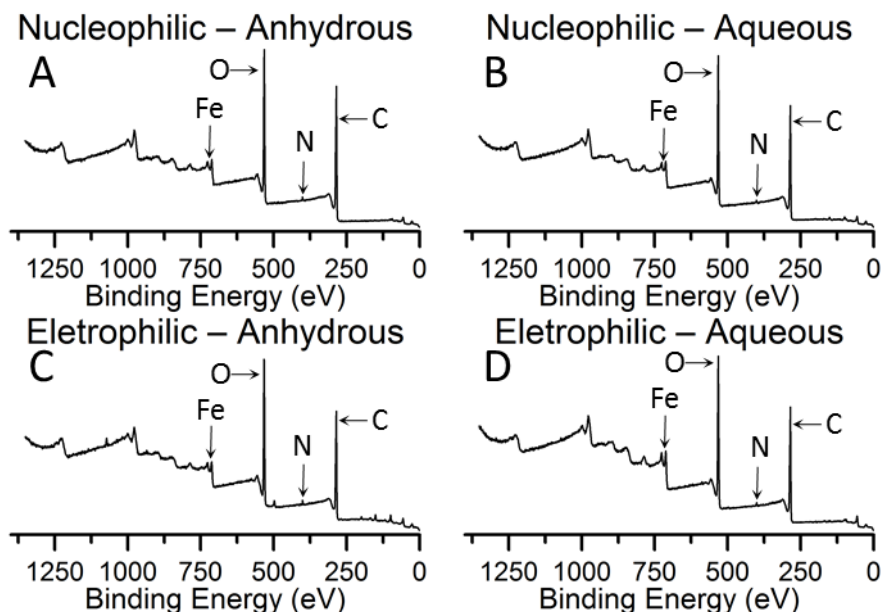
Figure 57: XPS-survey spectra of the four synthesized ferrocene functionalized RGO materials. A) Nucleophilic approach from anhydrous GO starting material. B) Nucleophilic approach from aqueous GO starting material. C) Electrophilic approach from anhydrous GO starting material. D) Electrophilic approach from aqueous GO starting material. All show C, O, N and Fe. In B-D the silicon sample plate also gives a in small Si signal and in C a NaCl impurity is evident.

Table 10: Elemental composition of the ferrocene functionalized RGO materials as derived from XPS-survey.

	% C	% O	% N	% Fe	Other elements	C : O
Nucleophilic – Anhydrous	80.11	15.37	3.18	1.34		5.2
Electrophilic – Anhydrous	80.22	16.04	2.51	1.23	Si, Na, Cl	5.0
Nucleophilic – Aqueous	77.73	18.96	2.59	0.72	Si	4.1
Electrophilic – Aqueous	78.96	19.26	1.32	0.46	Si	4.1

XPS-survey spectra (Figure 57 & Table 10) as well as Fe2p spectra show introduction of Fe2p signal at ≈720 eV, split into two peaks at 726 eV and 712 eV due to spin-orbit coupling (Figure 58). This binding energy is consistent with Fe(II)[262], otherwise the XPS data are in strong agreement with XPS on Azido-RGO, i.e. with no significant difference observed.
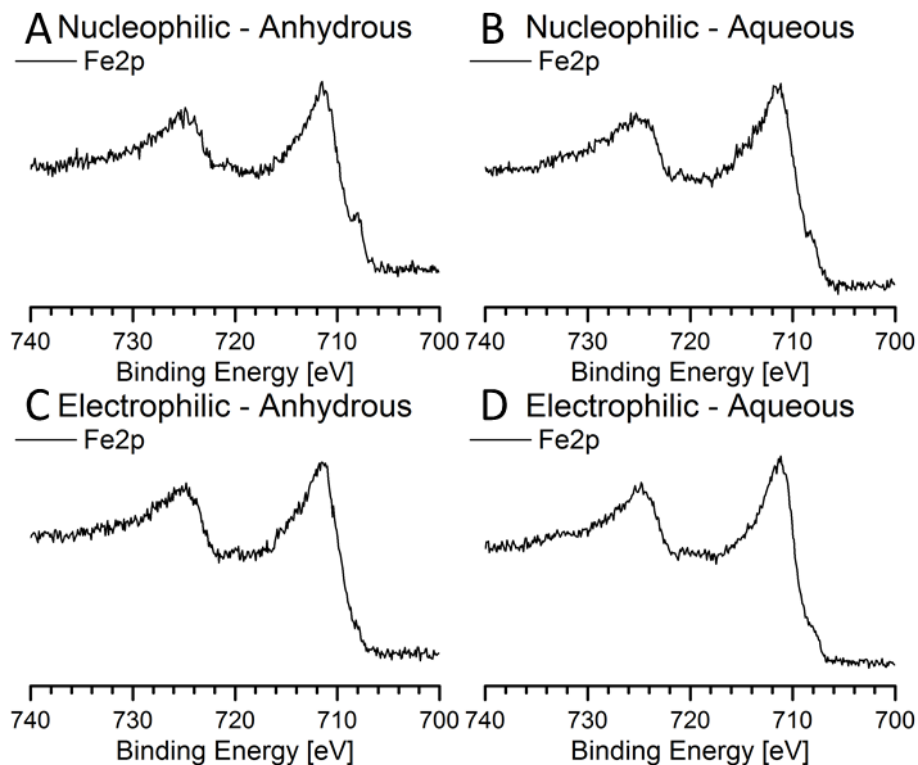
Figure 58: Fe2p spectra of ferrocene functionalized RGO. A) Nucleophilic approach from anhydrous GO starting material. B) Nucleophilic approach from aqueous GO starting material. C) Electrophilic approach from anhydrous GO starting material. D) Electrophilic approach from aqueous GO starting material, all showing two peaks at 726 eV and 712 eV consistent with Fe(II).

We can see a slight increase in sheet height compared to azido-RGO (≈ 1.5 nm), from the AFM images, to about 1.7 nm no other change of the sheet topography is observed from AFM (Figure 59).
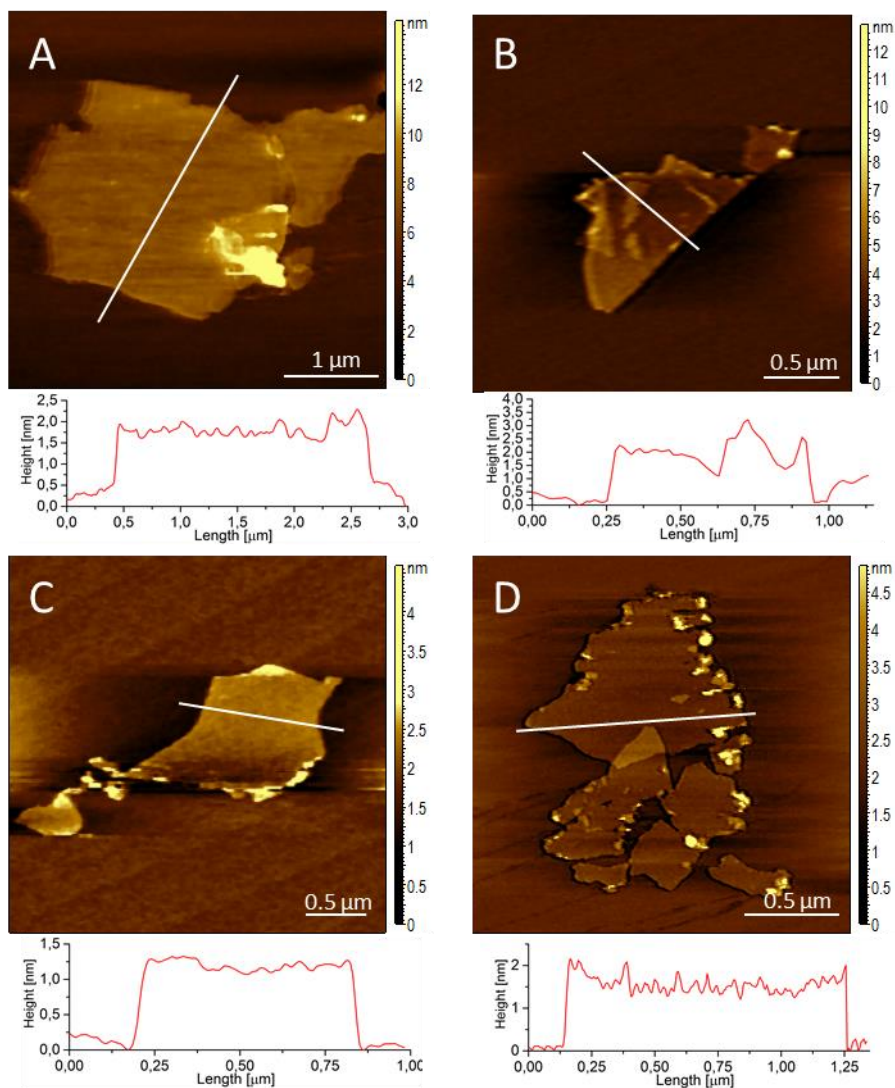
Figure 59: AFM Topography images with height profiles of ferrocene functionalizaed RGO drop cast on mica showing single-layer sheet of 0.25 – 4 µm XY-size range. A) Nucleophilic approach from anhydrous GO starting material. B) Nucleophilic approach from aqueous GO starting material. C) electrophilic approach from anhydrous GO starting material. D) Electrophilic approach from aqueous GO starting material.

4.4.2 Electrochemical Test

Functionalized GCEs were prepared by drop casting 10 µL of aqueous dispersions of ferrocene functionalized RGO onto freshly polished 7 mm^2 GCEs and dried *in vacuo* 1 hr. These functional electrodes were tested in a three-compartment electrochemical cell, with the functionalized GCE as working electrode, freshly flame annealed Pt-wire as counter electrode and saturated calomel electrode (SCE) as reference electrode in an electrolyte solution of 0.1 M H_2SO_4.

Firstly, the ferrocene coverage of all four ferrocene-RGO materials and one of the azido-RGO materials as reference were evaluated based on electro-oxidation. Two different loading amounts 1 µg and 0.1 µg was tested by varying the concentration of the dispersion used for drop casting. The electrodes were cycled for 100 scans in the potential range 0 – 0.8 V at 100 mV/s. All four ferrocene-RGO materials show the ferrocene redox peak at 0.5 V, but the current is significantly different. The peak separation is large ($\approx$ 200 mV), presumably due to slow charge transfer reaction or capacitive charging phenomena. The reference azido-RGO exhibits no redox peak in the potential window used (Figure 60).
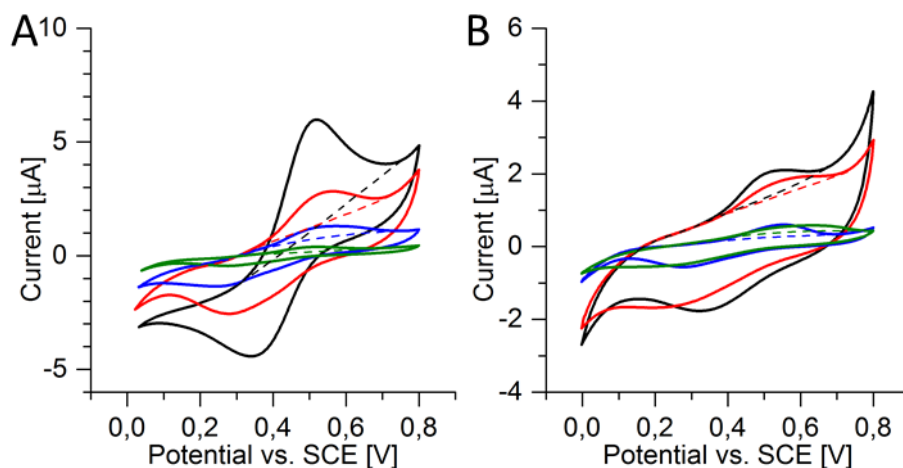
Figure 60: CV of ferrocene functionalizaed RGO drop cast on GCE at A) 1 µg and B) 0.1 µg; Nucleophilic approach from anhydrous GO (Black), electrophilic approach from anhydrous GO (Red), nucleophilic approach from aqueous GO (Blue), electrophilic approach from aqueous GO (Green), Reference Azido-RGO (Magenta).

From the anodic charge of the ferrocene oxidation, as determined from CV (Figure 60), we can calculate the molar amount of redox centres attached to the material, as we know that the ferrocene oxidation is a single electron transfer.

Equation 4 $$n = \frac{Q}{z \cdot F}$$

Where n is molar amount of redox units, Q is the charge, z is the number of electrons involved in CT, and F is Faraday constant. Knowing the molar amount of redox centres and the mass of the drop cast material on the electrode, the molecular weight per redox centre in the material can be determined.

Equation 5 $$Mw_{redox} = \frac{m}{n}$$

Equation 6 $$Mw_{Sheet} = Mw_{redox} - 339.2 g/mol$$

Where m is the mass of the drop cast material, Mw_{redox} is the molecular mass per redox centre, Mw_{sheet} is the molecular mass of the RGO sheets per redox centre. Determined by subtracting the molecular mass of the known chemical structure of the attached ferrocene and linker ($C_{16}H_{19}FeN_4O^{\bullet}$, 339.2 g/mol) from the molecular mass per redox centre, to find the molecular mass of the graphene sheet per redox centre. Under the assumption that the graphene sheets only consist of carbons, the number of carbon atoms per ferrocene can be determined, and from the surface area per carbon (5.246 $Å^2$), the average space between each pair of redox units in the material can be determined (Table 11). The same coverage of azide anchoring groups is available in azido-RGO assuming a 1:1 correlation between ferrocene and anchors.

Table 11: CV charge data and calculations of redox centre coverage on RGO-sheet. Top 1 µg and bottom 0.1 µg drop cast material.

Sample	Charge [C]	n_{e^-} [pmol]	Mw_{redox} [g/mol]	Carbon / redox	Surface area / redox
Nucleophilic – Anhydrous	$9.140\ 10^{-7}$	1895	527.8	16	0.9 nm^2
Electrophilic – Anhydrous	$2.525\ 10^{-7}$	523	1910.4	130	7 nm^2
Nucleophilic – Aqueous	$1.098\ 10^{-7}$	228	4393.5	337	19 nm^2
Electrophilic – Aqueous	$3.786\ 10^{-8}$	79	12740.9	931	52 nm^2
Nucleophilic – Anhydrous	$9.116\ 10^{-8}$	189	529.2	16	0.8 nm^2
Electrophilic – Anhydrous	$2.654\ 10^{-8}$	55.0	1818.1	123	6 nm^2
Nucleophilic – Aqueous	$1.167\ 10^{-8}$	24.2	4130.8	315	17 nm^2
Electrophilic – Aqueous	$3.978\ 10^{-9}$	8.2	12125.3	980	51 nm^2

We clearly see the difference between the four synthesized materials, from the calculated coverage, based on electrochemical CV. The two materials synthesized from aqueous GO show low coverage, consistent with the indication of low conversion from alcohol to azide as previously determined by XPS. When the anhydrous GO is functionalized through the

electrophilic route a coverage of approximately one functionality per 7 nm^2 is achieved. However, this is much less compared to the material synthesized through the nucleophilic route, which contains a functionality per less than 1 nm^2 of the theoretical surface area.

When running CV at different scan rates (Figure 61) to determine if the electrochemical reaction is surface confined or under diffusion control, as expected we see the system is proven to be surface confined. The peak current plotted versus the scan rate gives clear linear relation (Figure 61C), whereas the peak current plotted versus square root scan rate (Figure 61B) shows systematic parabolic deviation from linearity.
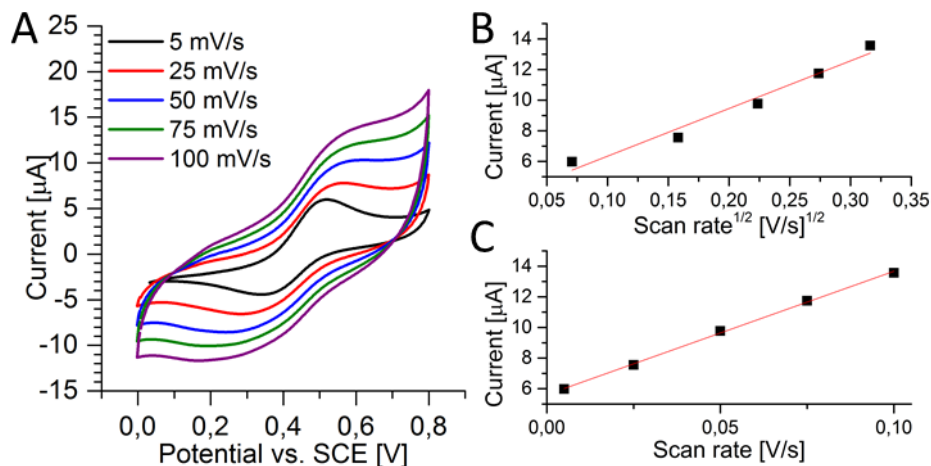
Figure 61: A) CV of 1 µg ferrocene functionalized RGO on GCE (nucleophilic – anhydrous) at different scan rate. B) Peak current vs. scan rate$^{1/2}$ with $r^2 = 0.961$. C) Peak current vs. scan rate with $r^2 = 0.998$.

The ferrocene functionalized RGO shows high redox stability. When a GCE electrode drop cast one µg ferrocene functionalized RGO was cycled in the potential window $0.0 - 0.8$ V vs SCE a total of 2100 cycles, the current drop from the 30th cycle to 2100th cycle is less than 3 %. Even when the electrode was rinsed in water and transferred to fresh electrolyte more that 96 % of the initial signal was retained (Figure 62).
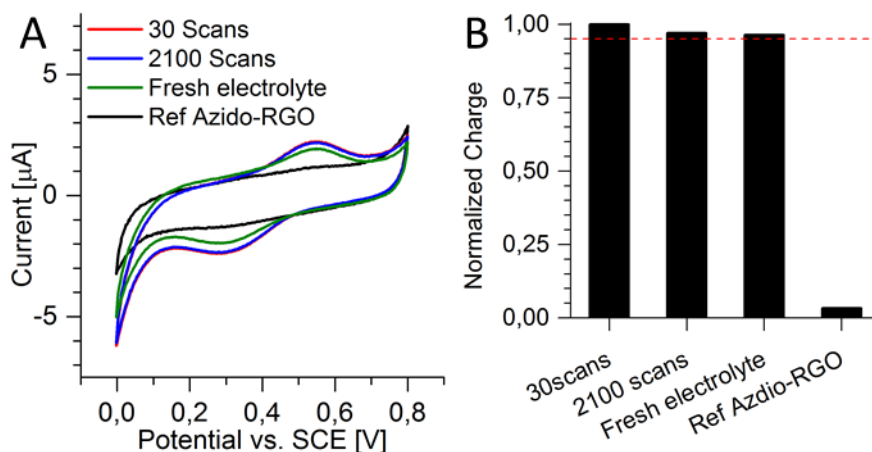
Figure 62: A) CV and B) column diagram of signal for stability test of ferrocene signal from 1 µg ferrocene functionalized RGO on GCE. The electrode was pre-cycled by 30 cycles at 100 mV/s and a CV recorded at 5 mV/s. Then an additional 2070 cycles at 100 mV/s before another CV was recorded at 5 mV/s. Finally, the electrode was removed, rinsed, and inserted into fresh electrolyte. The signal drop from the 30th cycle to 2100th cycles is 2.9% and from the 30th to the final are in fresh electrolyte is 3.7%.

For the better material where anhydrous GO was functionalized through the nucleophilic route, we further studied the effect of film thickness. The film thickness was varied by drop casting different quantities of the material on GCE (1 µg – 0.01 µg). This measurement shows near prefect proportionality between the redox charge and the film mass, showing that redox centres throughout the film, independent of thickness are involved in the electron transfer. This also validates the method of determining coverage as several experiments with different amounts of ferrocene functionalized RGO of the electrode gives a consistent number of redox centres per mass.
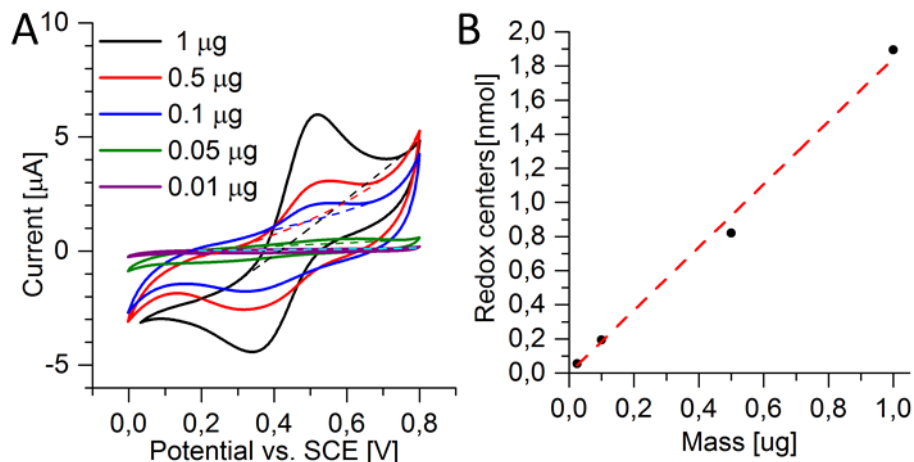
Figure 63: Test of influence of RGO film thickness. A) CV all recorded at 5 mV/s of ferrocene functionalized RGO at varying mass (1 µg – 0.01 µg) on GCE. B) Corresponding oxidation charge vs drop cast mass.

4.5   Conclusion and Outlook

A functional RGO platform for post reduction functionalization through CuAAC was establised and tested by CuAAC coupling of ethynylferrocene as a redox probe. The ferrocene-functionalized RGO was furthered used to evaluate surface coverage electrochemically. The RGO platform consists of RGO sheets decorated by short glycol linkers terminated by azides and attached through two different synthesis pathways; 1) using a combination of nucleophilic ring opening of epoxides and EDC coupling to introduce the glycol linker; which proved significantly better than 2) where the glycol was introduced through use of isocyanate functionalization. In both cases, the azide was introduced using the Mitsonubu reaction. The difference between aqueous and non-aqueous work-up on the GO was tested proving that non-aqueous work-up was vastly superior, mainly due to a much higher conversion yield in the Mitsunobu reaction as determined by XPS.

The reason for this difference is most likely due to very strongly bound water that is near impossible to be completely removed, This residual water can interfere with the phosphine used for the Mitsunobu reaction. The coverage, as determined by electrochemistry, is as high as one ferrocene per $\approx$ 16 RGO sheet carbon atoms or slightly more than one per square nanometer. One problem that was observed was slow electron transfer, which could be improved by using a conductive linker such as a phenyl or other conjugated linker. However, this could also result in high tendency to aggregate. 1,4-diaminobenzene could be used as the phenyl linker. This unit can be introduced just as the glycol. The conversion into azide could

be done through high-yield *in situ* diazotization followed by azidation in the presence of *p*-TsOH, which allows the direct transformation of aromatic amines[263].

$$\text{Ar}\!-\!\text{NH}_2 \xrightarrow[\text{H}_2\text{O / RT / 20-60 min}]{\text{9 eq. NaNO}_2 \text{ / 9 eq. p-TsOH}} \text{Ar}\!-\!\text{N}_2^+\text{TsO}^- \xrightarrow{\text{1.6 eq. NaN}_3 \text{ / H}_2\text{O / RT / <1 min}} \text{Ar}\!-\!\text{N}_3$$
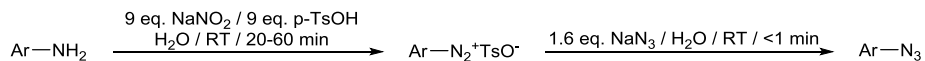
Scheme 10: possible reaction pathway from aromatic amine to aromatic azide[263].

It was also observed from the XPS that considerable amounts of oxygen are not removed during reduction, which could warrant using an even stronger reducing agent. As the synthesis is done in dry THF, stronger reducing agents are available such as; LiAlH$_4$ which has been proven more efficient for GO reduction than hydrazine and NaBH$_4$[264].

Chapter 5   TTF-Calix[4]pyrrole Functionalized RGO for Cl⁻ Sensing

This chapter describes the functionalization of Azido-RGO with an example of a complex synthetic supramolecular receptor tetrakis(tetrathiafulvalene)-calix[4]pyrrole (TTF-Calix[4]pyrrole) derivative synthesis in Prof. Jan O Jeppesens lab at SDU. After functionalization the complex redox system was investigated electrochemically and attempts were made to use the materials for sensing of both Cl⁻ and 1,3,5-trinitrobeneze (TNB) a model compound of TNT.

5.1   Introduction
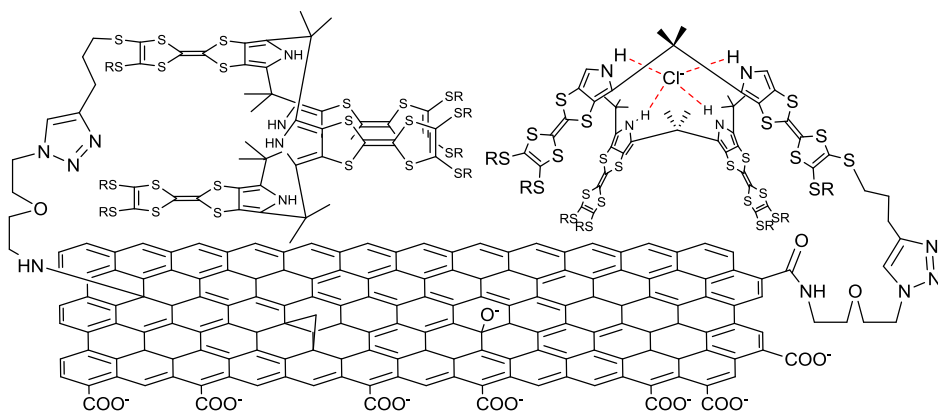
Figure 64: Schematic representation of Azido-RGO platform after functionalization with TTF-calix[4]pyrrole sensor molecules.

The purpose of this work is to demonstrate the feasibility to attach advanced redox active supramolecular chemical sensor molecules (TTF-calix[4]pyrrole) to the Azido-RGO platform synthesized in the previous chapter, generating an active sensing material which can be drop cast onto an electrode (Figure 64). This will significantly reduce the required amount

of active compound needed, as the concentration at the solid/solvent interface can be high without the need for a high bulk concentration. Especially for electrochemically based sensing, this is an optimal solution, as electrochemistry is also confined to electrode/solvent interfaces. This can natably reduce the sensor price because of the high cost of synthetic challenging compounds such as sensor compounds.

Another benefit is that solubility is no longer an issue. The solid interface can be transferred to any solvent without the need for the sensing material to be soluble in that solvent. In this specific case TTF-Calix[4]pyrrole is normally confined to measurements in organic solvents such as MeCN, but it would now be possible to use the compound in aqueous electrolyte.

5.1.1   Tetrathiafulvalene
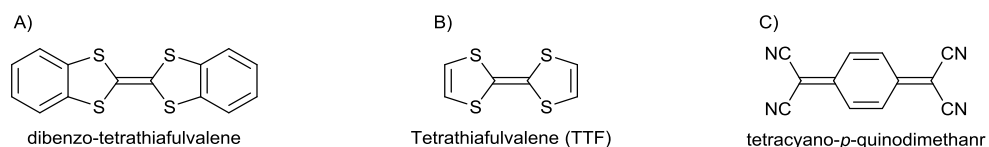
Figure 65: Molecular structure of A) first synthesized TTF derivative B), unmodified TTF, and C) tetracyano-*p*-quinodimethane

The first tetrathiafulvalene (TTF) derivative (Figure 65A) was synthesized by Hurltley and Smiles[265] in 1926. However, the interest in TTF derivatives was only really sparked after Wudl *et. al.*[266,267] investigated and discovered the unique electronic and π-donating properties of TTF in the 1970s. The key properties are strong π-electron donation and reversible oxidation in two steps. At low potentials the first single-electron transfer forms a stable radical cation, followed by another single electron transfer to form a dication (Figure 66).

Later Ferraris *et. al.*[274] found that the characteristic properties of TTF combined with the π-electron acceptor tetracyano-*p*-quinodimethane (Figure 65C) led to the first "organic metal". The implementation of TTF into supramolecular chemistry through the last decades has proven that TTF is useful beyond the field of "organic metals", and has found widespread use with cyclophanes, catenanes, dendrimers, polymers, rotaxanes, artificial photosynthesis systems, sensors etc.[269–273] (Figure 66).
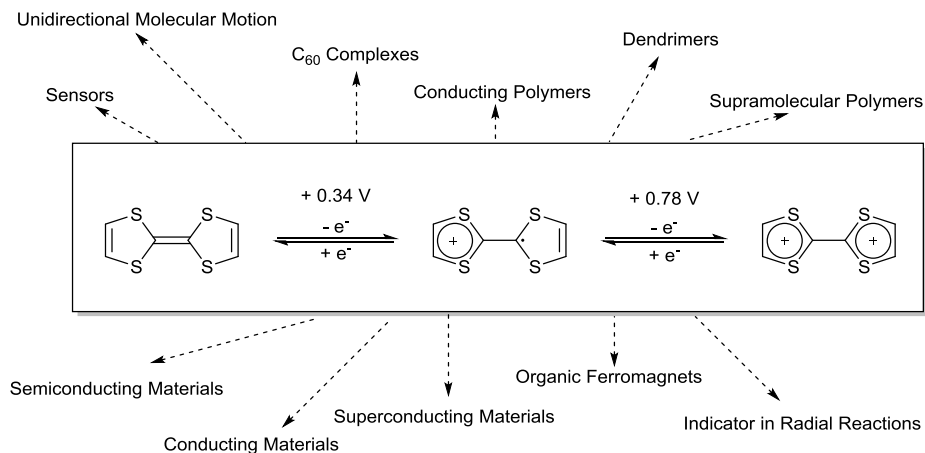
Figure 66: Schematic oxidation reaction of TTF. Potentials given vs. Ag/AgCl in MeCN[268]. In addition, some key areas where TTF is mostly used[269–273].

TTF is a quasi-planar molecule with 14 π-electrons, but lacks cyclic conjugation resulting in non-aromaticity. The easy oxidation is explained by formation of a 5-membered aromatic cyclic conjugated 6 e⁻ π-system upon formation of the radical cation. The second single electron transfer at slightly higher potential also forms an aromatic cyclic conjugated 6 e⁻ π-system in the other ring. The higher potential for this oxidation is due to cationic repulsion destabilizing the system.

5.1.2   Calix[4]pyrrole

The class of Calix[4]pyrroles is a meso-octasubstituted porphyrin system first synthesized by Baeyer in 1886[275] via condensation of pyrrole and acetone in the presence of acid to produce meso-octamethylcalix[4]pyrrole. Initially, calix[4]pyrrole was mainly studied for their weak metal ion binding complexes due to their resemblance to porphyrins[276–278]. Later calix[4]pyrroles gained interest within anion and ion pair binding[279–282] and was re-invented under the name calix[4]pyrroles based on their close resemblance to calixarenes[282]. The resemblance to calixarenes is stronger than to porphyrins because of the partial rotation around the meso carbon between the planar pyrrole units, rendering the structure flexible rather than flat. Calix[4]pyrrole is often thought of as having four discrete conformations cone, partial cone, 1,2-alternate and 1,3-alternate (Figure 67), although an infinite subset of conformations exists between these discrete conformations through the flexibility. Several theoretical studies[283–287] have been carried out and state that the most stable one of the conformations is the 1,3-alternating conformation in both gas phase and solution in a range of different solvents. This is confirmed by X-ray crystallography in solid phase[288]. When

binding anions the conformation is changed to a cone conformation both in solid phase and solution[282].
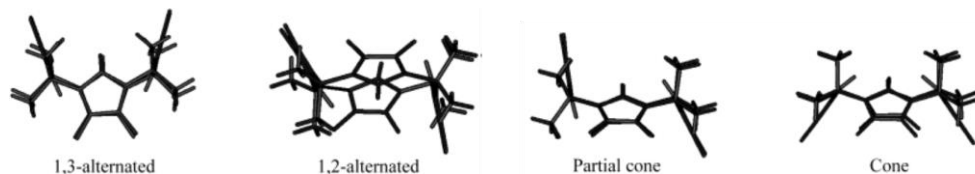
Figure 67: Illustration of the four discrete conformations of calix[4]pyrrole (adapted with permission from ref.[287] Copyright J. Am. Chem. Soc.)

5.1.3 TTF-Calix[4]pyrrole
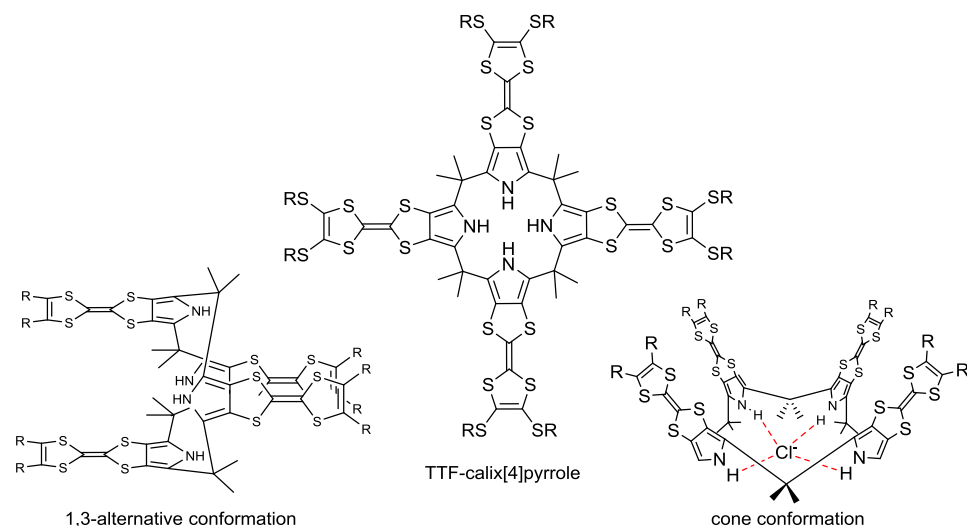
Figure 68: Schematic representation of TTF-calix[4]pyrrole; 1,3-alternative conformation (left); 2D projection (middle); cone conformation (right).

Based on the anion binding properties of calix[4]pyrrole and the electronic properties of TTF, K. Nielsen *et. al.*[289–291] designed a anion sensor using calix[4]pyrrole as a receptor unit and TTF as a transducer, as anion complexation would stabilize the oxidized form of TTF and reduce the redox potential. The binding constant of the calix[4]pyrrole towards Cl$^-$ was increased several orders of magnitude by attaching the TTF units, and binding of Cl$^-$ indeed alters the redox potential (Figure 69). However, it should be noted that this is a highly complex redox system, as it contains four TTF units each theoretically capable of two single electron transfers. Even though these redox units are not conjugated when one is oxidised, they can affect each other due to destabilization of multiple spatially confined cations.
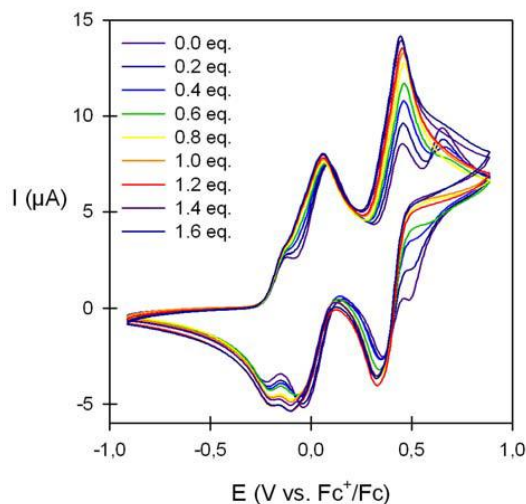
Figure 69: CVs of receptor TTF-calix[4]pyrrole (0.25 mM) titrated with TBACl (0 – 1.6 eq.) in TBAPF₆/CH₂ClCH₂Cl (adapted with permission from ref.[290] **Copyright J. Am. Chem. Soc.).**

TTF-calix[4]pyrrole also functions as a host for electron deficient quasi-planar molecules e.g. nitro-aromatic explosives[289] in the 1,3-alternating conformation. Two identical binding sites are available with two possible hydrogen bond interactions with calix[4]pyrrole NH as donor and CT interaction between TTF and electron deficient π-systems. The binding properties for electron deficient quasi-planar molecules are only available in the absence of complexing anions, as anion binding induces the cone conformation and is significantly stronger. Furthermore, the binding of neutral quasi-planar molecules is cooperative both because binding of the first guest stabilizes the dynamic receptor in the 1,3-alternating conformation, and because of a synergistic effect between binding interactions. Hydrogen bonding draws electrons out of the guest improving the CT interaction in the opposite site, and the CT interaction pulls electrons away from the pyrrole ring making it a better hydrogen bond donor for the guest in the opposite site (Figure 70).
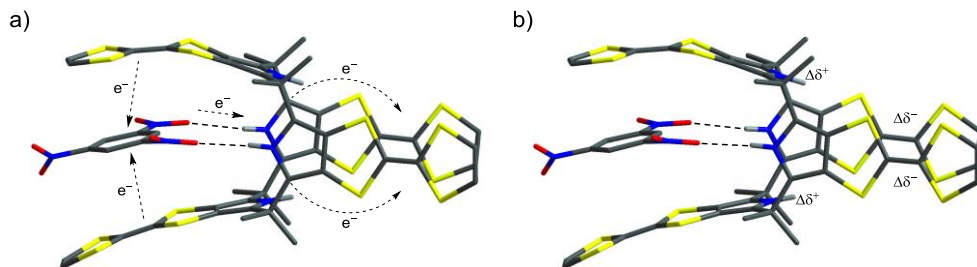
Figure 70: Illustration of binding of electron accepting quasi-planar neutral molecules in TTF-calix[4]pyrrole. Illustrating of how binding of TNB in the first binding pocket changes the partial charges in the second pocket thereby increases binding strength.

5.2   Synthesis

5.2.1   Synthesis of TTF-Calix[4]pyrrole Derivatives
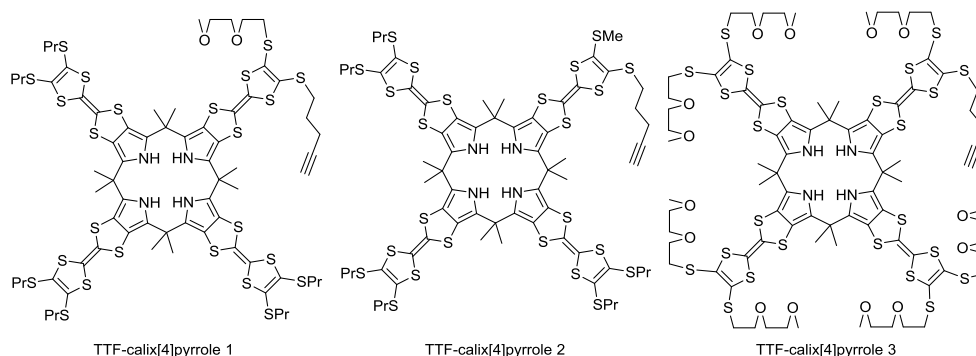
Figure 71: schematic representation of the three TTF-calix[4]pyrrole derivatives synthesized in Prof. Jan O. Jeppesen lab at SDU used in this project.

Three TTF-calix[4]pyrrole derivatives (Figure 71) were synthesized in Prof. Jan O. Jeppesen lab at SDU and provided for attachment onto Azido-RGO. TTF-calix[4]pyrrole 1 was synthesised by M.Sc. Lars H. Pedersen in 2011 stored at −18 °C until use in 2016. The other two TTF-calix[4]pyrroles 2 and 3 were synthesized by B.Sc. Simon Pedersen in 2015-16 and stored at −18°C.

The TTF-calix[4]pyrrole derivatives were synthesized in a templated asymmetric macrocyclization between 2 different monopyrrolotetrathiafulvalenes, in order to produce TTF-calix[4]pyrrole with a single terminal alkyne, which can be used for attachment to Azido-RGO. The template used is Cl⁻ in the form of tetrabutylammonium chloride (TBACl). This helps to promote the formation of calix[4]pyrrole rather than bigger macrocycles or polymeric chains, pre-organizing reactants to form calix[4]pyrrole because of the strong

complexation between calix[4]pyrrole and Cl⁻. High dilution is employed for the same purpose. Apart from the terminal alkyne for CuAAC reaction, the TTF-calix[4]pyrrole contains seven other terminal groups. In TTF-calix[4]pyrrole 1 the one connected to the same TTF as the terminal alkyne is a short glycol chain. TTF-calix[4]pyrrole 2 and 3 were synthesised with a methyl group instead of this short glycol linker, in order to reduce the bulkiness near the terminal alkyne, and leaving more room for catalytic complexing during CuAAC coupling. The six other terminal groups' primary function is to increase solubility. For TTF-calix[4]pyrrole 1 and 2 these are propyl groups helping solubility in the organic solvents usually used for synthesis and measurements of TTF-calix[4]pyrroles. TTF-calix[4]pyrrole 3 was synthesized with these short glycol chains instead of the six propyl groups to improve interaction with more polar solvents such as water.
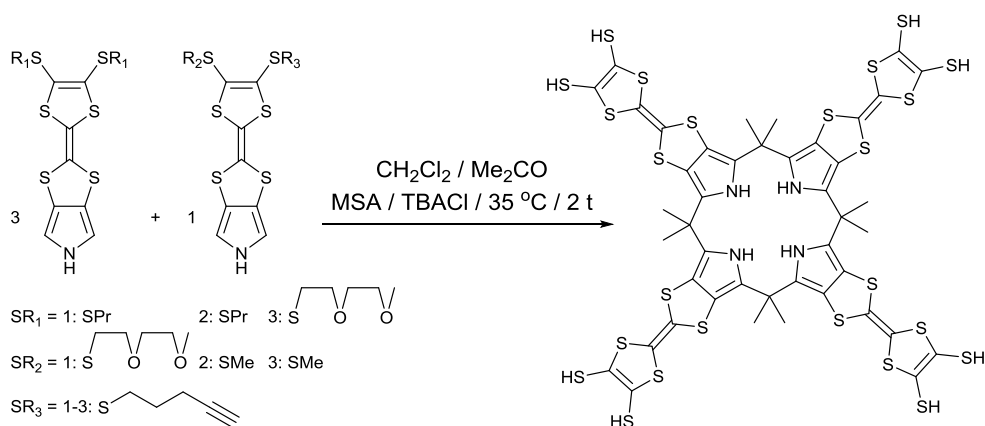
Figure 72: Reaction scheme of synthesis of TTF-calix[4]pyrroles

5.2.2 CuAAC Coupling of TTF-Calix[4]pyrrole on Azido-RGO
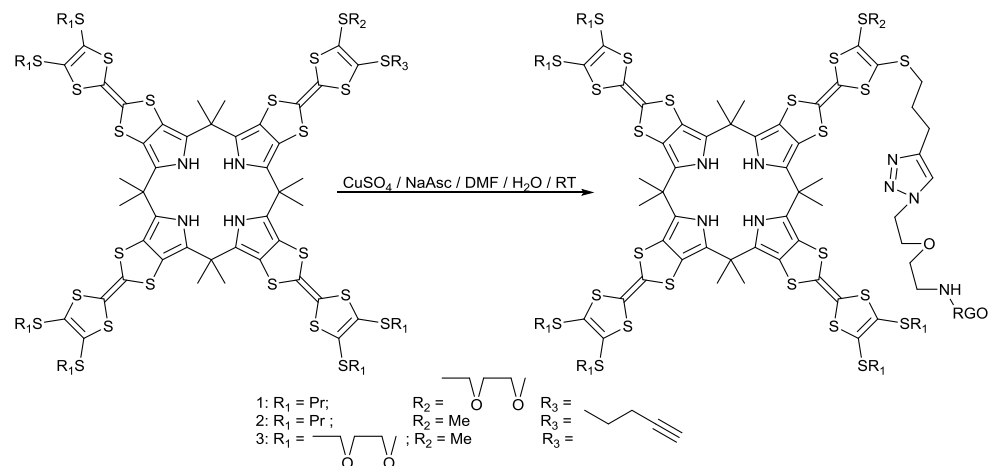
Figure 73: Reaction scheme of CuAAC between Azido-RGO and TTF-calix[4]pyrrole

TTF-calix[4]pyrrole (1 – 3) was attached to the azido-RGO platform through CuAAC reaction, using the azido-RGO which proved best in Chapter 4 (synthesized by nucleophilic approach from anhydrous GO). A mixture of DMF and H_2O (3:2) was used as solvent and *in situ* generated Cu(I) as catalyst. The resulting TTF-calix[4]pyrrole functionalized graphene like materials, henceforth called RGO-calix 1 – 3, were purified by repeated washing with DMF and H_2O before being dialyzed (full experimental section 7.1.15 page 113).

5.3 Characterization

5.3.1 XPS Characterization

The three synthesized RGO-calix materials as well as TTF-calix[4]pyrrole 2 (as reference compound) were characterized by XPS. The high content of sulphur atoms in the TTF-calix system presents a unique opportunity for characterization by the XPS – S2p spectrum. The reference, pure calix system shows a clear 1:2 (8:16) ratio between peaks at 163.8 eV and 165.1 eV. The 163.8 eV peak intensity 1 can be assigned to the 8 thiol sulphur atoms, and the 165.1 eV peak intensity 2 to the 16 fulvalene sulphur atoms. The same 1:2 peak ratio is found in all three RGO-calix materials, giving evidence of the incorporation of TTF-calix[4]pyrroles.
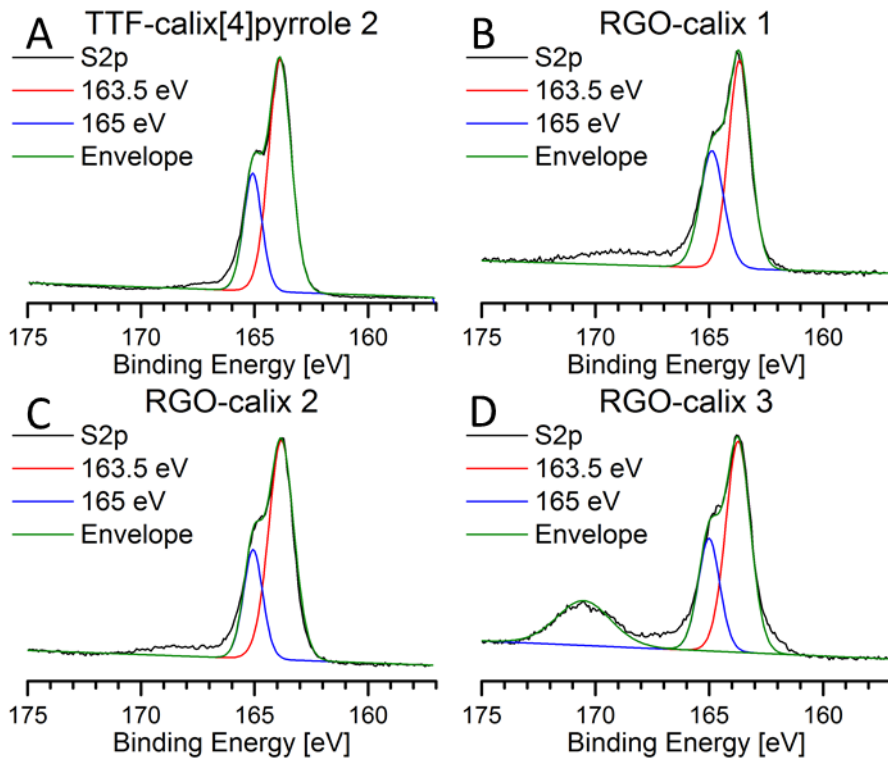
Figure 74: XPS – S2p spectra of A) TTF-calix[4]pyrrole; B) RGO-calix 1; C) RGO-calix 2; D) RGO-calix 3.

The introduction of sulphur can also be used to quantify the extent of functionalization using the atomic percentage of sulphur as determined by XPS-survey (Figure 75) to calculate the contribution from the functionality as in Chapter 3 for the crown-ether (section 3.2.5 page 38). By subtracting this from the total, the contribution from the graphene-like nanosheets can be determined and by extension the number of carbons per introduced calix functionality Using the theoretical surface area per carbon (5.246 Å^2), an estimate of the area of nanosheet available per calix molecule can also be determined.
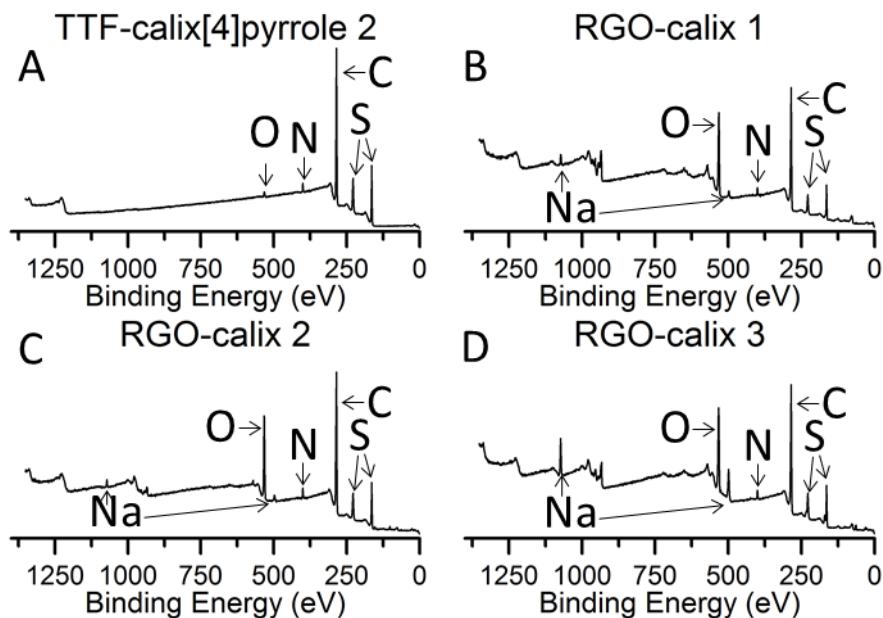
Figure 75: XPS – Survey spectra of A) TTF-calix[4]pyrrole; B) RGO-calix 1; C) RGO-calix 2; D) RGO-calix 3.

Table 12: Elemental composition as determined by XPS, as well as calculated contribution from functional moiety and RGO sheet; calculated C:O ratio and carbon per functional moiety.

	% C	% O	% N	%S	Other elements	C : O	C : Func.
TTF-calix[4]pyrrole 2	71.5	–	3.9	24.6	O	–	–
Theoretical	70.8	–	4.2	25	–	–	–
RGO-calix 1	72.1	10.3	5.8	11.8	Na	–	–
$C_{76}H_{97}N_8O_3S_{24}{}^{\bullet}$	37.4	1.5	3.9	11.8	–	–	–
Sheet	34.7	8.8	1.8	–	–	3.9	71
RGO-calix 2	72.5	8.7	5.7	13.1	Na	–	–
$C_{72}H_{89}N_8OS_{24}{}^{\bullet}$	39.3	0.5	4.4	13.1	–	–	–
Sheet	33.2	8.2	1.3	–	–	4.1	61
RGO-calix 3	69.5	13.3	5.6	11.6	Na	–	–
$C_{84}H_{113}N_8O_{13}S_{24}{}^{\bullet}$	40.6	6.3	3.9	11.6	–	–	–
Sheet	28.9	7.0	1.7	–	–	4.1	60

The measured elemental compositions of TTF-calix[4]pyrrole 2 ($C_{68}H_{80}N_4S_{24}$) match fairly accurately the theoretical atomic composition (Table 12): experimental (C: 71.5 S: 24.6 N: 3.9) theoretical (C: 70.8 S: 25.0 N: 4.2). The calculations based on sulphur content (Table 12) show that one TTF-calix[4]pyrrole is attached per ≈ 70 carbon atoms for RGO-calix 1 or what amounts to ≈ 3.7 nm^2. This is a slightly lower coverage than RGO-calix 2 and 3 with one TTF-calix[4]pyrrole attached per ≈ 60 carbon atoms or what amounts to ≈ 3.1 nm^2. In comparison, the core of the TTF-calix[4]pyrrole measures approximately 1×1×2 nm not including sidechains. These calculations also indicate that not all nitrogen functionalities are part of the TTF-calix[4]pyrrole attachments (including linker), or that more azide groups are available with the excess of TTF-calix[4]pyrrole used during synthesis. It seems that the reason why the RGO is not more functionalized is sterically limitations. Unfortunately, the resolution of the N1s spectra is not sufficient to be deconvoluted, and it is therefore not possible to determine if more azide groups are present.
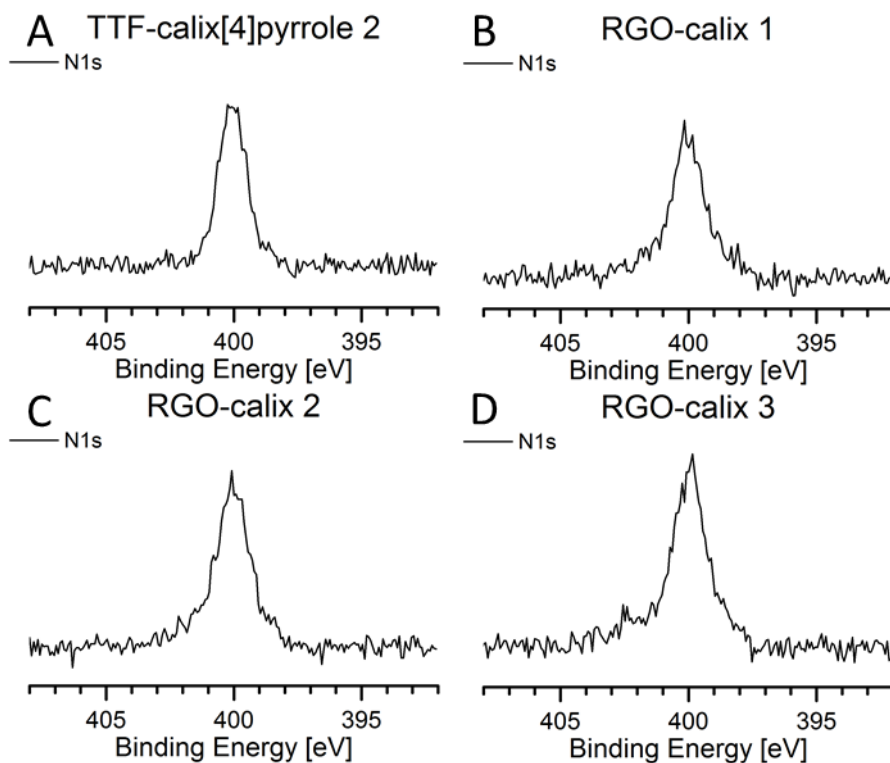
Figure 76: XPS – N1S spectra of A) TTF-calix[4]pyrrole; B) RGO-calix 1; C) RGO-calix 2; D) RGO-calix 3.

The C:O ratio in the RGO sheet seems to have gone down slightly from 5.2 to ≈ 4.1 compared to the starting material Azido-RGO. This is strange as additional reductant sodium ascorbate was used during synthesis. The C1s deconvoluted data are dominated by the sp^2 C–C peak at

248.8 eV. However, this is slightly misleading as a large percentage of the carbon comes from the TTF-calix[4]pyrrole system.
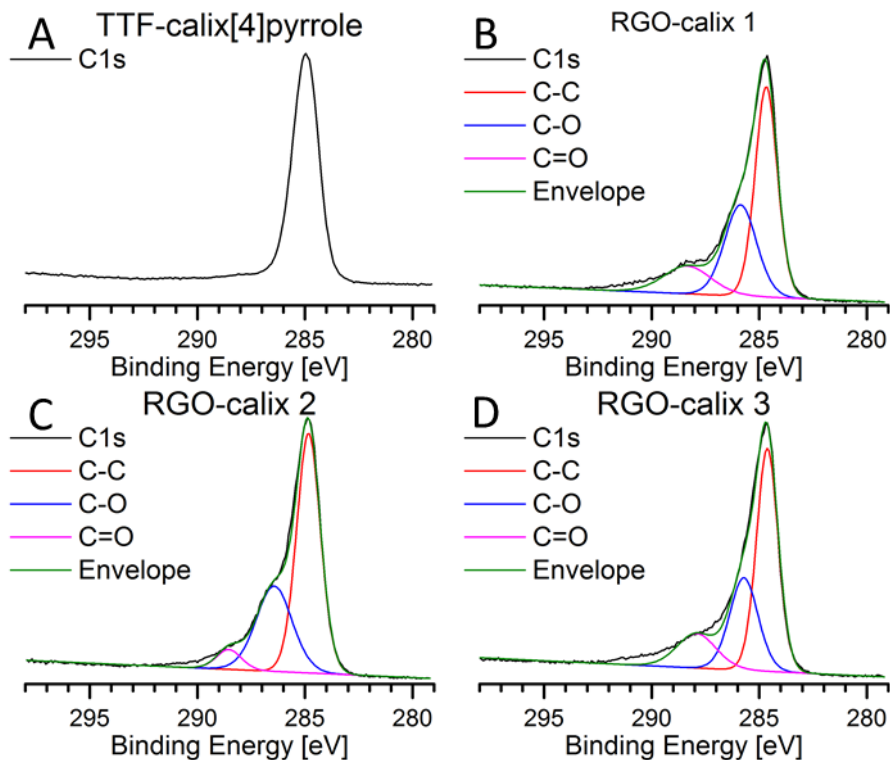
Figure 77: XPS – N1S spectra of A) TTF-calix[4]pyrrole; B) RGO-calix 1; C) RGO-calix 2; D) RGO-calix 3.

Table 13: Data from the deconvoluted XPS-C1s spectra with relative C–C, C–O, C=O content.

	C–C ≈ 284.8 eV	C–O ≈ 286 eV	C=O ≈ 288.5 eV
TTF-calix[4]pyrrole 2	100	0	0
RGO-calix 1	64.1	27.6	8.3
RGO-calix 2	74.1	20.7	5.2
RGO-calix 3	63.7	226.7	9.6

5.3.2   IR Spectroscopy

Due to the high coverage and size of the attached TTF-calix[4]pyrroles, the attachment dominates the IR spectra of the RGO-calix 1-3 materials, resulting in high resemblance between the RGO-calix and its respective TTF-calix[4]pyrrole, with several core fundamental vibration overlapping (Figure 78, 79 & 80). These overlapping fundamental

vibrations include: Pyrrole N–H stretch at ≈ 3400 cm^{-1}; three different C–H stretch vibrations at ≈ 2960 cm^{-1}, ≈ 2920 cm^{-1} & ≈ 1860 cm^{-1}; further, aromatic C=C stretch at ≈ 1650 cm^{-1} & ≈ 1560 cm^{-1}; S–CH$_3$/S–CH$_2$ bend at ≈ 1450 cm^{-1} and ≈ 1240 cm^{-1}; meso-CH$_3$ at ≈ 1360 cm^{-1}. Additional C–O stretch are observed at ≈ 1090 cm^{-1} for RGO-calix 1 and especially RGO-calix 3. Together with the XPS data this is strong evidence for successful functionalization of Azido-RGO. Within the three TTF-calix[4]pyrroles a slightly higher coverage is achieved with TTF-calix[4]pyrrole 2 and 3 possibly due to the reduced bulkiness around the terminal alkyne.
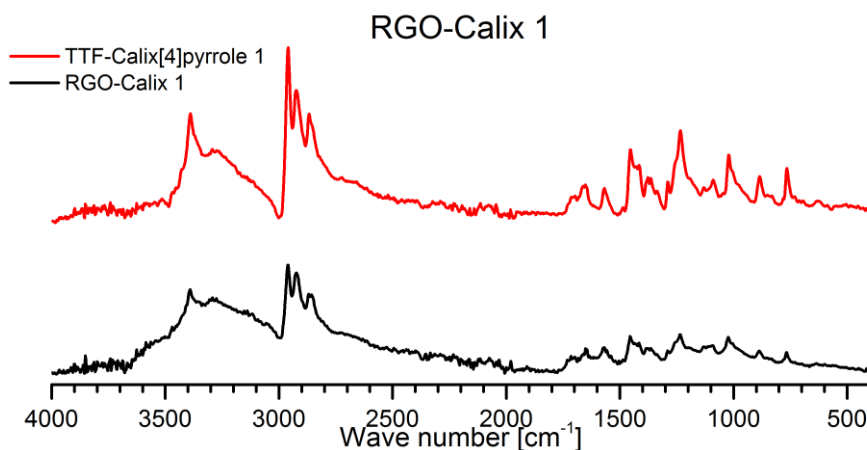
Figure 78: ATR-FTIR spectra of RGO-calix 1 (black) and TTF-calix[4]pyrrole 1
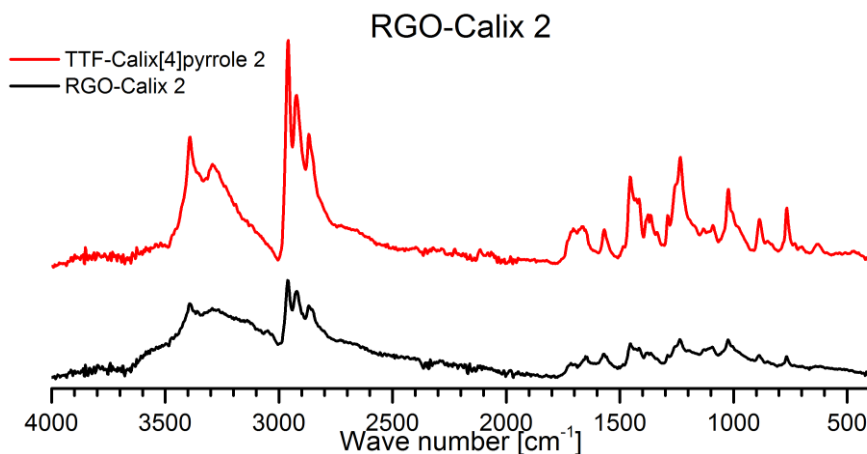
Figure 79: ATR-FTIR spectra of RGO-calix 2 (black) and TTF-calix[4]pyrrole 2
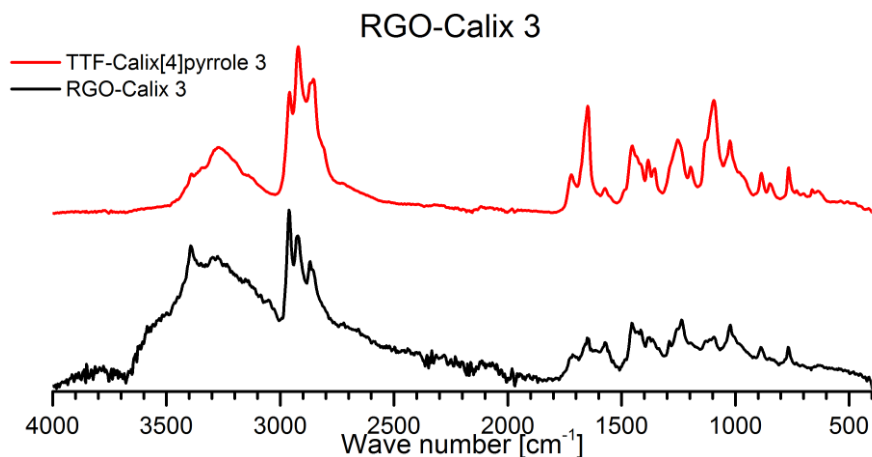
Figure 80: ATR-FTIR spectra of RGO-calix 3 (black) and TTF-calix[4]pyrrole 3

5.4 Electrochemical Measurements

Functionalized GCEs were prepared by drop casting 10 µL of aqueous dispersions of TTF-calix[4]pyrrole functionalized RGOs onto freshly polished 7 mm^2 GCEs and dried *in vacuo* for 1 hr. These functionalised electrodes were tested in a three-compartment electrochemical cell, with the functionalized GCE as working electrode, freshly burned coiled Pt-wire as counter electrode and SCE as reference electrode, under Ar atmosphere, in an aqueous electrolyte solution of 0.1 M KPF$_6$. KPF$_6$ was chosen as electrolyte because PF$_6^-$ is a big anion that does not complex to TTF-calix[4]pyrrole and therefore does not interfere with the sensing studies.

5.4.1 Investigation of RGO- Calix Redox Activity

CV of GCE functionalized with 1 µg RGO-calix 3 was recorded at 5 mV/s in the potential range from −0.75 to 1.75 V. Two oxidation peaks were observed, although only barely separated, at 0.875 V and 1.15 V. The two reductions peaks are located at 0.1V and 0.4 V. When limiting the potential window to only the oxidation region from 0 to 1.75 V), we see the oxidation peak in the first cycle, but no oxidation in subsequent scans. If we limit the potential window to the reduction region from 0 to −0.75 V, we see the reduction peak in the first scan, but not in subsequent scans. This confirms that the redox peaks, despite being far removed, belong to the same redox species.
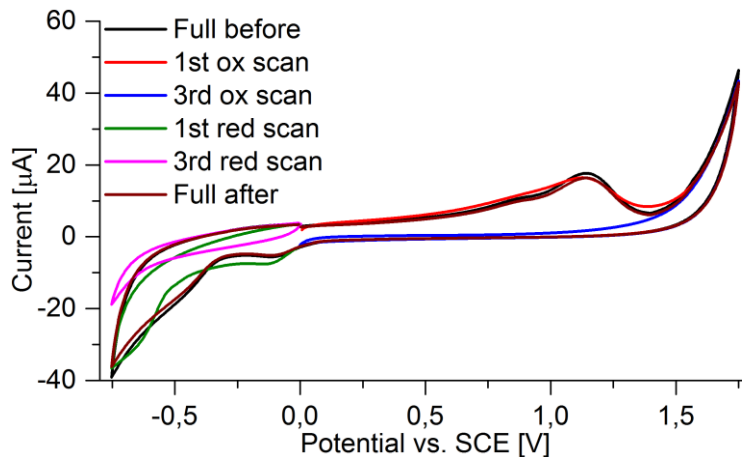
Figure 81: CV of GCE functionalized with 1 µg RGO-calix 3 recorded at 5 mV/s starting at 0.0 V vs. SCE. First full potential window (−0.75 – 1.75 V vs. SCE) (black) then only the oxidative region (0.0 – 1.75 V vs. SCE) first scan (red) subsequent scan (3rd shown blue) then only reductive region (−0.75 – 0.75 V vs. SCE) first scan (green) subsequent scans (3rd shown magenta) finally full window again (−0.75 – 1.75 V vs. SCE) (brown).

The exact reason for the large peak separation for the TTF/TTF$^{\bullet+}$ redox process is unknown, but it can be speculated that the radical cation of the TTF-units could be stabilized by the RGO sheet or possibly react with RGO to form a more stable intermediate which is more difficult to reduce.

In order to prove that the redox peak shown is related to the surface confined TTF-calix[4]pyrrole, CV was recorded at different scan rates. The potential of the oxidation peak is shifted to higher potentials even at low scan rate (75 mVs). Instead the reduction peak, specifically the one at −0.4 V vs. SCE, was used to plot peak current vs scan rate and vs square root of scan rate. As expected this shows that the system is not under diffusion control but surface confined as a good linearity is seen in the plot of current vs scan rate, but clear parabolic deviation is seen from plot vs square root of scan rate (Figure 82 and Figure 83).
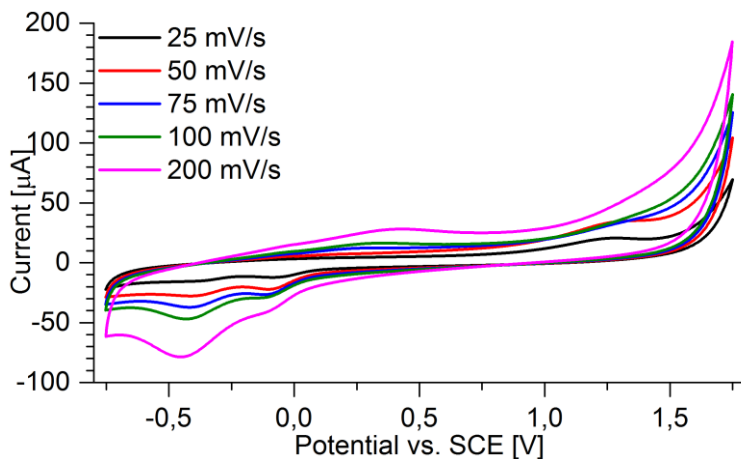
Figure 82: CV of GCE functionalized with 1 µg RGO-calix 3 recorded at different scan rate (25 – 200 mV/s in the potential window (−0.75 – 1.75 V vs. SCE).
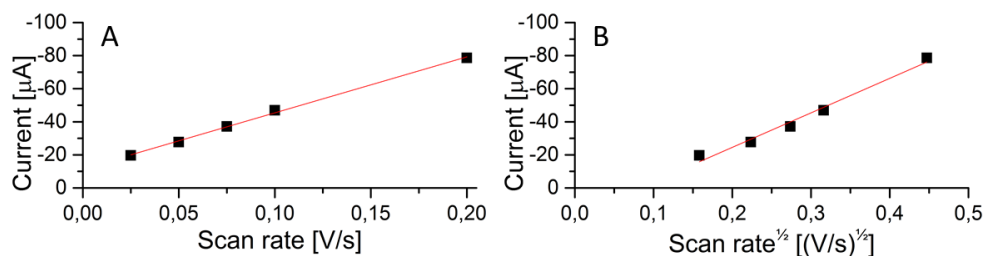
Figure 83: Plot of peak current vs A) scan rate; r² =0.998 B) square root of scan rate r²=0.977.

These data can be explained with the system described by K. Nielsen *et. al.*[290] where a similar TTF-calix[4pyrrole in a solution of TBAPF$_6$/CH$_2$ClCH$_2$Cl was investigated (Figure 84). Here four redox peaks were observed, at ≈ −0.17, 0.11, 0.38 and 0.61 V. The separation between peak 1 and 3 as well as between peak 2 and 4 is ≈ 0.5V, consistent with the separation of the redox potentials of TTF/TTF$^{•+}$ and TTF$^{•+}$/TTF^{2+}. It therefore seems that the first two redox peaks originate from the oxidation of the four TTF units to TTF$^{•+}$, and the subsequent two peaks for the further oxidation to TTF^{2+}. From the peak area of peak 1 and 2 an approximately 1:3 ratio is observed, leading to the assumption that oxidation of the first of the four TTF units is more facile than oxidation the others. This can be explained by one of the four units binding to the electrode, while the others are geometrically prevented from direct binding.
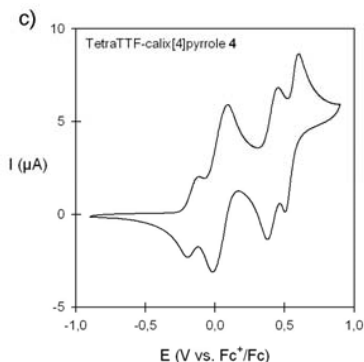
Figure 84: CVs (0.25 mM) recorded in n-Bu$_4$NPF$_6$/CH$_2$ClCH$_2$Cl of receptor 4, e. i. TTF-calix[4]pyrrole derivative. (Reproduced with permission from SI of ref[290], Copyright American Chemical Society).

Returning to our system we see a similar situation with a small peak preceding a larger peak separated by the same ≈ 0.275V consistent with one of the four TTF units first being oxidized to TTF$^{•+}$ before the other three (Figure 81). We do not see the full oxidation TTF^{2+} because this happens at a too high potential. From this we can assume that the oxidation peak we see is caused by 4 e$^-$ oxidation, one for each of the four TTF units. Thus, we can calculated the coverage similar the way it was done in chapter 4.
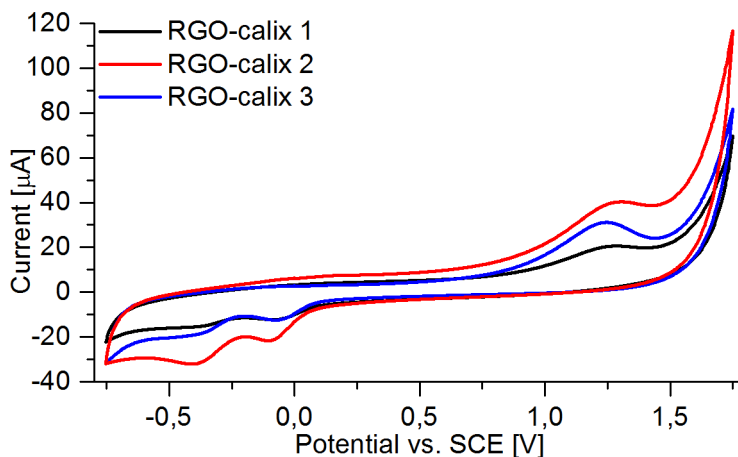
Figure 85: CV of functionalized GCE electrodes loaded with 1 µg of each of the RGO-calix (1 – 3) in the potential range −0.75 – 1.75 V vs. SCE at 25 mV/s.

CV of functionalized GCE electrodes loaded with 1µg of each of the RGO-calix (1 – 3) was recorded in the potential range −0.75 – 1.75 V vs. SCE at 25 mV/s (Figure 85). The charge associated with the broad oxidation peak at 1.25 V vs. SCE was determined and used to

determine the coverage of the materials under the assumption that 4 electrons are involved in this oxidation process, as they was done in chapter 4 (section 4.4.2 page 75).

Sample	Charge [C]	n_{e^-} [pmol]	n_{calix} [pmol]	Mw$_{redox}$ [g/mol]	Mw$_{calix}$ [g/mol]	Mw$_{sheet}$ [g/mol]	C / calix
RGO-calix 1	5.258 10^{-4}	0.545	0.136	7340	1940.1	5400	450
RGO-calix 2	1.532 10^{-4}	1.588	0.397	2519	1852.0	667	56
RGO-calix 3	1.351 10^{-4}	1.399	0.350	2857	2212.3	645	54

Table 14: Coverage of calix[4]pyrrole on RGO-sheet based on charge determined by CV.

The coverage of TTF-calix4]pyrrole in RGO-calix 2 and 3 calculated from CV data is remarkable consistent with those calculated with XPS. The significantly lower charge produced in case of RGO-calix converts to a significantly different result than that determined by XPS. The reason for this is presently unknown.

5.4.2 Sensing Properties of RGO-calix-3

Sensing studies weere only carried out on RGO-calix 3, due to severe time limitation at this stage of the project. GCE functionalized by drop casting 1 µg of RGO-calix 3 was used in experiments with Cl$^-$ titration recording CV in potential range from −0.75 to +1.75 V vs. SCE at 25 mV/s (Figure 86). This resulted in an interesting change of the reduction peaks at ≈ 0.1 & 0.4 V vs. SCE.
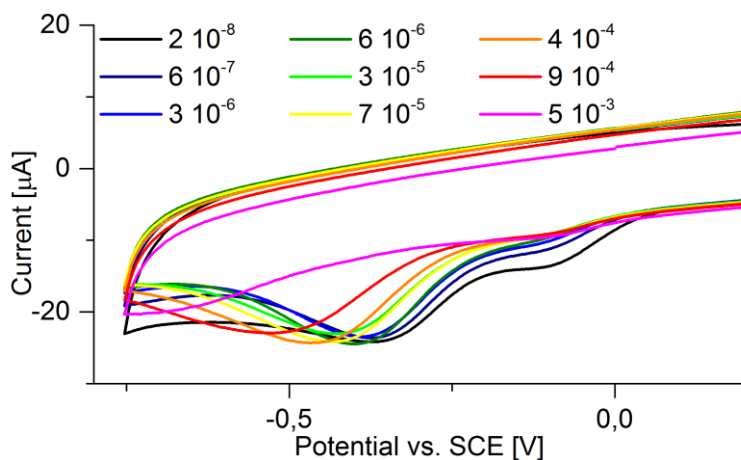
Figure 86: CV based titration with KCl ($2 \times 10^{-8} – 5 \times 10^{-3}$) of GCE functionalized by drop casting with 1 µg of RGO-calix 3 in 0.1 M KPF$_6$ electrolyte with potential range −0.75 – 1.75 V vs. SCE at 25 mV/s.

Upon addition of minute amounts ($[Cl^-] \approx 10^{-7}$) of Cl^- the peak at 0.1 V disappears and is incorporated into the 0.4 V peak. This peak is also shifted toward lower reduction potential as Cl^- is added (Figure 86). As explained above, the splitting of the two reduction peaks is assumed to be a result of asymmetric binding to the electrode surface. Upon addition of Cl^- the receptor presumably assumes a cone conformation rather than 1,3-alternating conformation which could explain why the reduction peak is no longer split into two different peaks. As the TTF-calix[4]pyrrole binds Cl^-, the redox potential is shifted to more negative values as seen for the system described by K. Nielsen *et. al.*[290]
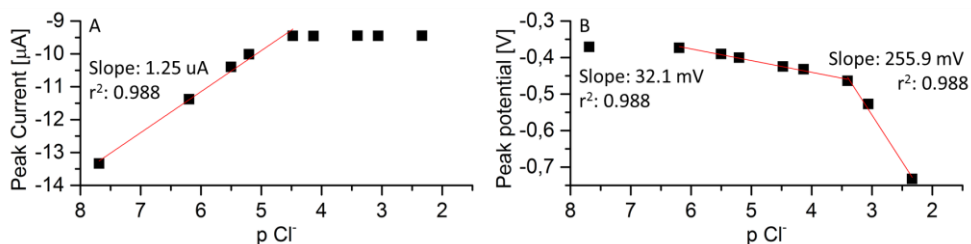
Figure 87: Plotted voltammetric peek current changes vs Cl^- concentration. A) Peak current of peak initially at 0.1 V vs. pCl⁻. B) Peak potential of peak initially at ≈ 0.4 V vs. pCl⁻.

A linear response is seen in the concentration range $10^{-8} - 10^{-5}$ M when plotting the peak current vs. pCl⁻ (Figure 87A), with a sensitivity of 1.25 μA per decade of Cl^- concentration. When plotting the reduction potential vs. pCl⁻ (Figure 87B) we first see a moderate decrease in reduction potential of ≈ 32 mV per decade of Cl^- concentration in the concentration range $10^{-7} - 10^{-4}$ M. At further addition a major shift of 250 mV per decade Cl^- concentration occurs in the concentration range $10^{-4} - 10^{-2}$ M. The initial potential shift seems to accord with what was reported by K. Nielsen *et al.*[290] but the potential shift at mM concentration seems too large to be cause by redox potential reduction due to guest binding and some other unknown mechanism seems to be at play here. Unfortunately, there was not enough time to investigate this further.

5.5   Conclusion

The functionalization of Azido-RGO with the sensing molecule TTF-calix[4]pyrrole was successfully achieved by CuAAC reaction, and verified by IR spectroscopy and XPS. The coverage was determined independently by XPS and electrochemistry for two of the three TTF-calix[4]pyrroles addressed. The electrochemical determination for the third was significantly lower than the XPS determination for reasons unknown. The coverage which could be determined was one functionality per $\approx 50 - 60$ carbon atoms. Considering the size of this functionality this is a high coverage. Due to time limitation at the end of the project, only one of the sensing materials was tested in sensing studies, and only for Cl^- the stronger binding of the possible guests for TTF-calix[4]pyrroles and not for TNB. The material RGO-calix 3 proved highly sensitive towards Cl^- with linear response of the reduction of the peak current for the reduction peaks at -0.1 V by 1.25 µA per decade in the Cl^- concentration range $10^{-8} - 10^{-5}$ M.

Interestingly, Cl^- also induced a shift of the reduction potential of the second peak at (≈ -0.4 V) at low concentration with a moderate shift, but a very significant shift is seen for higher concentration. This shift is presumed to follow another mechanism, due to the magnitude of the shift. Unfortunately, time limitation has prevented further studies of this as well as from studying the selectivity.

Chapter 6   Summary and Conclusion

In this thesis, reduced graphene oxide (RGO) functionalized with supramolecular moieties was synthesized in order to obtain active sensing materials. Combining the valuable properties of graphene-like materials, such as high surface area, high conductivity and low production cost with easy up-scaling, and the versatile and favourable receptor properties of supramolecular moieties, were the overarching objectives of the project.

These chemically modified RGO materials were obtained through one of two core strategies. In the first strategy graphite is oxidized and exfoliated to graphene (GO), which can be functionalized straight forwardly, through nucleophilic ring opening of surface epoxide groups to achieve functionalized GO. The functionalized GO was then reduced to the desired chemically modified RGO.

This approach was used to produce RGO nanosheets functionalized with crown-ether derivatives. A coverage of one crown-ether per 46 RGO-sheet carbon atoms was achieved for a 18-crown[6]ether derivative (RGO-crown[6]). This corresponds to an average coverage of 34 % of the theoretically available surface area. RGO-crown[6] was used for potentiometric sensing using both glassy carbon electrodes and disposable screen-printed electrodes. A detection limit of 10^{-5} M, selective to K^+ over all tested alkali and earth alkaline ions up to concentrations of 2.5×10^{-2} M was achieved. In a similar fashion 15-crown[5]ether (RGO-crown[5]) and 12-crown[4]ether (RGO-crown[4]) derivatives were attached to RGO nanosheets. Similar levels of functionalization to that of RGO-crown[6] were achieved: one molecular unit per 48 carbon atoms for RGO-crown[5], amounting to a 24 % of theoretical surface coverage, and one unit per 52 carbon atoms for RGO-crown[4], amounting to 17 % of the theoretical surface coverage. When these two materials were used to form sensing devices they show selectivity towards Na^+ for RGO-crown[5] and Li^+ for RGO-crown[4] with similar detection limits to that of RGO-crown[6], however, some interference from K^+ was evident.

The first approach to synthesis of chemically modified RGO, however, is apply only to supramolecular moieties that are not subjected to chemical reduction. In order to widen the possibilities of functionalization to include less chemically stable moieties, as an alternative

strategy azido-RGO was developed. Azido-RGO a material that allow to high yield functionalization of already RGO. This was achieved by functionalizing GO with a short linker containing terminal alcohol. The functionalized GO was then reduced efficiently, and the alcohol substituted with an azido-functionality. The produced material could then be functionalized by post-reduction with any moiety containing a terminal alkyne. The incorporation of azide was confirmed by both XPS and IR spectroscopy.

The coverage of azide in the as-synthesized azido-RGO was determined by functionalization with ferrocene as a redox probe, using the azido-functionalities in CuAAC reaction with ethynylferrocene. After functionalization the charge determined from electro-oxidation of the redox probe was determined by CV. From this charge it could be estimated that one ferrocene or azido-functionality was present per 16 carbon atoms of the RGO-sheet. This value translates into slightly more than one ferrocene or azide per nm^2.

The Azido-RGO was further used to attach the sensing molecule TTF-calix[4]pyrrole. Functionalization with this moiety was confirmed by both IR spectroscopy and XPS. The coverage was further determined independently by XPS and electrochemistry to one TTF-calix[4]pyrrole moiety per $\approx 50 - 60$ carbons amounting to one moiety per ≈ 3 nm^2. Given the size of this receptor moiety, the coverage is very high. This material proved to bind and detect Cl^- in aqueous solution at concentrations as low as 10^{-8} M. Azido-RGO could well prove to become a key building block in joining supramolecular-based sensors and graphene-like materials, a key benefit being confining these high-cost receptors to the electrode surface strongly reducing the amount needed for highly sensitive and selective sensing.

Chapter 7   Experimental Procedures

This chapter contains the detailed experimental procedures of the work described in this thesis.

7.1   Synthesis Procedures

All chemicals were purchased through Sigma-Aldrich as synthetic grade or higher and used as received, with the exception of CH_2Cl_2, which was distilled immediately prior to use; anhydrous THF, and DFM, which was dried on a PureSolv; H_2O, which was purified with a Milli-Q ultra-pure system ($18.2\ M\Omega\ cm$). All synthesis experiments using anhydrous solvents were performed in Ar atmosphere with $15 - 30$ min degassing of the solvent prior to experiment. Analytical thin-layer chromatography (TLC) was performed using alumina sheets pre-coated with silica gel 60F (Merck 5554), which were inspected by UV-light (254 nm) prior to development with $KMnO_4$ $_{(aq\ ph\approx12)}$ and heated with a heat-gun. NMR spectra were recorded on a Bruker AVANCE III 400 MHz Spectrometer, where ^{1}H-NMR spectra were recorded at 400 MHz at 298 K, and ^{13}C-NMR at 100 MHz at 298 K. The NMR samples were dissolved in $CDCl_3$ 99.8 % D from Sigma-Aldrich, and the residual solvent used as sthe tandard, the NMR signals was assigned with help from calculation made in ChemBioDraw Professional v.15.0.0106. Solvent signals were assigned according to Fulmer *et al.*[292]. IR spectra were recorded using a Bruker ALPHA FT-IR spectrometer using an ATR module. An Eppendorf Centrifuge 5810R V8.4 was used for all centrifugations.

7.1.1   Graphene Oxide Synthesis

Graphene oxide (GO) was prepared by a modified Hummer's method[135] in a two-step oxidation procedure inspired by S Gan *et al.*[229]. Pre-oxidized graphite was prepared in the first step, and GO prepared from pre-oxidized graphite in the second step.

$$\text{Graphite} \xrightarrow{\begin{array}{l}1)\ K_2S_2O_8\ /\ P_2O_5\ /\ H_2SO_4\ /\ 3h\ /\ 80\ ^\circ C\\2)\ KMnO_4\ /\ H_2SO_4\ /\ 2h\ /\ 35\ ^\circ C\end{array}} \text{Graphene Oxide}$$
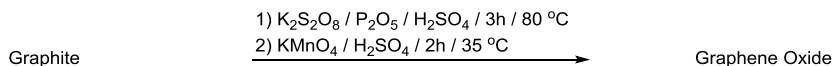
Graphite Flakes (powder, < 20 µm, synthetic) (5.0 g) were added to H_2SO_4 (conc. 96%) (15 mL) solution containing $K_2S_2O_8$ (2.5 g) and P_2O_5 (2.5 g) at 80 °C. After 3 hours, the reaction mixture was cooled to RT and the dark blue mixture diluted with 30 mL H_2O. The diluted reaction mixture was filtered and washed with H_2O until the waste solution reached neutral pH. The resulting crude pre-oxidized graphite powder was dried *in vacuo*.

Crude pre-oxidized graphite (1.1 g) was added to H_2SO_4 (conc. 96%) (25 mL) in an ice bath (0 °C). $KMnO_4$ (3.2 g) was then added slowly (20 min) under stirring, so that the temperature of the solution was maintained between 0 – 20 °C during the addition. After addition, the reaction mixture was stirred at 35 °C for 2 hours. After reaction the graphite oxide was purified either through aqueous workup producing GO also referred to as aqueous GO in Chapter 4, or by workup with anhydrous EtOAc referred to as anhydrous GO in Chapter 4.

Aqueous Workup

Workup based on modification of S. Gan *et.al.*[229] and O. C. Compton *et al.*[293]

The reaction was terminated by addition of H_2O (140 mL) and H_2O_2 (30% aq) (0.5 mL). The solution was centrifuged (12000 RPM, 18192 g) to remove the aqueous phase and washed by repeated centrifugation (12000 RPM, 18192 g, 20 min with HCl (10% aq) (5 × 180 mL) and H_2O (5 × 180 mL) retaining the solid GO and discarding the aqueous phase.

After washing, the sedimented GO was redispersed in H_2O and divided into approximate size distributions using centrifugation. The dispersion was first centrifuged at low speed (1000 RPM, 126 g, 20 min). The sediment from this step was discarded as multilayered Graphite Oxide. The supernatant was then centrifuged at medium speed (4000 RPM, 2021 g, 20 min). This sediment was redispersed and centrifuged at low speed (1000 RPM, 126 g, 20 min). This supernatant was marked as large GO sheets (mostly 10 – 20 µm). The supernatant from medium speed centrifugation was centrifuged again at medium-high speed (8000 RPM, 8085 g, 20 min) and the sediment redispersed and centrifuged at medium speed (4000 RPM, 2021 g, 20 min). This supernatant was marked as medium GO sheets (mostly 5 – 15 µm). The supernatant from medium-high speed centrifugation was then centrifuged at high speed (12000 RPM, 18192 g, 20 min) and the sediment from this step redispersed and centrifuged at medium-high speed (8000 RPM, 8085 g, 20 min). This supernatant was marked as small

GO sheets (mostly $1-8$ µm). The supernatant from the high-speed centrifugation was kept as very small and fragmented GO sheets (mostly < 1 µm) and also contains GO nanoparticles. The size of the GO sheets determined by AFM also showed sheets of other sizes in all four size-distributions but most of the sheets are within the size distribution given.

After size separation the GO sheets were purified by dialysis in H_2O (27×1 L) over a week using Spectra/Por membrane MWCO 12 000 – 14 000. Dialysis H_2O was changed five times daily during the first five days but only once daily over the final two days. After dialysis the concentration (in mg/mL) was determined by drying 5 mL of the solution in vacuum and weighing the residual powder.

The small GO sheets (mostly $1-8$ µm) were used in all further experiments of GO or aqueous GO described in this thesis. Dispersions of larger size GO were used in related master projects by the master students in our group.

Anhydrous Workup

Workup based on modification of A. Dimiev *et al.*[142] and O. C. Compton *et al.*[293]

The reaction was terminated by the addition of anhydrous EtOAc (140 mL) and $H_2O_{2\,(30\%\,aq)}$ (0.5 mL). The solution was centrifuged (12000 RPM, 18192 g, 20 min) to remove the solution phase and then washed by repeated centrifugation (12000 RPM, 18192 g, 20 min) and redispersion in anhydrous EtOAc ($5 \times$ 180 mL) retaining the solid GO and discarding the solution phase.

After washing, the sedimented GO was redispersed in anhydrous EtOAc. The dispersion was first centrifuged at medium speed (4000 RPM, 8085 g, 20 min). The sediment was discarded and the supernatant was then centrifuged at high speed (12000 RPM, 18192 g, 20 min). The sediment was redispersed and centrifuged at medium speed (4000 RPM, 8085 g, 20 min). The size of the GO sheets was determined by AFM images to about $1-10$ µm. This sample was used as anhydrous GO without further purification.

7.1.2 Triphosgene Activated Coupling of Boc-Glycin and Crown-Ether

Modification of T. Yechezkel *et al.*[227]
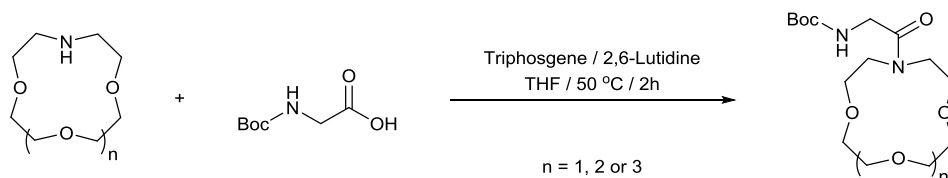
Boc-glycin (189.8 mg; 1.08 mmol) and Triphosgene (98.6 mg; 0.37 mmol) were dissolved in anhydrous THF (12 mL) followed by dropwise addition (2 min) of 2,6-lutidine (0.7 mL) under vigorous reaction. After the addition this mixture was slowly added to a heated solution of 1-aza-crown-ether (0.23 mmol) dissolved in anhydrous THF (15 mL) at 50 °C. After 2 hours the reaction was stopped by addition of H_2O (20 mL) and HCl $_{(1M, aq)}$ (30 mL) and immediately extracted with CH_2Cl_2 (3 × 30 mL). The organic phase was washed with NaOH $_{(1M, aq)}$ (20 mL), H_2O (20 mL), and dried over Na_2SO_4 $_{(s)}$. The solvent was removed *in vacuo* to a slightly yellow oil which was dried overnight *in vacuo*.

N-tert-Butyloxycarbonyl-*N*-2-aminoacetate-1-aza-18-crown[6]ether

Yield: 92.5 mg, 0.22 mmol, 95 %

TLC (CH_2Cl_2 9:1 MeOH): R_f = 0.34 – 0.38

^{1}H-NMR (400 MHz, CDCl$_3$, 298 K) δ: 5.48 (S, 2H, N(CO)C**H**$_2$N(CO)), 4.01
(d, J = 4.6 Hz, 4H, (C**H**$_2$)$_2$N(CO)R), 3.73 – 3.50 (m, 20H, CH$_2$C**H**$_2$O),
1.41 (s, 9H, OC(C**H**$_3$)$_3$).
^{13}C-NMR (101 MHz, CDCl$_3$) δ: 167.79 (R$_2$N(**C**O)R), 154.76 (N(**C**O)O),
78.35 (O**C**(CH$_3$)$_3$), 70.03, 69.77, 69.70, 69.67, 69.64, 69.56, 69.53, 69.33, 68.52, 68.31
(10 × O**C**H$_2$**C**H$_2$), 47.11, 45.84 (2 × N**C**H$_2$**C**H$_2$), 41.31 (N(CO)**C**H$_2$NCO),
27.37 (OC(**C**H$_3$)$_3$).

N-tert-Butyloxycarbonyl-*N*-2-aminoacetate-1-aza-15-crown[5]ether

Yield: 71.5 mg, 0.19 mmol, 82 %

TLC (CH_2Cl_2 9:1 MeOH): R_f = 0.35 – 0.39

^{1}H-NMR (400 MHz, CDCl$_3$, 298 K) δ: 5.46 (S, 2H, N(CO)C**H**$_2$N(CO)),
3.91 (d, J = 4.6 Hz, 4H, (C**H**$_2$)$_2$N(CO)R), 3.75 – 3.49 (m, 16H, CH$_2$C**H**$_2$O),
1.47 (s, 9H, OC(C**H**$_3$)$_3$).
^{13}C-NMR (101 MHz, CDCl$_3$) δ: 167.81 (R$_2$N(**C**O)R), 154.72 (N(**C**O)O),
78.24 (O**C**(CH$_3$)$_3$), 70.13, 69.67, 69.65, 69.61, 69.56, 69.43, 68.63, 68.43 (8 × O**C**H$_2$**C**H$_2$),
47.11, 45.84 (2 × N**C**H$_2$**C**H$_2$), 41.31 (N(CO)**C**H$_2$NCO), 27.47 (OC(**C**H$_3$)$_3$).

_N_-tert-Butyloxycarbonyl-_N_-2-aminoacetate-1-aza-12-crown[4]ether

Yield: 69.8 mg, 0.21 mmol, 91 %

TLC (CH$_2$Cl$_2$ 9:1 MeOH): R$_f$ = 0.32 – 0.40

^{1}H-NMR (400 MHz, CDCl$_3$, 298 K) δ: 5.51 (S, 2H, N(CO)C**H**$_2$N(CO)),
4.07 (d, J = 4.6 Hz, 4H, (C**H**$_2$)$_2$N(CO)R), 3.69 – 3.37 (m, 16H, CH$_2$C**H**$_2$O),
1.45 (s, 9H, OC(C**H**$_3$)$_3$).
^{13}C-NMR (101 MHz, CDCl$_3$) δ: 166.43 (R$_2$N(**C**O)R), 155.82 (N(**C**O)O),
78.41 (O**C**(CH$_3$)$_3$), 70.27, 69.81, 69.66, 69.47, 68.88, 68.57 (6 × O**C**H$_2$**C**H$_2$),
47.31, 45.64 (2 × N**C**H$_2$**C**H$_2$), 41.27 (N(CO)**C**H$_2$NCO), 27.34 (OC(**C**H$_3$)$_3$).

7.1.3 Deprotection of Boc-Protected 2-Aminoacetate-1-Aza-Crown-Ether

Modification of S.E. Blondelle and R. A. Houghten[228]
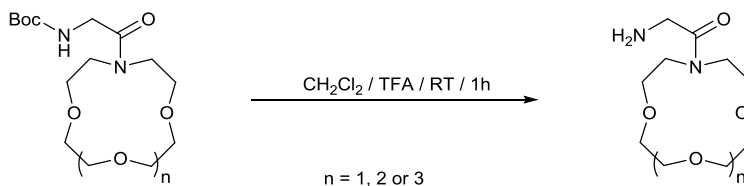
_N_-tert-Butyloxycarbonyl-_N_-2-aminoacetate-1-aza-crown-ether (as prepared) was dissolved in CH$_2$Cl$_2$ (20 mL), trifluoroacetic acid (10 mL) was added, and the mixture stirred at RT for 1 hour. The reaction mixture was concentrated to oil _in vacuo_. The oil was redissolved in CH$_2$Cl$_2$ (20 mL), washed with NaOH $_{(1M\ aq)}$ (2 × 20 mL), H$_2$O (20 mL), and dried over Na$_2$SO$_4$ $_{(s)}$. Solvent was removed _in vacuo_ give a slightly yellow oil which was dried overnight _in vacuo_.

2-aminoacetate-1-aza-18-crown[6]ether

Yield: 59.0 mg, 0.18 mmol, 84 %   (of 0.22 mmol)

TLC (CH$_2$Cl$_2$ 9:1 MeOH): R$_f$ = 0.06 – 0.09

^{1}H-NMR (400 MHz, CDCl$_3$, 298 K) δ: 3.98 (bs, 4H, (C**H**$_2$)$_2$N(CO)R) 3.71 – 3.61 (m, 20H, CH$_2$C**H**$_2$O), 2.72 (s, 2H, N(CO)C**H**$_2$NH$_2$). (No NH$_2$ signal was observed)
^{13}C-NMR (101 MHz, CDCl$_3$) δ: 159.80 (R$_2$N(**C**O)R), 70.73, 70.69, 70.68, 69.84, 69.57, 69.45, 69.19, 69.17, 69.14, 69.10 (10 × O**C**H$_2$**C**H$_2$), 29.48, 49.43 (2 × N**C**H$_2$**C**H$_2$), 40.94 (NCO**C**H$_2$NH2).

2-aminoacetate-1-aza-15-crown[5]ether

Yield: 44.2 mg, 0.16 mmol, 89 %   (of 0.19 mmol)

TLC (CH$_2$Cl$_2$ 9:1 MeOH): R$_f$ = 0.05 – 0.08

^{1}H-NMR (400 MHz, CDCl$_3$, 298 K) δ: 3.99 (t, J = 7.4 Hz, 4H, (**CH**$_2$)$_2$N(CO)R) 3.73 – 3.58 (m, 16H, C**H**$_2$C**H**$_2$O), 2.78 (s, 2H, N(CO)C**H**$_2$NH$_2$). (No NH$_2$ signal was observed)

^{13}C-NMR (101 MHz, CDCl$_3$) δ: 159.72 (R$_2$N(**C**O)R), 70.77, 70.68, 69.53, 69.47, 69.23, 69.19, 69.11, 69.07 (8 × O**C**H$_2$**C**H$_2$), 29.37, 49.31 (2 × N**C**H$_2$**C**H$_2$), 40.84 (NCO**C**H$_2$NH$_2$).

2-aminoacetate-1-aza-12-crown[4]ether

Yield: 44.1 mg, 0.19 mmol, 90 %   (of 0.21 mmol)

TLC (CH$_2$Cl$_2$ 9:1 MeOH): R$_f$ = 0.05 – 0.11

^{1}H-NMR (400 MHz, CDCl$_3$, 298 K) δ: 4.05 (t, J = 7.3 Hz, 4H, (**CH**$_2$)$_2$N(CO)R) 3.74 – 3.65 (m, 12H, C**H**$_2$C**H**$_2$O), 2.73 (s, 2H, N(CO)C**H**$_2$NH$_2$). (No NH$_2$ signal was observed)

^{13}C-NMR (101 MHz, CDCl$_3$) δ: 159.69 (R$_2$N(**C**O)R), 70.71, 70.63, 69.57, 69.51, 69.17, 69.03 (6 × O**C**H$_2$**C**H$_2$), 29.42, 49.29 (2 × N**C**H$_2$**C**H$_2$), 40.79 (NCO**C**H$_2$NH$_2$).

7.1.4   Crown-Ether Functionalization of GO or RGO

Modification of C. Shan *et al.*[184]
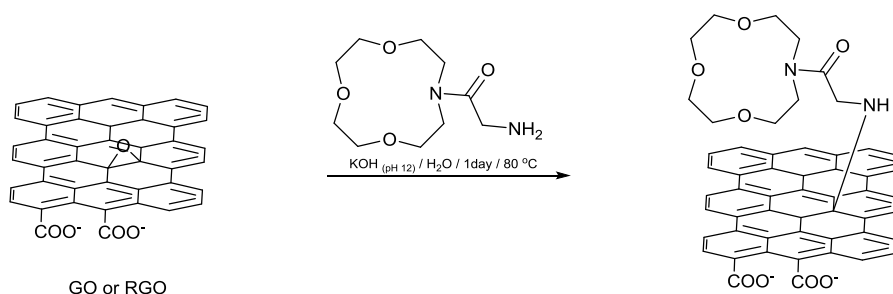
Aqueous dispersion (10 mL) of GO or RGO adjusted to 1 mg/mL was prepared. A solution of 2-amino-crown-ether (0.05 mmol) in H$_2$O (0.5 mL) was then added to the dispersion under vigorous stirring for 30 min. KOH$_{(aq\ 8\ M)}$ (0.25 mL) was added adjusting pH to ≈ 12, the pH adjusted dispersion was heated to 60 °C and stirred overnight. The dispersion was then cooled to room temperature, centrifuged at (12000 RPM, 18192 g, 20 min) and washed twice by centrifugation with H$_2$O (2 × 10 mL). After the third centrifugation the sediment was redispersed in H$_2$O (10 mL) and dialyzed in H$_2$O (27 × 100 mL) over a week using Spectra/Por membranes MWCO 12 000 – 14 000.

This procedure was also successfully scaled up to 100 mL dispersion.

7.1.5   Graphene Oxide Reduction: Alkaline

Modification of X. Fan *et al.*[157]

Graphene Oxide $\xrightarrow{\text{KOH (pH 14) / H}_2\text{O} /\ \ 6h / 60\ ^{\circ}\text{C}}$ Reduced Graphene Oxide
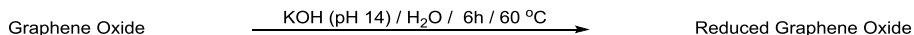
Aqueous dispersion (10 mL) of GO or functionalized GO adjusted to 1 mg/mL was prepared and heated to 80°C. $KOH_{(aq\ 8\ M)}$ (1.5 mL) was added to the heated dispersion adjusting pH to ≈ 14. The dispersion was stirred for 6 hours before cooling to room temperature, centrifuged at (12000 RPM, 18192 g, 20 min) and washed twice by centrifugation with H_2O (2×10 mL). After the third centrifugation the sediment was redispersed in H_2O (10 mL) and dialyzed in H_2O (27×100 mL) over a week using Spectra/Por membranes MWCO 12 000 – 14 000.

This procedure was also successfully scaled up to 100 mL dispersion.

7.1.6   Graphene Oxide Reduction: Ascorbic Acid

Modification of J. Zhang *et al.*[153]

Graphene Oxide $\xrightarrow{\text{L-ascorbic acid / H}_2\text{O} / 24h / RT}$ Reduced Graphene Oxide
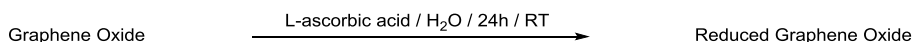
Aqueous dispersion (10 mL) of GO or functionalized GO adjusted to 1 mg/mL was prepared. L-ascorbic acid (0.57 mmol ,100 mg) was added to the dispersion under vigorous stirring overnight. The dispersion was then centrifuged at (12000 RPM, 18192 g, 20 min) and washed twice by centrifugation with H_2O (2×10 mL). After the third centrifugation the sediment was redispersed in H_2O (10 mL) and dialyzed in H_2O (27×100 mL) over a week using Spectra/Por membranes MWCO 12 000 – 14 000.

7.1.7   Graphene Oxide Reduction: Zn/H$_3$O$^+$

Modification of X. Mei and J. Ouyand[155]

Graphene Oxide $\xrightarrow{\text{HCl (pH 2) / Zn / H}_2\text{O} / 1h / RT}$ Reduced Graphene Oxide
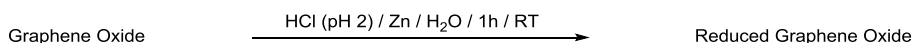
Aqueous dispersion (10 mL) of GO or functionalized GO adjusted to 1 mg/mL was prepared. $HCl_{(aq\ 37\%)}$ (dropwise) was used to adjust pH to ≈ 2. Zn powder (50 mg) was then added to the stirred dispersion. After 1 hour excess Zn powder was dissolved by added $HCl_{(aq\ 37\%)}$ (1 mL). The dispersion was then cooled to room temperature, centrifuged at (12000 RPM, 18192 g, 20 min) and washed twice by centrifugation with H_2O (2×10 mL). After the third centrifugation the sediment was redispersed in H_2O (10 mL) and dialyzed in H_2O (27×100 mL) over a week using Spectra/Por membranes MWCO 12 000 – 14 000.

7.1.8 Silyl Protection of Glycol Linker
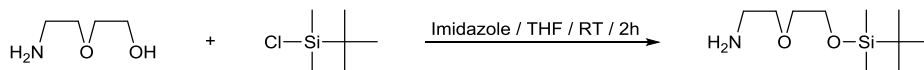
2-(2-aminoethoxy)ethan-1-ol (5 mL, 5.24 g, 50 mmol) and imidazole (8.51 g, 125 mmol) were dissolved in anhydrous THF (50 mL). *t*-Butylchlorodimethylsilane 50% in toluene (20 mL, 8.7 g, 57.7 mmol) was added slowly over 30 min and the reaction left to stir for an additional 90 min. H_2O (100 mL) was added and pH adjusted with NaOH (aq 1M) to pH ≈ 5. 2-(2-((*t*-Butyldimethylsilyl)oxy)ethoxy)ethan-1-amine was extracted with CH_2Cl_2 (5×20 mL) and the solvent removed *in vacuo* giving a colourless oil (8,89 g, 40.5 mmol, 81 %)

^{1}H-NMR (400 MHz, CDCl$_3$, 298 K) δ: 3.94 (bs, 2H), 3.66 (t, J = 5.1 Hz, 2H, Si–O–C**H**$_2$), 3.45 – 3.39 (m, 4H, 2×O–C**H**$_2$), 2.78 (t, 5.1 Hz, 2H, N–C**H**$_2$), 0.78 (s, 9H, 3×C–C**H**$_3$), −0.04 (s, 6H, Si–C**H**$_3$).

^{13}C-NMR (101 MHz, CDCl$_3$) δ: 72.88, 72.39 (2×O–C**H**$_2$), 62.65 (Si–O–C**H**$_2$), 41.60 (N–C**H**$_2$), 25.86 (3×C–C**H**$_3$), 18.31 (**C**–CH$_3$) −5.31 (Si–C**H**$_3$).

7.1.9 GO functionalization: Through Nucleophilic Approach

Modification of R. Kumar *et.al.*[256]
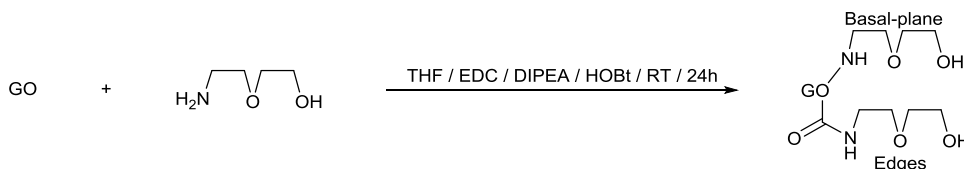
GO (0.5 g) (either aqueous or anhydrous) was centrifuged to remove most solvent followed by drying *in vacuo* for 10 days. It was then grinded in a mortar, (0.1 g) redispersed in anhydrous THF (100 mL), and ultra-sonicated for 30min, then centrifuged and redispersed in anhydrous THF (100 mL). This process was repeated five times, followed by drying the GO *in vacuo*.

Dried GO (80 mg) was dispersed in anhydrous THF (75 mL) and sonicated for 30 min. *N*-(3-Dimethylaminopropyl)-*N′*-ethylcarbodiimide hydrochloride (0.3 g, 1.56 mmol), hydroxybenzotriazole (0.59 g, 4.36 mmol), and *N,N*-diisopropylethylamine (1.4 mL, 1 g, 8 mmol) were dissolved in anhydrous THF (5 mL) and added over 5 min. After 24 hours, the reaction mixture was centrifuged (12000 RPM, 18192 g, 20 min), redispersed in anhydrous THF (100 mL), centrifuged, and used as crude product in next synthesis step (section 7.1.11 page 111).

7.1.10 GO functionalization: Isocyanate

Modified combination of H.-J. Knölker and T. Braxmeier[259] and S. Stankovich *et al.*[185]
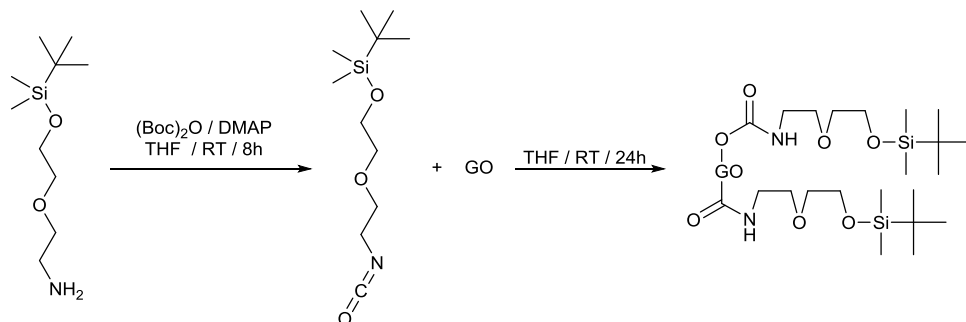
GO (0.5 g) (either aqueous or anhydrous) was centrifuged to remove most solvent followed by drying *in vacuo* for 10 days. It was then grinded in a mortar, (0.1 g) redispersed in anhydrous THF (100 mL), and ultra-sonicated for 30min, then centrifuged and redispersed in anhydrous THF (100 mL). This process was repeated five times, followed by drying the GO *in vacuo*.

Glycol reaction mixture: 2-(2-((*t*-Butyldimethylsilyl)oxy)ethoxy)ethan-1-amine (3.4 g, 15.5 mmol) and 4-(dimethylamino)pyridine (1.9 g, 155.5 mmol) were dissolved in anhydrous THF (50 mL), di-*t*-butyl dicarbonate (3.65 mL, 3.55g, 16.26 mmol) was added over 10 min, the reaction mixture left stirring 8 hours.

Dried GO (80 mg) was dispersed in anhydrous THF (55 mL) and sonicated for 30 min. The glycol reaction mixture (25 mL) was added to the dispersion and left stirring overnight. The dispersion was centrifuged (12000 RPM, 18192 g, 20 min), redispersed in anhydrous THF (100 mL), centrifuged and used as crude product in next synthesis step (section 7.1.11 page 111).

7.1.11 GO Reduction: NaBH$_4$

Modification of H.-J. Shin[152]
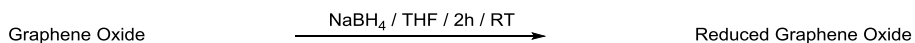
Functionalized GO ($\approx$ 80 mg) was dispersed in anhydrous THF (80 mL), NaBH$_4$ (0.25 g, 6 mmol) added, and the reaction mixture left stirring for two hours, before being centrifuged (12000 RPM, 18192 g, 20 min). The solid was then redispersed in anhydrous THF (100 mL), centrifuged and used as crude product in the next synthesis step (either section 7.1.12 page 112 or section 7.1.13 page 112).

7.1.12   Silyl Deprotection

Modification of E.J Corey and A. Venkateswarlu[260]

Silyl protected functionalized RGO ($\approx$ 80 mg) was dispersed in anhydrous THF (80 mL) and Tetra-*n*-butylammonium fluoride (1.02 g, 3.9 mmol) added. The reaction mixture was left stirring 1 hour, before being centrifuged (12000 RPM, 18192 g, 20 min). This was followed by redispersion in anhydrous THF (100 mL) and centrifugation and then used as crude product in next synthesis step (section 7.1.13 page 112).

7.1.13   Mitsunobu Reaction

Modification of C. Besset[257]
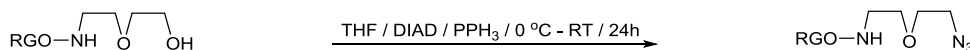
Hydroxyl functionalized RGO ($\approx$ 80 mg) was dispersed in anhydrous THF (60 mL) and cooled to 0 °C in an ice bath. NaN_3 (1.3g, 20 mmol) was dissolved in anhydrous THF 10 mL. Anhydrous $NaSO_4$ ($\approx$ 4g) and then $H_2SO_{4(conc.\ 96\%)}$ (1 mL) was added and stirred for 30 min. This *in situ* HN_3 solution was added through a filter syringe to the RGO dispersion. Diisopropyl azodicarboxylate (0.8 g, 4 mmol) and Triphenylphosphine (1.05g ,4 mmol) were dissolved in anhydrous THF and added to the RGO dispersion and stirred for 24 hours in which time the cooling bath was allowed to heat to room temperature. The dispersion was then centrifuged (12000 RPM, 18192 g, 20 min), redispersed in anhydrous THF (100 mL), centrifuged dispersed in H_2O (5×100 mL) and centrifuged again. The whole process was repeated 5 times. Finally, the Azido-RGO was dispersed in (60 mL) 1 mL was removed to measure the concentration by drying over 7 days while the rest was dialyzed in H_2O (27 × 600 mL) over a week using Spectra/Por membranes MWCO 12 000 – 14 000. After dialysis the concentration of the dispersion was diluted to 1 mg/mL.

7.1.14 CuAAC Coupling Reaction with Ferrocene
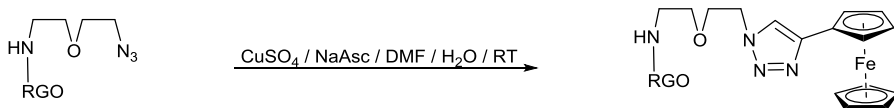
Ethynylferrocene (5 mg, 24 µmol) was dissolved in DMF (2 mL). $CuSO_4$ (4 mg, 24 µmol) and sodium ascorbate (23.7 mg, 120 µmol) were dissolved in H_2O (1 ml) and azido-RGO dispersion (1 mL, 1mg/mL). The three solutions/dispersions were mixed and stirred for 24 hours. Ferrocene functionalized RGO was then centrifuged (12000 RPM, 18192 g, 20 min) and washed by redispersion followed by centrifugation first in DMF (5×5 mL), then in H_2O (5×5 mL), and finally it was redispersed in H_2O (1 mL) and dialyzed in H_2O (27 × 10 mL) over a week using Spectra/Por membranes MWCO 12 000 – 14 000.

7.1.15 CuAAC Coupling Reaction with TTF-Calix[4]pyrrole
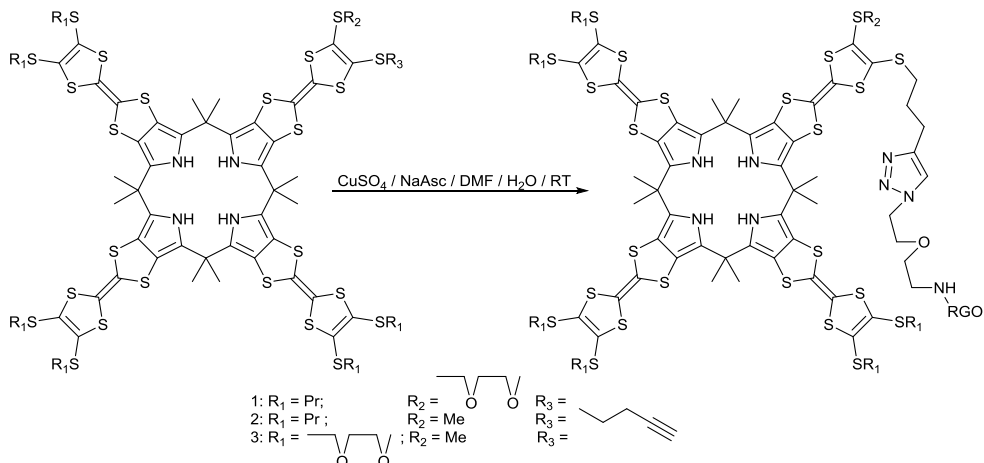
TTF-calix[4]pyrrole X (10 mg, ≈ 5 µmol) was dissolved in DMF (3 mL). $CuSO_4$ (4 mg, 24 µmol) and Sodium ascorbate (23.7 mg, 120 µmol) were dissolved in H_2O (1 ml) and azido-RGO dispersion (1 mL, 1mg/mL). The three solutions/dispersions were mixed and stirred for 24 hours. TTF-calix[4]pyrrole functionalized RGO was then centrifuged (12000 RPM, 18192 g, 20 min) and washed by redispersion followed by centrifugation first in DMF (5×5 mL) and then in H_2O (5×5 mL). It was finally redispersed in H_2O (1 mL) and dialyzed in H_2O (27 × 10 mL) over a week using Spectra/Por membranes MWCO 12 000 – 14 000.

7.2   Electrochemical Procedures

Potentiometric studies were carried out using a CHI Model 700C general-purpose potentiostat. Other electrochemical measurements were carried out using a Autolab PGSTAT12 system. All electrochemical experiments were performed under Ar atmosphere with vigours degassing for 30 min prior to experiment.

7.2.1   Functionalization of Glassy-Carbon Electrode

A glassy carbon electrode with a surface area of 7 mm^2 was polished with 1.0 µm, 0.3 µm and 0.05 µm alumina slurry and ultra-sonicated in H_2O 2×5 min and blow-dried with N_2. 10 – 15 µL of a functional material in aqueous solution was drop cast onto the electrode surface and dried. For potentiometric studies drying was done overnight, for all other studies the electrode was dried 30 – 60min in vacuum immediately prior to use.

7.2.2   Screen-Printed Electrode Measurements

The DropSense 150 electrodes used consist of 4 mm diameter carbon working, Pt counter and Ag reference electrodes.

Functionalization: The electrode was rinsed with ethanol and H_2O, and then air-dried. 15 µL of 1 mg/mL aqueous dispersion was drop cast on the working electrode and dried overnight.

Measurement: A DropSense connection box was used to connect working, counter and reference electrode. The OCP of 50 µL of 0.1 M $NaNO_3$ solution was first measured and recorded, and the electrode then rinsed lightly with H_2O. 8.5mg $NaNO_3$ was added to 1 mL of the sample of interest, 50 µL drop cast on the electrode and OCP was measured recording the change from first measurement.

7.2.3   Fabrication of a S-D Device

Preparation of S-D device: 3.8×1.8 cm^2 glass plates were cut and cleaned by ultra-sonication in ethanol and H_2O. A metallic mask (Figure 88B) was then immobilized over the centre of the glass. A layer of Chromium acting as glue between gold and glass was sputtered onto the glass followed by three layers of gold. A 3mm O-ring was placed over the gap between the two gold electrodes and 100 µL 0.5 mg/mL RGO material drop cast in the O-ring and dried overnight.
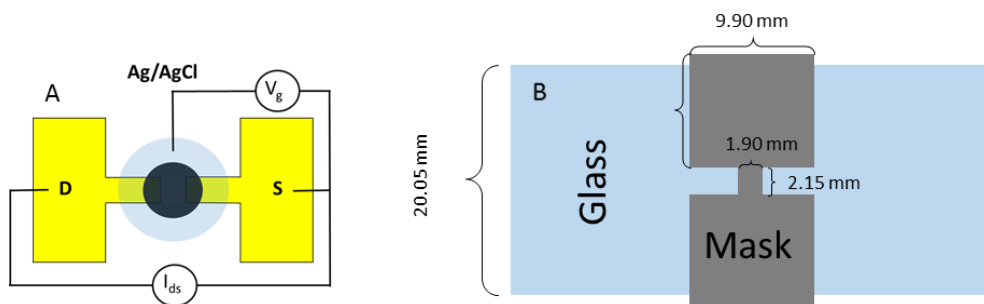
Figure 88: A) schematic of electrochemical system; B) dimensions of mask used to cover part of the glass slide during sputtering.

Measurements: The O-ring used for depositing RGO-film was exchanged for a 5 mm O-ring, a 1 mL glass reservoir was fixed over the O-ring, and an Ag/AgCl reference electrode was inserted into the electrolyte solution Figure 88A.

7.3   Other Experimental Procedures

7.3.1   XPS

Sample preparation: HPS Si Wafer (Topsil: 334110000525013) was cut into 5×5 mm^2 sample plates rinsed in acidic piranha (3 H_2SO_4 : 1 H_2O_2) ***Caution!*** *The piranha solution is extremely dangerous and should be handled with caution; in some circumstances, most commonly when it has been mixed with a significant amount of oxidizable organic material, it has detonated unexpectedly*. The XPS sample was then drop cast onto the sample plate and dried *in vacuo*. This drop casting process was repeated four times to ensure coverage of the silicon plate.

Measurement: Before measurement the samples were degasses in pre-analysis chamber at 10^{-5} bar for at least 30 min. XPS was then recorded on Thermo Scientific X-ray photoelectron spectrometer with an Al K-Alpha (1486 eV) X-ray source. The X-ray spot area is set to 400 µm and a flood gun used for charge compensation.

The following settings where used for recording of the different spectra:

1) Survey (pass energy 2000 KeV, energy step 1 KeV, scans 4, dwell time 50 s)
2) Si2p (pass energy 50 KeV, energy setp 0.1 KeV, scans 2, dwell time 50 s)
3) S2p (pass energy 50 KeV, energy step 0.1 KeV, scans 2 or 10, dwell time 50 s)
4) C1s (pass energy 50 KeV, energy step 0.075 KeV, scans 12, dwell time 50s)
5) N1s (pass energy 50 KeV, energy step 0.075 KeV, scans 12, dwell time 50s)
6) O1s (pass energy 50 KeV, energy step 0.1 KeV, scans 6, dwell time 50s)
7) Fe2p (pass energy 50 KeV, energy step 0.1 KeV, scans 10, dwell time 50s)

Two scans were used for S2p in samples where S is not presumed to be present and ten scans in samples where S is presumed to be present; Fe2p was only measured for ferrocene functionalized RGO samples.

Data processing: All data were processed in the program Thermo Avantage v4.88 where survey analysis of elemental composition, and the specific orbital spectra were deconvoluted.

7.3.2   AFM

Sample preparation: 1×1 cm^2 mica sample plates were mounted on magnets for easy mounted on AFM setup, and then the top layer was peeled off using scotch tape, before 50 µL sample was drop cast onto the mica, usually 3 different concentration of each material was used for drop casting.

Imaging: AFM Images were recorded in the contact mode using an Agilent SPS 5500 instrument in open loop setup with an Agilent multipurpose scanner 90 µm × 90 µm equipped. The tip was a Bruker DNP-S tip with a force constant of ≈ 0.35 N/m and ≈ 10 nm tip radius according to the manufacturer. Picoview V.14.4 was used as imaging software.

Data processing: Pico Image Basic V.6.2 was used to prepare images where several operations were used: 1st order leveling in the form of Plane leveling defined by three points; 2nd order leveling in the form of 2nd order polynomial form removal (only needed for large area sample >10×10 µm); systematic scanning artifact reduction in the form of Line correction in scanning direction; and denoising by median Spatial filtering.

Bibliography

(1)   McEwen, C. N.; Ligler, F. S.; Swager, T. M. *Chem. Soc. Rev.* **2013**, *42*, 8581–8583.

(2)   Wang, J. *Biosens. Bioelectron.* **2006**, *21*, 1887–1892.

(3)   Sanghavi, B. J.; Sitaula, S.; Griep, M. H.; Karna, S. P.; Ali, M. F.; Swami, N. S. *Anal. Chem.* **2013**, *85*, 8158–8165.

(4)   Hamilton, G. R. C.; Sahoo, S. K.; Kamila, S.; Singh, N.; Kaur, N.; Hyland, B. W.; Callan, J. F. *Chem. Soc. Rev.* **2015**, *44*, 4415–4432.

(5)   Nordrehaug, J. E.; Johannessen, K. A.; von der Lippe, G. *Circulation* **1985**, *71*, 645–649.

(6)   Lan, W.; Zou, X. U.; Hamedi, M. M.; Hu, J.; Parolo, C.; Maxwell, E. J.; Bu, P.; Whitesides, G. M. *Anal. Chem.* **2014**, *86*, 9548–9553.

(7)   Hart, J. P.; Wring, S. A. *TrAC Trends Anal. Chem.* **1997**, *16*, 89–103.

(8)   Metters, J. P.; Kadara, R. O.; Banks, C. E. *Analyst* **2011**, *136*, 1067.

(9)   Suslick, K. S. *MRS Bull.* **2004**, *29*, 720–725.

(10)   Moos, R.; Izu, N.; Rettig, F.; Reiß, S.; Shin, W.; Matsubara, I. *Sensors* **2011**, *11*, 3439–3465.

(11)   Brownson, D. a C.; Banks, C. E. *Analyst* **2010**, *135*, 2768–2778.

(12)   Wu, S.; He, Q.; Tan, C.; Wang, Y.; Zhang, H. *Small* **2013**, *9*, 1160–1172.

(13)   Shao, Y.; Wang, J.; Wu, H.; Liu, J.; Aksay, I. A.; Lin, Y. *Electroanalysis* **2010**, *22*, 1027–1036.

(14)   Yoshio, M.; Noguchi, H. *Anal. Lett.* **1982**, *15* (15), 1197–1276.

(15)   Dalapati, S.; Jana, S.; Guchhait, N. *Spectrochim. Acta - Part A Mol. Biomol. Spectrosc.* **2014**, *129*, 499–508.

(16)   Gramage-Doria, R.; Armspach, D.; Matt, D. *Coord. Chem. Rev.* **2013**, *257*, 776–816.

(17)   Sambrook, M. R.; Notman, S. *Chem. Soc. Rev.* **2013**, *42*, 9251–9267.

(18)   Pinalli, R.; Suman, M.; Dalcanale, E. *European J. Org. Chem.* **2004**, *2004*, 451–462.

(19)   Wu, S.; Lan, X.; Cui, L.; Zhang, L.; Tao, S.; Wang, H.; Han, M.; Liu, Z.; Meng, C. *Anal. Chim. Acta* **2011**, *699*, 170–176.

(20)   Guo, Y.; Guo, S.; Li, J.; Wang, E.; Dong, S. *Talanta* **2011**, *84*, 60–64.

(21)   Liu, Z.; Zhang, A.; Guo, Y.; Dong, C. *Biosens. Bioelectron.* **2014**, *58*, 242–248.

(22)   Lu, D.; Lin, S.; Wang, L.; Shi, X.; Wang, C.; Zhang, Y. *Electrochim. Acta* **2012**, *85*, 131–138.

(23)   Fu, L.; Lai, G.; Yu, A. *RSC Adv.* **2015**, *5*, 76973–76978.

(24)   Zhang, Z.; Gu, S.; Ding, Y.; Shen, M.; Jiang, L. *Biosens. Bioelectron.* **2014**, *57*, 239–244.

(25)   Nag, S.; Duarte, L.; Bertrand, E.; Celton, V.; Castro, M.; Choudhary, V.; Guegan, P.;

Feller, J. *J. Mater. Chem. B* **2014**, *2*, 6571–6579.

(26)   Buck, L.; Axel, R. *Cell* **1991**, *65*, 175–187.

(27)   Fu, X.; Benson, R. F.; Wang, J.; Fries, D. *Sens. Actuat. B Chem.* **2005**, *106*, 296–301.

(28)   Burnworth, M.; Rowan, S. J.; Weder, C. *Chem. Eur. J* **2007**, *13*, 7828–7836.

(29)   Hulanicki, a.; Glab, S.; Ingman, F. *Pure Appl. Chem.* **1991**, *63*, 1247–1250.

(30)   Xia, F.; Zuo, X.; Yang, R.; Xiao, Y.; Kang, D.; Vallee-Belisle, A.; Gong, X.; Yuen, J. D.; Hsu, B. B. Y.; Heeger, A. J.; Plaxco, K. W. *Proc. Natl. Acad. Sci. USA* **2010**, *107*, 10837–10841.

(31)   Nolan, E. M.; Lippard, S. J. *J. Am. Chem. Soc.* **2003**, *125*, 14270–14271.

(32)   Ghosn, M. W.; Wolf, C. *Tetrahedron* **2011**, *67*, 6799–6803.

(33)   Li, X.-G.; Feng, H.; Huang, M.-R.; Gu, G.-L.; Moloney, M. G. *Anal. Chem.* **2012**, *84*, 134–140.

(34)   Dey, R. S.; Raj, C. R. *J. Phys. Chem. C* **2010**, *114*, 21427–21433.

(35)   Chen, Q.; Zhu, L.; Zhao, C.; Wang, Q.; Zheng, J. *Adv. Mater.* **2013**, *25*, 4171–4176.

(36)   You, L.; Zha, D.; Anslyn, E. V. *Chem. Rev.* **2015**, *115*, 7840–7892.

(37)   Sun, R.; Wang, L.; Yu, H.; Abdin, Z.; Chen, Y.; Huang, J.; Tong, R. *Organometallics* **2014**, *33*, 4560–4573.

(38)   Warwick, C.; Guerreiro, A.; Soares, A. *Biosens. Bioelectron.* **2013**, *41*, 1–11.

(39)   Fischer, E. H. *Ber. Dtsrh. Clieni. Ges.* **1894**, *27*, 29–85 – 2993.

(40)   Rajagopal, S.; Rajagopal, K.; Lefkowitz, R. J. *Nat. Rev. Drug Discov.* **2010**, *9*, 373–386.

(41)   Litman, G. W.; Rast, J. P.; Shamblott, M. J.; Haire, R. N.; Hulst, M.; Roess, W.; Litman, R. T.; Hinds-Frey, K. R.; Zilch, a; Amemiya, C. T. *Mol. Biol. Evol.* **1993**, *10*, 60–72.

(42)   Chen, L.; Xu, S.; Li, J. *Chem. Soc. Rev.* **2011**, *40*, 2922.

(43)   Feynman, R. P. *Eng. Sci.* **1960**, *23*, 22–36.

(44)   EU. *Commission recommendation of 18 October 2011 on the definition of nanomaterial (2011/696/EU).*; 2011; Vol. L275.

(45)   Ruska, E.; Dahlem, D. B.; Germany, W.; Planck-gesellschaft, D. M. *Rev. Mod. Phys.* **1987**, *59*, 627–637.

(46)   Binnig, G.; Rohrer, H.; Gerber, C.; Weibel, E. *Phys. Rev. Lett.* **1982**, *49*, 57–61.

(47)   Nobelprize.org. The Nobel Prize in Physics 1986 http://www.nobelprize.org/nobel_prizes/physics/laureates/1986/ (accessed Oct 28, 2015).

(48)   Binnig, G.; Quate, C. F. *Phys. Rev. Lett.* **1986**, *56*, 930–933.

(49)   Zhang, X.; Guo, Q.; Cui, D. *Sensors* **2009**, *9*, 1033–1053.

(50)   Vaddiraju, S.; Tomazos, I.; Burgess, D. J.; Jain, F. C.; Papadimitrakopoulos, F. *Biosens. Bioelectron.* **2010**, *25*, 1553–1565.

(51)   Huang, C.; Huang, M. The Scale of the Universe 2 http://htwins.net/scale2/ (accessed Apr 13, 2016).

(52)   Burda, C.; Chen, X.; Narayanan, R.; El-Sayed, M. A. *Chem. Rev.* **2005**, *105*, 1025–1102.

(53)   Ariga, K.; Li, M.; Richards, G. J.; Hill, J. P. *J. Nanosci. Nanotechnol.* **2011**, *11*, 1–13.

(54)   Li, N.; Zhao, P.; Astruc, D. *Angew. Chem. Int. Ed.* **2014**, *53*, 1756–1789.

(55)   Kharisov, B. I. *Recent Pat. Nanotechnol.* **2008**, *2*, 190–200.

(56)   Xia, Y.; Yang, P.; Sun, Y.; Wu, Y.; Mayers, B.; Gates, B.; Yin, Y.; Kim, F.; Yan, H. *Adv. Mater.* **2003**, *15*, 353–389.

(57)   Osada, M.; Sasaki, T. *Adv. Mater.* **2012**, *24*, 210–228.

(58)   Gates, B. D.; Xu, Q.; Stewart, M.; Ryan, D.; Willson, C. G.; Whitesides, G. M. *Chem. Rev.* **2005**, *105*, 1171–1196.

(59)   Bartels, L.; Meyer, G.; Rieder, K.-H. *Phys. Rev. Lett.* **1997**, *79*, 697–700.

(60)   Oyabu, N.; Custance, O.; Yi, I.; Sugawara, Y.; Morita, S. *Phys. Rev. Lett.* **2003**, *90*, 176102.

(61)   Lehn, J. M. *Pure Appl. Chem.* **1978**, *50*, 871–892.

(62)   Nobelprize.org. The Nobel Prize in Chemistry 1987 http://www.nobelprize.org/nobel_prizes/chemistry/laureates/1987 (accessed Nov 3, 2015).

(63)   Lehn, J.-M. *Angew. Chemie Int. Ed.* **1988**, *27*, 89–112.

(64)   Lehn, J. M. In *Nobel Lectures Chemistry 1981-1990*; Malmström, B. G., Ed.; World Scientific, 1987; p 445.

(65)   Liu, K.; Kang, Y.; Wang, Z.; Zhang, X. *Adv. Mater.* **2013**, *25*, 5530–5548.

(66)   Chakrabarty, R.; Mukherjee, P. S.; Stang, P. J. *Chem. Rev.* **2011**, *111*, 6810–6918.

(67)   Kay, E. R.; Leigh, D. A.; Zerbetto, F. *Angew. Chemie Int. Ed.* **2007**, *46*, 72–191.

(68)   Steed, J. W.; Atwood, J. L. In *Supramolecular Chemistry*; John Wiley & Sons, Ltd., 2009; pp 27–38.

(69)   Lide, D. R. *Handbook of Chemistry and Physics*, 76th Ed.; CRC Press inc., 1995.

(70)   Tulyakova, E.; Delbaere, S.; Fedorov, Y.; Jonusauskas, G.; Moiseeva, A.; Fedorova, O. *Chem. Eur. J* **2011**, *17*, 10752–10762.

(71)   Valeur, B.; Leray, I. *Inorg. Chim. Acta* **2007**, *360*, 765–774.

(72)   Palacios, M. A.; Nishiyabu, R.; Marquez, M.; Anzenbacher, P. *J. Am. Chem. Soc.* **2007**, *129*, 7538–7544.

(73)   Beer, P. D.; Gale, P. a. *Angew. Chemie Int. Ed.* **2001**, *40*, 486–516.

(74)   Klein, E.; Crump, M. P.; Davis, A. P. *Angew. Chemie* **2005**, *117*, 302–306.

(75)   Bähring, S.; Olsen, G.; Stein, P. C.; Kongsted, J.; Nielsen, K. A. *Chem. Eur. J* **2013**, *19*, 2768–2775.

(76)   Kojić-Prodić, B.; Molčanov, K. *Acta Chim. Slov.* **2008**, *55*, 692–708.

(77)   Grabowski, S. J. *Chem. Rev.* **2011**, *111*, 2597–2625.

(78)   Buckingham, A. D.; Del Bene, J. E.; McDowell, S. A. C. *Chem. Phys. Lett.* **2008**, *463*, 1–10.

(79)   Meot-Ner, M. *Chem. Rev.* **2005**, *105*, 213–284.

(80)   Goymer, P. *Nat. Chem.* **2012**, *4*, 863–864.

(81)   Moore, T. S.; Winmill, T. F. *J. Chem. Soc. Trans.* **1912**, *101*, 1614–1625.

(82)   Arunan, E.; Desiraju, G. R.; Klein, R. a.; Sadlej, J.; Scheiner, S.; Alkorta, I.; Clary, D. C.; Crabtree, R. H.; Dannenberg, J. J.; Hobza, P.; Kjaergaard, H. G.; Legon, A. C.; Mennucci, B.; Nesbitt, D. J. *Pure Appl. Chem.* **2011**, *83*, 1619–1636.

(83)   Arunan, E.; Desiraju, G. R.; Klein, R. a.; Sadlej, J.; Scheiner, S.; Alkorta, I.; Clary, D. C.; Crabtree, R. H.; Dannenberg, J. J.; Hobza, P.; Kjaergaard, H. G.; Legon, A. C.; Mennucci, B.; Nesbitt, D. J. *Pure Appl. Chem.* **2011**, *83*, 1637–1641.

(84)   Hunter, C. A. C.; Lawson, K. R. K.; Perkins, J.; Urch, C. J. *J. Chem. Soc. Perkin Trans.* **2001**, *2*, 651–669.

(85)   Atkins, P.; de Paula, J. *Physical Chemistry*, 8th Ed.; WH Freman, 2006.

(86)   Lin, H.-C.; Jin, B.-Y. *Materials (Basel).* **2010**, *3*, 4214–4251.

(87)   Schwartz, M. H. *J. Incl. Phenom. Mol. Recognit. Chem.* **1990**, *9*, 1–35.

(88)   Olsen, G.; Halder, A.; Chi, Q. In *Nanomaterials and Nanotechnology*; Tan, Z., Ed.; One central Press: Manchester.

(89)   Lax, A.; Rchme, F.; Maxwell, R. *Natl. Trust Annu. Archaeol. Rev.* **1998**, 18–23.

(90)   Palermo, V. *Chem. Commun.* **2013**, *49*, 2848–2857.

(91)   Wallace, P. R. *Phys. Rev.* **1947**, *71*, 622–634.

(92)   McClure, J. W. *Phys. Rev.* **1956**, *104*, 666–671.

(93)   Slonczewski, J.; Weiss, P. *Phys. Rev.* **1958**, *109*, 272–279.

(94)   Mermin, N. D. *Phys. Rev.* **1968**, *176*, 250–254.

(95)   Fradkin, E. *Phys. Rev. B* **1986**, *33*, 3263–3268.

(96)   Geim, A. K.; Novoselov, K. S. *Nat. Mater.* **2007**, 183–191.

(97)   Novoselov, K. S.; Geim, A. K.; Morozov, S. V; Jiang, D.; Zhang, Y.; Dubonos, S. V; Grigorieva, I. V; Firsov, A. A. *Science.* **2004**, *306*, 666–669.

(98)   Novoselov, K. S.; Jiang, D.; Schedin, F.; Booth, T. J.; Khotkevich, V. V; Morozov, S. V; Geim, a K. *Proc. Natl. Acad. Sci. USA* **2005**, *102*, 10451–10453.

(99)   Novoselov, K. S.; Geim, A. K.; Morozov, S. V; Jiang, D.; Katsnelson, M. I.; Grigorieva, I. V; Dubonos, S. V; Firsov, A. A. *Nature* **2005**, *438*, 197–200.

(100)   Nobelprize.org. The Nobel Prize in Physics 2010 http://www.nobelprize.org/nobel_prizes/physics/laureates/2010/ (accessed Nov 29, 2015).

(101)   Peigney, A.; Laurent, C.; Flahaut, E.; Bacsa, R. R.; Rousset, A. *Carbon* **2001**, *39*, 507–514.

(102)   Nair, R. R.; Grigorenko, A. N.; Blake, P.; Novoselov, K. S.; Booth, T. J.; Peres, N. M. R.; Stauber, T.; Geim, A. K. *Science* **2008**, *320*, 1308.

(103)   Lee, C.; Wei, X.; Kysar, J. W.; Hone, J. *Science* **2008**, *321*, 385–388.

(104)   Seol, J. H.; Jo, I.; Moore, A. L.; Lindsay, L.; Aitken, Z. H.; Pettes, M. T.; Li, X.; Yao, Z.; Huang, R.; Broido, D.; Mingo, N.; Ruoff, R. S.; Shi, L. *Science* **2010**, *328*, 213–216.

(105)   Balandin, A. A.; Ghosh, S.; Bao, W.; Calizo, I.; Teweldebrhan, D.; Miao, F.; Lau, C. N. *Nano Lett.* **2008**, *8*, 902–907.

(106) Bolotin, K. I.; Sikes, K. J.; Jiang, Z.; Klima, M.; Fudenberg, G.; Hone, J.; Kim, P.; Stormer, H. L. *Solid State Commun.* **2008**, *146*, 351–355.

(107) Zhang, Y.; Tan, Y. W.; Stormer, H. L.; Kim, P. *Nature* **2005**, *438*, 201–204.

(108) Novoselov, K. S.; Jiang, Z.; Zhang, Y.; Morozov, S. V; Stormer, H. L.; Zeitler, U.; Maan, J. C.; Boebinger, G. S.; Kim, P.; Geim, A. K. *Science* **2007**, *315*, 2007.

(109) Robinson, J.; Weng, X.; Trumbull, K.; Cavalero, R.; Wetherington, M.; Frantz, E.; LaBella, M.; Hughes, Z.; Fanton, M.; Snyder, D. *ACS Nano* **2010**, *4*, 153–158.

(110) Bae, S.; Kim, H.; Lee, Y.; Xu, X.; Park, J.-S.; Zheng, Y.; Balakrishnan, J.; Lei, T.; Kim, H. R.; Song, Y. Il; Kim, Y.-J.; Kim, K. S.; Ozyilmaz, B.; Ahn, J.-H.; Hong, B. H.; Iijima, S. *Nat. Nanotechnol.* **2010**, *5*, 574–578.

(111) Muñoz, R.; Gómez-Aleixandre, C. *Chem. Vap. Depos.* **2013**, *19*, 297–322.

(112) Seah, C.-M.; Chai, S.-P.; Mohamed, A. R. *Carbon* **2014**, *70*, 1–21.

(113) Li, X.; Magnuson, C. W.; Venugopal, A.; Tromp, R. M.; Hannon, J. B.; Vogel, E. M.; Colombo, L.; Ruoff, R. S. *J. Am. Chem. Soc.* **2011**, *133*, 2816–2819.

(114) Momiuchi, Y.; Yamada, K.; Kato, H.; Homma, Y.; Hibino, H.; Odahara, G.; Oshima, C. *J. Phys. D. Appl. Phys.* **2014**, *47*, 455301.

(115) Hu, B.; Ago, H.; Orofeo, C. M.; Ogawa, Y.; Tsuji, M. *New J. Chem.* **2012**, *36*, 73.

(116) Seifert, M.; Vargas, J. E. B.; Bobinger, M.; Sachsenhauser, M.; Cummings, A. W.; Roche, S.; Garrido, J. A. *2D Mater.* **2015**, *2*, 024008.

(117) Yazyev, O. V; Louie, S. G. *Nat. Mater.* **2010**, *9*, 806–809.

(118) Yazyev, O. V.; Chen, Y. P. *Nat. Nanotechnol.* **2014**, *9*, 755–767.

(119) Israelachvili, J. N. *Intermolecular and Surface Forces*, 3rd Ed.; Academic Press: Waltham, 2011.

(120) Hernandez, Y.; Nicolosi, V.; Lotya, M.; Blighe, F. M.; Sun, Z.; De, S.; McGovern, I. T.; Holland, B.; Byrne, M.; Gun'Ko, Y. K.; Boland, J. J.; Niraj, P.; Duesberg, G.; Krishnamurthy, S.; Goodhue, R.; Hutchison, J.; Scardaci, V.; Ferrari, A. C.; Coleman, J. N. *Nat. Nanotechnol.* **2008**, *3*, 563–568.

(121) Kahl, H.; Wadewitz, T.; Winkelmann, J. *J. Chem. Eng. Data* **2003**, *48*, 580–586.

(122) Singh, M. *Phys. Chem. Liq.* **2006**, *44*, 579–584.

(123) Coleman, J. N. *Acc. Chem. Res.* **2013**, *46*, 14–22.

(124) Khan, U.; Porwal, H.; Óneill, A.; Nawaz, K.; May, P.; Coleman, J. N. *Langmuir* **2011**, *27*, 9077–9082.

(125) Solomon, H. M.; Burgess, B. A.; Kennedy, G. L.; Staples, R. E. *Drug Chem. Toxicol.* **1995**, *18*, 271–293.

(126) Kennedy, G. L.; Sherman, H. *Drug Chem. Toxicol.* **1986**, *9*, 147–170.

(127) Jasper, J. J. *J. Phys. Chem. Ref. Data* **1972**, *1*, 841.

(128) Ciesielski, A.; Samorì, P. *Chem. Soc. Rev.* **2014**, *43*, 381–398.

(129) Parviz, D.; Das, S.; Ahmed, H. S. T.; Irin, F.; Bhattacharia, S.; Green, M. J. *ACS Nano* **2012**, *6*, 8857–8867.

(130) Khan, U.; O'Neill, A.; Porwal, H.; May, P.; Nawaz, K.; Coleman, J. N. *Carbon* **2012**, *50*, 470–475.

(131) Gong, L.; Kinloch, I. A.; Young, R. J.; Riaz, I.; Jalil, R.; Novoselov, K. S. *Adv.*

Mater. **2010**, *22*, 2694–2697.

(132) Green, A. a.; Hersam, M. C. *Nano Lett.* **2009**, *9*, 4031–4036.

(133) Brodie, B. C. *Philos. Trans. R. Soc. London* **1859**, *149*, 249–259.

(134) Staudenmaier, L. *Berichte der Dtsch. Chem. Gesellschaft* **1898**, *31*, 1481–1487.

(135) Hummers, W. S. J.; Offeman, R. E. *J. Am. Chem. Soc.* **1958**, *80*, 1339–1339.

(136) Zeng , F.; Sun, Z.; Sang, X.; Diamond, D.; Lau, K. T.; Liu, X.; Su, D. S. *ChemSusChem* **2011**, *4*, 1587–1591.

(137) Lerf, A.; He, H.; Riedl, T.; Forster, M.; Klinowski, J. *Solid State Ionics* **1997**, *101-103*, 857–862.

(138) Buchsteiner, A.; Lerf, A.; Pieper, J. *J. Phys. Chem. B* **2006**, *110*, 22328–22338.

(139) Szabó, T.; Tombácz, E.; Illés, E.; Dékány, I. *Carbon* **2006**, *44*, 537–545.

(140) Paredes, J. I.; Villar-Rodil, S.; Martínez-Alonso, A.; Tascón, J. M. D. *Langmuir* **2008**, *24*, 10560–10564.

(141) Dreyer, D. R.; Park, S.; Bielawski, C. W.; Ruoff, R. S. *Chem. Soc. Rev.* **2010**, *39*, 228–240.

(142) Dimiev, A.; Kosynkin, D. V.; Alemany, L. B.; Chaguine, P.; Tour, J. M. *J. Am. Chem. Soc.* **2012**, *134*, 2815–2822.

(143) Hofmann, U.; Holst, R. *Berichte der Dtsch. Chem. Gesellschaft* **1939**, *72*, 754–771.

(144) Scholz, W.; Boehm, H. P. *Z. Anorg. Allg. Chem.* **1969**, *369*, 327–340.

(145) Nakajima, T.; Mabuchi, a.; Hagiwara, R. *Carbon* **1988**, *26*, 357–361.

(146) Lerf, A.; He, H.; Forster, M.; Klinowski, J. *J. Phys. Chem. B* **1998**, *5647*, 4477–4482.

(147) He, H.; Klinowski, J.; Forster, M.; Lerf, A. *Chem. Phys. Lett.* **1998**, *287*, 53–56.

(148) He, H.; Riedl, T.; Lerf, A.; Klinowski, J. *J. Phys. Chem.* **1996**, *100*, 19954–19958.

(149) Jung, I.; Dikin, D. a.; Piner, R. D.; Ruoff, R. S. *Nano Lett.* **2008**, *8*, 4283–4287.

(150) Zhu, Y.; Murali, S.; Cai, W.; Li, X.; Suk, J. W.; Potts, J. R.; Ruoff, R. S. *Adv. Mater.* **2010**, *22*, 3906–3924.

(151) Stankovich, S.; Dikin, D. A.; Piner, R. D.; Kohlhaas, K. A.; Kleinhammes, A.; Jia, Y.; Wu, Y.; Nguyen, S. T.; Ruoff, R. S. *Carbon* **2007**, *45*, 1558–1565.

(152) Shin, H. J.; Kim, K. K.; Benayad, A.; Yoon, S. M.; Park, H. K.; Jung, I. S.; Jin, M. H.; Jeong, H. K.; Kim, J. M.; Choi, J. Y.; Lee, Y. H. *Adv. Funct. Mater.* **2009**, *19*, 1987–1992.

(153) Zhang, J.; Yang, H.; Shen, G.; Cheng, P. *Chem. Commun.* **2010**, *46*, 1112–1114.

(154) Gao, J.; Liu, F.; Liu, Y.; Ma, N.; Wang, Z.; Zhang, X. *Chem. Mater.* **2010**, *22*, 2213–2218.

(155) Mei, X.; Ouyang, J. *Carbon* **2011**, *49*, 5389–5397.

(156) Fan, Z.; Kai, W.; Yan, J.; Wei, T.; Zhi, L.; Feng, J.; Ren, Y.; Song, P.; Wei, F. *ACS Nano* **2011**, *5*, 191–198.

(157) Fan, B. X.; Peng, W.; Li, Y.; Li, X.; Wang, S.; Zhang, G. *Adv. Mater.* **2008**, *20*, 4490–4493.

(158) Mcallister, M. J.; Li, J.; Adamson, D. H.; Schniepp, H. C.; Abdala, A. A.; Liu, J.;

Herrera-alonso, O. M.; Milius, D. L.; Car, R.; Prud, R. K.; Aksay, I. A. *Chem. Mater.* **2007**, *19*, 4396–4404.

(159) Kudin, K. N.; Ozbas, B.; Schniepp, H. C.; Prud'Homme, R. K.; Aksay, I. A; Car, R. *Nano Lett.* **2008**, *8*, 36–41.

(160) Schniepp, H. C.; Li, J. L.; McAllister, M. J.; Sai, H.; Herrera-Alonson, M.; Adamson, D. H.; Prud'homme, R. K.; Car, R.; Seville, D. A.; Aksay, I. A. *J. Phys. Chem. B* **2006**, *110*, 8535–8539.

(161) Long, B.; Manning, M.; Burke, M.; Szafranek, B. N.; Visimberga, G.; Thompson, D.; Greer, J. C.; Povey, I. M.; MacHale, J.; Lejosne, G.; Neumaier, D.; Quinn, A. J. *Adv. Funct. Mater.* **2012**, *22*, 717–725.

(162) Hu, H.; Xin, J. H.; Hu, H.; Wang, X.; Kong, Y. *Appl. Catal. A Gen.* **2015**, *492*, 1–9.

(163) Jia, X.; Campos-Delgado, J.; Terrones, M.; Meunier, V.; Dresselhaus, M. S. *Nanoscale* **2011**, *3*, 86–95.

(164) Lu, Y. H.; Wu, R. Q.; Shen, L.; Yang, M.; Sha, Z. D.; Cai, Y. Q.; He, P. M.; Feng, Y. P. *Appl. Phys. Lett.* **2009**, *94*, 3–5.

(165) Enoki, T.; Takai, K. *Solid State Commun.* **2009**, *149*, 1144–1150.

(166) Quintana, M.; Montellano, A.; Del Rio Castillo, A. E.; Tendeloo, G. Van; Bittencourt, C.; Prato, M. *Chem. Commun.* **2011**, *47*, 9330–9332.

(167) Shi, G.; Wang, X. *Phys. Chem. Chem. Phys.* **2015**, *17*, 28484–28504.

(168) Sun, Z.; Kohama, S. I.; Zhang, Z.; Lomeda, J. R.; Tour, J. M. *Nano Res.* **2010**, *3*, 117–125.

(169) Bekyarova, E.; Itkis, M. E.; Ramesh, P.; Berger, C.; Sprinkle, M.; De Heer, W. A.; Haddon, R. C. *J. Am. Chem. Soc.* **2009**, *131*, 1336–1337.

(170) Bettinger, H. F. *Chemistry* **2006**, *12*, 4372–4379.

(171) Chua, C. K.; Ambrosi, A.; Pumera, M. *Chem. Commun.* **2012**, *48*, 5376–5378.

(172) Liu, L.-H.; Yan, M. *J. Mater. Chem.* **2011**, *21*, 3273.

(173) Strom, T. A.; Dillon, E. P.; Hamilton, C. E.; Barron, A. R. *Chem. Commun.* **2010**, *46*, 4097–4099.

(174) Quintana, M.; Spyrou, K.; Grzelczak, M.; Browne, W. R.; Rudolf, P.; Prato, M. *ACS Nano* **2010**, *4*, 3527–3533.

(175) Zhang, X.; Hou, L.; Cnossen, A.; Coleman, A. C.; Ivashenko, O.; Rudolf, P.; Van Wees, B. J.; Browne, W. R.; Feringa, B. L. *Chem. Eur. J.* **2011**, *17*, 8957–8964.

(176) Ragoussi, M. E.; Malig, J.; Katsukis, G.; Butz, B.; Spiecker, E.; De La Torre, G.; Torres, T.; Guldi, D. M. *Angew. Chem. Int. Ed.* **2012**, *51*, 6421–6425.

(177) Sarkar, S.; Bekyarova, E.; Haddon, R. C. *Acc. Chem. Res.* **2012**, *45*, 673–682.

(178) Sarkar, S.; Bekyarova, E.; Niyogi, S.; Haddon, R. C. *J. Am. Chem. Soc.* **2011**, *133*, 3324–3327.

(179) Niyogi, S.; Bekyarova, E.; Itkis, M. E.; McWilliams, J. L.; Hamon, M. A; Haddon, R. C. *J. Am. Chem. Soc.* **2006**, *128*, 7720–7721.

(180) Su, P.-G.; Lu, Z.-M. *Sens. Actuat. B Chem.* **2015**, *211*, 157–163.

(181) Chen, H. J.; Zhang, Z. H.; Cai, R.; Chen, X.; Liu, Y. N.; Rao, W.; Yao, S. Z. *Talanta* **2013**, *115*, 222–227.

(182)   Dreyer, D. R.; Todd, A. D.; Bielawski, C. W. *Chem. Soc. Rev.* **2014**, *43*, 5288.

(183)   Yang, H.; Shan, C.; Li, F.; Han, D.; Zhang, Q.; Niu, L. *Chem. Commun.* **2009**, No. 26, 3880–3882.

(184)   Shan, C.; Yang, H.; Han, D.; Zhang, Q.; Ivaska, A.; Niu, L. *Langmuir* **2009**, *25*, 12030–12033.

(185)   Stankovich, S.; Piner, R. D.; Nguyen, S. T.; Ruoff, R. S. *Carbon N. Y.* **2006**, *44*, 3342–3347.

(186)   Hsiao, M.-C.; Liao, S.-H.; Yen, M.-Y.; Liu, P.-I.; Pu, N.-W.; Wang, C.-A.; Ma, C.-C. M. *ACS Appl. Mater. Interfaces* **2010**, *2*, 3092–3099.

(187)   Lomeda, J. R.; Doyle, C. D.; Kosynkin, D. V; Hwang, W.-F.; Tour, J. M. *J. Am. Chem. Soc.* **2008**, *130*, 16201–16206.

(188)   Ismaili, H.; Geng, D.; Sun, A. X.; Kantzas, T. T.; Workentin, M. S. *Langmuir* **2011**, *27*, 13261–13268.

(189)   Liu, Y.; Weinert, M.; Li, L. *Nanotechnology* **2015**, *26*, 035702.

(190)   Gómez-Navarro, C.; Meyer, J. C.; Sundaram, R. S.; Chuvilin, A.; Kurasch, S.; Burghard, M.; Kern, K.; Kaiser, U. *Nano Lett.* **2010**, *10*, 1144–1148.

(191)   Bukharaev, A. A.; Berdunov, N. V.; Ovchinnikov, D. V.; Salikhov, K. M. *Scanning Microsc.* **1998**, *12*, 225–234.

(192)   Haubner, K.; Murawski, J.; Olk, P.; Eng, L. M.; Ziegler, C.; Adolphi, B.; Jaehne, E. *ChemPhysChem* **2010**, *11*, 2131–2139.

(193)   Szabó, T.; Berkesi, O.; Forgó, P.; Josepovits, K.; Sanakis, Y.; Petridis, D.; Dékány, I. *Chem. Mater.* **2006**, *18*, 2740–2749.

(194)   Wang, Z.; Dong, Y.; Li, H.; Zhao, Z.; Bin Wu, H.; Hao, C.; Liu, S.; Qiu, J.; Lou, X. W. (David). *Nat. Commun.* **2014**, *5*, 5002.

(195)   Kumar, B.; Asadi, M.; Pisasale, D.; Sinha-Ray, S.; Rosen, B. A.; Haasch, R.; Abiade, J.; Yarin, A. L.; Salehi-Khojin, A. *Nat. Commun.* **2013**, *4*, 1–8.

(196)   Maehashi, K.; Sofue, Y.; Okamoto, S.; Ohno, Y.; Inoue, K.; Matsumoto, K. *Sens. Actuat. B Chem.* **2013**, *187*, 45–49.

(197)   Abraham, A. A.; Rezayi, M.; Manan, N. S. A.; Narimani, L.; Rosli, A. N. Bin; Alias, Y. *Electrochim. Acta* **2015**, *165*, 221–231.

(198)   Li, F.; Ye, J.; Zhou, M.; Gan, S.; Zhang, Q.; Han, D.; Niu, L. *Analyst* **2012**, *137*, 618–623.

(199)   Jaworska, E.; Lewandowski, W.; Mieczkowski, J.; Maksymiuk, K.; Michalska, A. *Analyst* **2013**, *138*, 2363–2371.

(200)   Hernández, R.; Riu, J.; Bobacka, J.; Vallés, C.; Jiménez, P.; Benito, A. M.; Maser, W. K.; Rius, F. X. *J. Phys. Chem. C* **2012**, *116*, 22570–22578.

(201)   Xu, Y.; Zhao, L.; Bai, H.; Hong, W.; Li, C.; Shi, G. *J. Am. Chem. Soc.* **2009**, *131*, 13490–13497.

(202)   Zhu, G.; Wu, L.; Zhang, X.; Liu, W.; Zhang, X.; Chen, J. *Chem. Eur. J.* **2013**, *19*, 6368–6373.

(203)   Yang, L.; Zhao, H.; Li, Y.; Li, C.-P. *Sens. Actuat. B Chem.* **2015**, *207*, 1–8.

(204)   Zor, E.; Bingol, H.; Ramanaviciene, A.; Ramanavicius, A.; Ersoz, M. *Analyst* **2014**,

140, 313–321.

(205) Mao, X.; Zhao, H.; Luo, L.; Tian, D.; Li, H. *J. Mater. Chem. C* **2015**, *3*, 1325–1329.

(206) Swathi, R. S.; Sebastian, K. L. *J. Chem. Phys.* **2008**, *129*, 054703.

(207) Swathi, R. S.; Sebastian, K. L. *J. Chem. Phys.* **2009**, *130*, 086101.

(208) Mao, X.; Tian, D.; Li, H. *Chem. Commun.* **2012**, *48*, 4851–4853.

(209) Olsen, G.; Ulstrup, J.; Chi, Q. *ACS Appl. Mater. Interfaces* **2015**, *8*, 37–41.

(210) Ghafar-Zadeh, E. *Sensors* **2015**, *15*, 3236–3261.

(211) Oesch, U.; Ammann, D.; Simon, W. *Clin. Chem.* **1986**, *32*, 1448–1459.

(212) Bryan, G. W.; Langston, W. J. *Environ. Pollut.* **1992**, *76*, 89–131.

(213) Duruibe, J. O.; Ogwuegbu, M. O. C.; Egwurugwu, J. N. *Int. J. Phys. Sci.* **2007**, *2*, 112–118.

(214) Miyada, D. S.; Inami, K.; Matsuyama, G. *Clin. Chem.* **1971**, *17*, 27–30.

(215) Bühlmann, P.; Pretsch, E.; Bakker, E. *Chem. Rev.* **1998**, *98*, 1593–1688.

(216) Bakker, E. *Anal. Chem.* **2004**, *76*, 3285–3298.

(217) Bakker, E.; Pretsch, E.; Bühlmann, P. *Anal. Chem.* **2000**, *72*, 1127–1133.

(218) Pedersen, C. J. *J. Am. Chem. Soc.* **1967**, *89*, 2495–2496.

(219) Pedersen, C. J. *Angew. Chem. Int. Ed.* **1988**, *27*, 1021–1027.

(220) Christensen, J. J.; Hill, J. O.; Izatt, R. M. *Science* **1971**, *174*, 459–467.

(221) Chen, D.; Feng, H.; Li, J. *Chem. Rev.* **2012**, *112*, 6027–6053.

(222) Wei, W.; Xu, C.; Ren, J.; Xu, B.; Qu, X. *Chem. Commun.* **2012**, *48*, 1284–1286.

(223) Ballesteros-Garrido, R.; de Miguel, M.; Doménech-Carbó, A.; Alvaro, M.; Garcia, H. *Chem. Commun.* **2013**, *49*, 3236–3238.

(224) Banerjee, M.; Gupta, A.; Saha, S. K.; Chakravorty, D. *Small* **2015**, *11*, 3451–3457.

(225) Wang, W.-H.; Gong, C.; Wang, W.; Fullerton-Shirey, S. K.; Seabaugh, A.; Cho, K. *J. Phys. Chem. C* **2015**, *119*, 20016–20022.

(226) Gokel, G. W.; Leevy, W. M.; Weber, M. E. *Chem. Rev.* **2004**, *104*, 2723–2750.

(227) Yechezkel, T.; Salitra, Y.; Gilon, C. *J. Pept. Res.* **1999**, *53*, 507–517.

(228) Blondelle, S. E.; Houghten, R. A. *Int. J. Pept. Protein Res.* **1993**, *41*, 522–527.

(229) Gan, S.; Zhong, L.; Wu, T.; Han, D.; Zhang, J.; Ulstrup, J.; Chi, Q.; Niu, L. *Adv. Mater.* **2012**, *24*, 3958–3964.

(230) Brennessel, W. W.; Ellis, J. E. *Acta Crystallogr. Sect. E Crystallogr. Commun.* **2015**, *71*, 291–295.

(231) Simonov, Y. A.; Fonari, M. S.; Zaworotko, M. J.; Abourahma, H.; Lipkowski, J.; Ganin, E. V; Yavolovskii, A. A. *Org. Biomol. Chem.* **2003**, *1*, 2922–2929.

(232) Moers, O.; Wuaya, K.; Jones, P. G.; Blaschetie, A. *Acta Crystallogr. Sect. C* **1999**, *55*, 1542–1545.

(233) Faridbod, F.; Ganjali, M. R.; Dinarvand, R.; Norouzi, P. *Sensors* **2008**, *8*, 1645–1703.

(234) Meldal, M.; Tornøe, C. W. *Chem. Rev.* **2008**, *108*, 2952–3015.

(235) Himo, F.; Lovell, T.; Hilgraf, R.; Rostovtsev, V. V; Noodleman, L.; Sharpless, K.

B.; Fokin, V. V. *J. Am. Chem. Soc.* **2005**, *127*, 210–216.

(236) Huisgen, R. *Angew. Chemie Int. Ed.* **1963**, *2*, 565–598.

(237) Rostovtsev, V. V.; Green, L. G.; Fokin, V. V.; Sharpless, K. B. *Angew. Chem. Int. Ed.* **2002**, *41*, 2596–2599.

(238) Tornøe, C. W.; Christensen, C.; Meldal, M. *J. Org. Chem.* **2002**, *67*, 3057–3064.

(239) Kolb, H. C.; Finn, M. G.; Sharpless, K. B. *Angew. Chem. Int. Ed.* **2001**, *40*, 2004–2021.

(240) Rodionov, V. O.; Fokin, V. V.; Finn, M. G. *Angew. Chem. Int. Ed.* **2005**, *44*, 2210–2215.

(241) Kou, L.; He, H.; Gao, C. *Nano-Micro Lett.* **2010**, *2*, 177–183.

(242) Wang, Z.; Ge, Z.; Zheng, X.; Chen, N.; Peng, C.; Fan, C.; Huang, Q. *Nanoscale* **2012**, *4*, 394–399.

(243) Pan, Y.; Bao, H.; Sahoo, N. G.; Wu, T.; Li, L. *Adv. Funct. Mater.* **2011**, *21*, 2754–2763.

(244) Cao, Y.; Lai, Z.; Feng, J.; Wu, P. *J. Mater. Chem.* **2011**, *21*, 9271.

(245) Sun, S.; Cao, Y.; Feng, J.; Wu, P. *J. Mater. Chem.* **2010**, *20*, 5605.

(246) Sun, Y.; Mao, X.; Luo, L.; Tian, D.; Li, H. *Org. Biomol. Chem.* **2015**, *13*, 9294–9299.

(247) Shen, X.; Liu, Y.; Pang, Y.; Yao, W. *Electrochem. commun.* **2013**, *30*, 13–16.

(248) Kaminska, I.; Das, M. R.; Coffinier, Y.; Niedziolka-Jonsson, J.; Sobczak, J.; Woisel, P.; Lyskawa, J.; Opallo, M.; Boukherroub, R.; Szunerits, S. *ACS Appl. Mater. Interfaces* **2012**, *4*, 1016–1020.

(249) Jin, Z.; McNicholas, T. P.; Shih, C. J.; Wang, Q. H.; Paulus, G. L. C.; Hilmer, A. J.; Shimizu, S.; Strano, M. S. *Chem. Mater.* **2011**, *23*, 3362–3370.

(250) Soai, K.; Shuji, Y.; Atsuhiro, O. *Synthesis (Stuttg).* **1987**, *1987*, 48–49.

(251) Tran, A. T.; Huynh, V. A.; Friz, E. M.; Whitney, S. K.; Cordes, D. B. *Tetrahedron Lett.* **2009**, *50*, 1817–1819.

(252) Thompson, A. S.; Humphrey, G. R.; DeMarco, A. M.; Mathre, D. J.; Grabowski, E. J. J. *J. Org. Chem.* **1993**, *58*, 5886–5888.

(253) Ju, Y.; Kumar, D.; Varma, R. S. *J. Org. Chem.* **2006**, *71*, 6697–6700.

(254) Quesada, E.; Taylor, R. J. K. *Tetrahedron Lett.* **2005**, *46*, 6473–6476.

(255) Gribble, W. G. *Chem. Soc. Rev.* **1998**, *27*, 395.

(256) Kumar, R.; Gopalakrishnan, K.; Ahmad, I.; Rao, C. N. R. *Adv. Funct. Mater.* **2015**, *25*, 5910–5917.

(257) Besset, C.; Chambert, S.; Fenet, B.; Queneau, Y. *Tetrahedron Lett.* **2009**, *50*, 7043–7047.

(258) Corey, E. J.; Kang, M.; Desai, M. C.; Ghosh, A. K.; Houpis, I. N. *J. Am. Chem. Soc.* **1988**, *10*, 649–651.

(259) Knölker, H. J.; Braxmeier, T. *Tetrahedron Lett.* **1996**, *37*, 5861–5864.

(260) Corey, E. J.; Venkateswrlu, A. *J. Am. Chem. Soc.* **1972**, *94*, 6190–6191.

(261) Moulder, J. F.; Stickle, W. F.; Sobol, P. E.; Bomben, K. D. *Handbook of X-ray*

Photoelectron Spectroscopy; Physical Electronics Inc: Eden Prairie, Minnesota 55344, 1992.

(262)   Yamashita, T.; Hayes, P. *Appl. Surf. Sci.* **2008**, *254*, 2441–2449.

(263)   Kutonova, K. V.; Trusova, M. E.; Postnikov, P.; Filimonov, V. D.; Parello, J. *Synth.* **2013**, *45*, 2706–2710.

(264)   Ambrosi, A.; Chua, C. K.; Bonanni, A.; Pumera, M. *Chem. Mater.* **2012**, *24*, 2292–2298.

(265)   Hurtley, W. R. H.; Smiles, S. *J. Chem. Soc.* **1926**, *129*, 2263–2270.

(266)   Wudl, F.; Smith, G. M.; Hufnagel, E. J. *J. Chem. Soc. D* **1970**, 1453–1454.

(267)   Wudl, F.; Wobschall, D.; Hufnagel, E. J. *J. Am. Chem. Soc.* **1972**, *94*, 670–672.

(268)   Bryce, B. M. R. *Adv. Funct. Mater.* **1999**, *11*, 11–23.

(269)   Jeppesen, J. O.; Nielsen, M. B.; Becher, J. *Chem. Rev.* **2004**, *104*, 5115–5132.

(270)   Jorgensen, T.; Hansen, T. K.; Becher, J. *Chem. Soc. Rev.* **1994**, *23*, 41–51.

(271)   Bryce, M. R. *Chem. Soc. Rev.* **1991**, *20*, 355.

(272)   Talham, D. R. *Chem. Rev.* **2004**, *104*, 5479–5501.

(273)   Bendikov, M.; Wudl, F.; Perepichka, D. F. *Chem. Rev.* **2004**, *104*, 4891–4945.

(274)   Ferraris, J.; Cowan, D. O.; Walatka, V.; Perlstein, J. H. *J. Am. Chem. Soc.* **1973**, *95*, 948–949.

(275)   Baeyer, A. *Berichte der Dtsch. Chem. Gesellschaft* **1886**, *19* (2), 2184–2185.

(276)   Jacoby, D.; Floriani, C.; Chiesi-Villa, A.; Rizzoli, C. *J. Chem. Soc. Chem. Commun.* **1991**, *077*, 220.

(277)   Brown, W. H.; Hutchinson, B. J.; MacKinnon, M. H. *Can. J. Chem.* **1971**, *49*, 4017–4022.

(278)   Rothemund, P.; Gage, C. L. *J. Am. Chem. Soc.* **1955**, *77*, 3340–3342.

(279)   Gale, P. A.; Sessler, J. L.; Král, V. *Chem. Comm.* **1998**, 1–8.

(280)   Caltagirone, C.; Gale, P. A. *Chem. Soc. Rev.* **2009**, *38*, 520–563.

(281)   Gale, P. a.; Anzenbacher, P.; Sessler, J. L. *Coord. Chem. Rev.* **2001**, *222*, 57–102.

(282)   Gale, P. A.; Sessler, J. L.; Král, V.; Lynch, V. *J. Am. Chem. Soc.* **1996**, *118*, 5140–5141.

(283)   Pichierri, F. *J. Mol. Struct.* **2008**, *870*, 36–42.

(284)   Wang, D.; Wu, Y.-D. *J. Theor. Comput. Chem.* **2004**, *3*, 51–68.

(285)   Pichierri, F. *J. Mol. Struct.* **2002**, *581*, 117–127.

(286)   Wu, Y. D.; Wang, D. F.; Sessler, J. L. *J. Org. Chem.* **2001**, *66*, 3739–3746.

(287)   Blas, J. R.; Mrquez, M.; Sessler, J. L.; Luque, F. J.; Orozco, M. *J. Am. Chem. Soc.* **2002**, *124*, 12796–12805.

(288)   Anzenbacher, P.; Try, A. C.; Miyaji, H.; Jursikova, K.; Lynch, V. M.; Marquez, M.; Sessler, J. L. *J. Am. Chem. Soc.* **2000**, *122*, 10268–10272.

(289)   Nielsen, K. a; Cho, W.-S.; Jeppesen, J. O.; Lynch, V. M.; Becher, J.; Sessler, J. L. *J. Am. Chem. Soc.* **2004**, *126*, 16296–16297.

(290)   Nielsen, K. a; Cho, W.-S.; Lyskawa, J.; Levillain, E.; Lynch, V. M.; Sessler, J. L.; Jeppesen, J. O. *J. Am. Chem. Soc.* **2006**, *128*, 2444–2451.

(291)   Nielsen, K. A.; Jeppesen, J. O.; Levillain, E.; Becher, J. *Angew. Chem.* **2003**, *115*, 197–201.

(292)   Fulmer, G. R.; Miller, A. J. M.; Sherden, N. H.; Gottlieb, H. E.; Nudelman, A.; Stoltz, B. M.; Bercaw, J. E.; Goldberg, K. I.; Gan, R.; Apiezon, H. *Organometallics* **2010**, *29*, 2176–2179.

(293)   Compton, O. C.; Jain, B.; Dikin, D. a; Abouimrane, A.; Amine, K.; Nguyen, S. T. *ACS Nano* **2011**, *5*, 4380–4391.

Appendix A Publications and Dissemination

Publications

1. <u>Gunnar Olsen</u>, Jens Ulstrup, Qijin Chi, "Crown-Ether Derived Graphene Hybrid Composite for Membrane-Free Potentiometric Sensing of Alkali Metal Ions", *ACS Applied Materials Interfaces*, **2016**, *8* (1), pp 37–41

2. <u>Gunnar Olsen</u>, Arnab Halder, Qijin Chi "Supramolecular Graphene Nanocomposites and Applications for Chemosensors and Biosensors" Chapter in the Book entitled "Nanomaterials and Nanotechnology" 2016 One Central Press: One Central Park, Northampton Road, Manchester, M40 5BP, UK (provisionally accepted - Book Chapter)

Publication Outside PhD work

1. Steffen Bähring, <u>Gunnar Olsen</u>, Paul C. Stein, Jacob Kongsted, Kent A. Nielsen, "Coordination-Driven Switching of a Preorganized and Cooperative Calix[4]pyrrole Receptor" *Chem. Eur. J.*, **2013**, *19*, 2768 – 2775

2. Steffen Bähring, Luis Martín-Gomis, <u>Gunnar Olsen</u>, Kent A. Nielsen, Dong Sub Kim, Troels Duedal, Ángela Sastre-Santos, Jan O. Jeppesen, Jonathan L. Sessler "Design and Sensing Properties of a Self-Assembled Supramolecular Oligomer" *Chem. Eur. J.* **2016**, *22*, 1958-1967 (cover article)

3. Steffen Bähring, Luis Martín-Gomis, <u>Gunnar Olsen</u>, Kent A. Nielsen, Dong Sub Kim, Troels Duedal, Ángela Sastre-Santos, Jan O. Jeppesen, Jonathan L. Sessler "Cover Picture: Design and Sensing Properties of a Self-Assembled Supramolecular Oligomer" *Chem. Eur. J.* **2016**, 22, pp 1865 (cover picture)

Oral Presentations

1. "Alkali Metal Sensing: CMRGO Source-Drain Devise" 2nd ELECTRONANOMAT workshop **Oct 2014**, Shanghai, China

2. "Azido-RGO as a Universal Platform for RGO based Sensors" DTU – Chemistry PhD symposium **Nov 2015**, Kgs. Lyngby, Denmark (Best Oral Presentation Award)

Poster Presentations

1. "Supramolecular Functionalization of RGO Nanosheets for Chemical Sensing" XVI. Annual Linz Winter Workshop **Feb 2014**, Linz, Austria

2. "18-Crown[6]ether Functionalized Reduced Graphene Oxide for Membrane-free Ion Selective Sensing" Carbonhagen - 6th symposium on carbon and related nanomaterials, **Aug 2015**, Copenhagen, Denmark

Manuscripts under preparation

1. Gunnar Olsen, Jens Ulstrup, Qijin Chi, "A series of Crown-Ether functionalized Graphene Materials for Alkali Metal Ions Sensing"

2. Gunnar Olsen, Jens Ulstrup, Qijin Chi, "Azido-RGO – A General Platform for Post-Reduction Functionalization of Graphene"

3. Arnab Halder, Minwei Zhang, Gunnar Olsen and Qijin Chi "Biocompatible electroactive engineering graphene with dopamine for highly sensitive detection of melamine"